THE UNIVERSITY OF MANITOBA

Heat Affected Zone Cracking of Allvac 718Plus Superalloy during High Power Beam Welding and Post-weld Heat Treatment.

OLUWASEUN AYODEJI IDOWU

A dissertation submitted to the Faculty of Graduate Studies in partial fulfillment of the requirement for the degree of

Doctor of Philosophy

Department of Mechanical and Manufacturing Engineering

Winnipeg, Manitoba

Acknowledgements

I am sincerely grateful to my supervisor, Dr M.C. Chaturvedi, for granting me the opportunity to work on this interesting project. The journey is long, but it would not have been possible for me to reach this milestone without his patience, understanding, and valuable advice. Also, I am very grateful to my co-supervisor, Dr O.A. Ojo for his timely suggestions and encouragements. His one-on-one sit-down discussion sessions were very helpful in charting the right course for my research. I acknowledge Dr N.L. Richards and Dr M.S. Freund, who are members of my examining committee, for their several constructive inputs at various stages of my research.

I thank ATI Allvac for providing Allvac 718Plus superalloy which was used for this research. I acknowledge the financial support provided for this research project by Standard Aero Ltd, Bristol Aerospace, Boeing Canada Technologies Ltd, Manitoba Aerospace Association, NSERC etc. I also appreciate graduate fellowship awards provided for my study by the University of Manitoba and NSERC. I am grateful to Dr Zhang, Dr Rong Liu, John Van Dorp, Dan McCooeye, Don Mardis and Mike Boskwick for their technical assistance. Thanks are also due to Dr. Krutika, Dr. Dotun, Dr. Sidhu and other members of the materials research group for their support and friendliness. I sincerely appreciate the love and support that I received from Mr and Mrs Adegunju in Winnipeg. They opened up their home to me, and made me feel free to call it my home.

I am very thankful to God, the source of my wisdom and understanding. Finally, I would like to thank my beautiful wife, Boluwatife, and daughter, Oludunni, for their love, support and encouragement. Boluwatife did not allow me to rest each day after coming home from work until I got this thesis done.

Abstract

The present dissertation reports the findings of a study of cracking behavior of a newly developed superalloy, Allvac 718Plus during high power beam welding and post-weld heat treatments. Microstructures of the base alloy, heat affected zone (HAZ) and fusion zone of welded and post-weld heat treated coupons were examined by the use of standard metallographic techniques involving optical microscopy, analytical scanning electron microscopy (SEM) and analytical transmission electron microscopy. Moreover, non-equilibrium segregation behavior of boron atoms to the grain boundaries of the alloy during pre-weld heat treatments was evaluated using secondary ion mass spectroscopic system.

In the first phase of the research, 718Plus was welded using a low and high heat input CO_2 laser to assess the response of the alloy to welding. Detailed examination of the welds by analytical electron microscopic technique revealed the occurrence of cracking in the heat affected zone (HAZ) of low heat input welds, while their fusion zone (FZ) was crack free. However, both the FZ and HAZ of high heat input welds were crack-free. Resolidified constituents were observed along the cracked grain boundaries of the lower heat input welds, which indicated that HAZ cracking in this newly developed superalloy was associated with grain boundary liquation. However, despite a more extensive liquation of grain boundaries and grain interior in the HAZ of high heat input welds, no cracking occurred. This was attributed to the combination of lower welding

stresses generated during cooling, and relaxation of these stresses by thick intergranular liquid.

Although HAZ cracking was prevented by welding with a high heat input laser, it resulted in a significant damage to the parent microstructure through its extensive liquation. Therefore, such a technique is not usually recommended in order to ensure integrity of weld structures. The use of low heat input welding, which will minimize the microstructural damage is desirable. Thus, it is necessary that another approach be employed to minimize or eliminate HAZ cracking of the alloy which occurred during welding using low heat input. The use of suitable pre-weld heat treatment to engineer pre-weld microstructure capable of reducing or eliminating cracking during welding has been widely reported for other nickel-base superalloys. Therefore, during the second phase of this research, the effects of pre-weld thermal processing on the cracking response of 718Plus were investigated. The alloy was thermally treated at different temperatures and cooling rates before welding. Results from the quantification of the cracking response of the alloy showed that HAZ cracking during welding may be significantly reduced or eliminated through an adequate selection of pre-weld thermal cycle.

In the third stage of this research, crack-free welds of 718Plus were post-weld heat treated using standard thermal schedules recommended by the manufacturer of 718Plus. This was meant to relieve welding stresses as well as homogenize the microstructure of the welds. However, a significant solid state cracking of the alloy

occurred during the post-weld heat treatment. This appears to constitute a major difference between the weldability of γ' strengthened 718Plus and that of its parent alloy, 718, which is strengthened by γ'' precipitate that has a sluggish precipitation kinetics. It is hypothesized that post-weld heat treatment cracking of 718Plus occurred due to the combined presence of aging contraction stresses, due to fast precipitation of γ' in HAZ, at a period when the grain boundaries in the zone have been embrittled. SEM and TEM analyses revealed a significant precipitation of γ′ phase during post-weld heat treatment of the welds. Also, the grain boundaries that mostly cracked during post-weld heat treatment were outlined by Laves phase and extensive needle-like precipitates of δ phase. The Laves phase formed as a resolidification product on liquated grain boundaries in weld HAZ during welding, while the needle-like δ phase precipitated around the Laves phase during PWHT. It has been reported in previous studies on 718-type alloy that Laves phase is very brittle and has a weak interface with the γ matrix; therefore, it may provide preferential sites for crack initiation and propagation. The extensive formation of δ needles, as observed in the present work, has been also reported to impair the strength of 718-type alloys. Thus, during post-weld heat treatment of 718Plus, the presence of the embrittling phases on HAZ grain boundaries, coupled with aging contraction stresses that are generated during aging, would result in cracking of the grain boundaries at a period when the matrix has been hardened by a considerable precipitation of γ′ phase.

TABLE OF CONTENTS

Acknowledgements ii

Abstract iii

Table of Contents vi

List of Figures x

List of Tables xvii

Chapter 1: Introduction 1

Chapter 2: Literature Review 3

2.1 Physical Metallurgy of Inconel 718 Alloy 3

2.1.1 Introduction 3

2.1.2 Microstructure of Inconel 718 5

2.2 Physical Metallurgy of 718Plus Superalloy 12

2.2.1 Introduction 12

2.2.2 Microstructure of 718Plus 16

2.3 Welding, Residual Stresses and Weld Imperfections 18

2.3.1 General Introduction 18

2.3.2 Fusion Welding Processes 21

2.3.2.1 High Energy Beam Welding Processes 26

2.3.2.1.1 Electron Beam Welding Process 26

2.3.2.1.2 Laser Beam Welding Process 29

2.3.3 Residual Stresses in Welds 32

2.3.4 Weld Imperfections 35

2.3.4.1 Introduction 35

2.3.4.2 Weld Imperfections – Welding Process Related 35

2.3.4.3 Weld Imperfections – Design Related 39

2.3.4.4 Weld Imperfections – Metallurgical 39

2.3.4.4.1 Solidification Cracking in Welds 40

2.3.4.4.1.1 Theories of Solidification Cracking 44

2.3.4.4.1.1.1 Shrinkage Brittleness Theory 44

2.3.4.4.1.1.2 Strain Theory of Hot Cracking 47

2.3.4.4.1.1.3 Generalized Theory of Super-Solidus Cracking 53

2.3.4.4.2 Weld Heat Affected Zone Liquation Cracking 59

2.3.4.4.2.1 Theories of Weld Heat Affected Zone Liquation Cracking 61

2.3.4.4.2.1.1 Constitutional Liquation Theory 61

2.3.4.4.2.1.2 Grain Boundary Segregation Mechanism 69

2.3.4.4.3 Post-Weld Heat Treatment Cracking in Superalloys 72

2.3.4.4.3.1 Development of Post-Weld Heat Treatment Cracking in Superalloys 73

2.3.4.4.3.2 Factors Affecting Post-Weld Heat Treatment Cracking in Superalloys 75

2.4 Previous Investigations on the Weldability of 718-Type Alloy 79

2.5 Scope and Nature of the Present Study 82

Chapter 3: Experimental Procedures **87**

3.1 Materials and Processing 87

3.1.1 Materials and Pre-weld Heat Treatments 87

3.1.2 Welding 87

3.1.3 Post-Weld Heat Treatments 90

3.2 Optical and Scanning Electron Microscopy 90

3.3 Secondary Ion Mass Spectroscopy 91

3.4 Transmission Electron Microscopy 92

Chapter 4: Results and Discussion **95**

4.1 Effect of Weld Heat Input on the Microstructure and Heat Affected Zone Cracking of 718Plus **95**

4.1.1 Introduction 95

4.1.2 Microstructure of Pre-weld Solution Heat Treated Alloy 95

4.1.3 Fusion Zone and HAZ Microstructures of Low and High Heat Input Welds of 718Plus 101

4.1.5 The Occurrence of Liquid Backfilling in the HAZ of Low Heat Input Welds of 718Plus 112

4.2 Influence of Pre-weld Heat Treatments on Weld Heat Affected Zone Cracking of 718Plus **120**

4.2.1 Introduction 120

4.2.2 Microstructure of Pre-weld Solution Heat Treated 718Plus 121

4.2.3 HAZ Microstructure of Welded Alloy 124

4.2.4 Effect of Pre-weld Heat Treatments on Grain Boundary Segregation of Boron and HAZ Cracking 132

4.2.5 Effect of Pre-Weld Heat Treatments on Grain Size and Weld HAZ Cracking 142

4.3 **Post-weld Heat Treatment Microstructure and Cracking in HAZ of 718Plus** **145**

4.3.1 Introduction 145

4.3.2 Microstructure of Weld Fusion Zone after Standard Post-weld Heat Treatment 146

4.3.3 Weld HAZ Microstructure and Cracking during Standard Post-weld Heat Treatment of 718Plus 161

4.3.4 Development of Post-weld Heat Treatment Cracking in 718Plus 175

Chapter 5: Summary and Conclusions **181**

5.1 Effect of Weld Heat Input on Heat Affected Zone Cracking of 718Plus 181

5.2 Influence of Pre-weld Heat Treatments on Weld Heat Affected Zone Cracking of 718Plus 182

5.3 Post-weld Heat Treatment Microstructure and Cracking of 718Plus 184

Chapter 6: Suggestions for Future Work **186**

References **189**

Refereed Publications from the Present Work **199**

Other Refereed Publications **199**

Poster Presentations **200**

List of Figures

Figure		Page
2-1	Unit cell illustrating DO_{22} ordered structure of BCT lattice of γ'' phase [10]	7
2-2	Unit cell illustrating $L1_2$ ordered FCC lattice of γ' phase [10]	9
2-3	Oxyacetylene welding: a) overall process, b) welding area enlarged [30]	23
2-4	Gas Tungsten Arc Welding: a) overall process, b) welding area enlarged [30]	25
2-5	Electron Beam Welding: a) process; b) keyhole [30]	27
2-6	Laser beam welding with solid state laser: a) process, b) energy absorption and emission during laser action [30]	30
2-7	Schematic illustration of changes in temperature and stresses during welding [32]	33
2-8	Schematic illustration of changes in stress-temperature and stress-strain during welding thermal cycle. Point 6 refers to the final residual stress and strain after the element has cooled to ambient temperature [33]	34
2-9	Weld Imperfections	36
2-10	Effect of the amount of liquid on crack susceptibility: a) weld, b) crack susceptibility curve, c) pure metal, d) small liquid amount e) more liquid, and f) much more liquid [30]	42
2-11	Hot cracking susceptibility of eutectiferous alloys [45]	46
2-12	Schematic illustration of hot cracking in castings by fracture through interdendritic liquid films existing near solidus temperature [51]	49
2-13	Schematic illustration of weld hot cracking processes a) liquation of segregate, b) hot cracking of base metal c) hot cracking of weld [51]	50
2-14	Schematic illustration of strain distribution during various stages of solidification in a casting system containing hot spot [51]	52

List of Figures Contd.

Figure		Page
2-15	Schematic illustration of strain theory of hot cracking [51]	54
2-16	Effect of constitutional features on cracking susceptibility in binary systems (Generalized theory) [45]	56
2-17	Effect of dihedral angle (θ) on the shape and distribution of liquid phase on grain corners, edges and faces [45]	58
2-18	Schematic diagram of a portion of hypothetical phase diagram for an alloy system exhibiting constitutional liquation [56]	63
2-19	Schematic representation of the concentration gradients at various temperatures during constitutional liquation [56]	65
2-20	Schematic representation of the effect of holding time on stability of liquid film produced by constitutional liquation [56]	68
2-21	Post weld heat treatment cracking: a) phase diagram, b) thermal cycles during welding and heat treating, c) precipitation C curve, d) weld cross-section, e) changes in microstructure [30]	74
2-22	Separation between γ′ strengthened alloys that are difficult to weld and those readily weldable [89]	76
2-23	Flow chart of research approach on: a) HAZ cracking during low and high heat input laser welding, b) influence of pre-weld heat treatments on weld HAZ cracking, c) PWHT microstructure and cracking in 718Plus	84
4-1	(a) Optical and (b) SEM microstructure of solution heat treated ($1025^{o}C$/1 hr + water cool) 718Plus superalloy showing intergranular and intragranular particles within γ matrix	96
4-2	SEM/EDS spectrum from (a) Nb, Ti-rich carboboride, (b) Ti, Nb-rich carbonitride in 718Plus solution heat treated at $1025^{o}C$/1h + water cool	97
4-3	Optical micrographs of the fusion and heat affected zones of (a) low heat and (b) high heat input welds of 718Plus	102

List of Figures Contd.

Figure		Page
4-4	SEM microstructure of the fusion zone of a laser weld of 718Plus. Top right inset shows Nb, Ti-rich carboboride while top left inset shows a Ti, Nb-rich carbonitride in the fusion zone	103
4-5	SEM micrograph showing HAZ cracking in low heat input laser weld of 718Plus. Base inset shows interfacial liquation of Nb, Ti-rich carboboride in the HAZ	104
4-6	SEM backscattered electron images of HAZ cracks associated with (a) Nb,Ti-rich carboboride and (b) Ti, Nb-rich carbonitride. Inset in (b) shows resolidification product outlining a crack	105
4-7	SEM micrograph showing a crack-free HAZ of a high heat input laser weld of 718Plus. Note extensive liquation within HAZ grain interior and of grain boundaries	107
4-8	SEM micrograph showing a crack-free HAZ of a TIG weld of 718Plus. Note extensive liquation within HAZ grain interior and of grain boundaries	111
4-9	SEM micrograph of incompletely backfilled crack in weld HAZ of low heat input laser weld of 718Plus. Resolidification products on the boundary are shown at higher magnification (x4300)	113
4-10	SEM a) micrograph showing the thickened appearance and reverse curvature of HAZ grain boundary (GY) due to LFM, b) X-ray line scan showing Nb-enrichment of a migrated region around GY compared to adjacent γ matrix	114
4-11	SEM microstructure of 718Plus solution heat treated at 950^{o}C and a) iced water quenched, b) air cooled, c) furnace cooled. The top right inset on 1c shows γ′ particles in γ matrix of the furnace cooled samples	122
4-12	SEM microstructure of 718Plus solution heat treated at 1050^{o}C and a) iced water quenched, b) air cooled, c) furnace cooled. The top right inset on 1c shows γ′ particles in γ matrix of furnace cooled samples	123

List of Figures Contd.

Figure		Page
4-13	Optical micrographs (x100, 10% oxalic etch) of 718Plus showing the variation in grain size after solution heat treatment at a) 950°C, b) 1050°C, c) 1150°C and followed by air cooling	125
4-14	Variation in average grain size of 718Plus with pre-weld heat treatment temperature and cooling rate	126
4-15	SEM micrograph showing the absence of HAZ cracking in the weld of 718Plus that was pre-weld solution heat treated at 950°C and iced water quenched	127
4-16	SEM micrographs showing γ′ particles a) before welding (i.e. after 950°C + furnace cool), and b) after welding (in the HAZ)	129
4-17	(a) Optical, and (b) SEM micrographs showing cracking in the weld HAZ of 718Plus that was pre-weld solution heat treated at 1150°C + air cool	130
4-18	Variation in HAZ total crack length (TCL) of 718Plus with pre-weld heat treatment temperature and cooling rate	131
4-19	SIMS image of boron in 718Plus after heat treatment at 950°C and a) iced-water quench b) air cool c) furnace cool	135
4-20	SIMS image of boron in 718Plus after heat treatment at 1050°C and a) iced-water quench b) air cool c) furnace cool	135
4-21	SIMS image of boron in 718Plus after heat treatment at 1150°C and a) iced-water quench b) air cool c) furnace cool	135
4-22	SIMS micrographs showing grain boundary boron segregation in 718Plus (higher boron version ≈ 60 ppm) after pre-weld heat treatment at a) 950°C, b) 1050°C, and c) 1150°C. All samples were air cooled	140
4-23	Variation in weld HAZ total crack length (TCL) of 718Plus (higher boron version ≈ 60 ppm) with pre-weld heat treatment temperature. All samples were air cooled	141

List of Figures Contd.

Figure		Page
4-24	Optical micrograph showing cellular-dendritic microstructure of weld fusion zone of 718Plus following pre-weld solution heat treatment (SHT) at 950^{o}C/1hr +AC, and post-weld heat treatments comprising of a) SHT at 950^{o}C/1hr +AC, and b) aging heat treatment at 788^{o}C/ 8 hrs + furnace cool to 654^{o}C/ 8 hrs + air cool	147
4-25	(a): SEM secondary electron image of weld fusion zone microstructure of 718Plus following pre-weld solution heat treatment (SHT) at 950^{o}C/1hr +AC, and post-weld heat treatments comprising of a) SHT at 950^{o}C/1hr +AC, and b) aging heat treatment at 788^{o}C/ 8 hrs + furnace cool to 654^{o}C/ 8 hrs + AC	148
	(b): SEM backscattered electron image of weld fusion zone microstructure of 718Plus following pre-weld solution heat treatment (SHT) at 950^{o}C/1hr +AC, and post-weld heat treatments comprising of a) SHT at 950^{o}C/1hr +AC, and b) aging heat treatment at 788^{o}C/ 8 hrs + furnace cool to 654^{o}C/ 8 hrs + AC	149
4-26	TEM bright field image of fusion zone constituents of post-weld heat treated 718Plus, showing carbide (C), matrix (M), Laves (L) and delta (D) phases	151
4-27	TEM/ EDS spectrum of a) MC-type carbide, b) Laves constituents in the fusion zone of post-weld heat treated 718Plus (c) delta phase, (d) matrix in the fusion zone of post-weld heat treated 718Plus	152
4-28	TEM SADPs from a) $[\bar{1}12]$, and b) $[\bar{1}14]$ zone axes of a MC-type carbide particle (C) in the fusion zone of post-weld heat treated 718Plus	155
4-29	TEM SADP from $[01\bar{1}2]$ zone axis of a Laves particle (L) in the fusion zone of post-weld heat treated 718Plus	155
4-30	TEM SADP from [100] zone axis of delta phase particle (D) in the fusion zone of post-weld heat treated 718Plus	157

List of Figures Contd.

Figure		Page
4-31	TEM a) SADP from [001] zone axis of γ matrix (M) showing the presence of superlattice reflections typical to $L1_2$ ordered lattice of γ′ phase, b) dark field image of γ′ particles taken with (010) superlattice reflection in the fusion zone of post-weld heat treated 718Plus	158
4-32	TEM SADP from [011] zone axis of γ matrix showing the absence of superlattice reflections of γ′ phase in the as-weld fusion zone of 718Plus	158
4-33	SEM secondary electron image of the as-weld fusion zone of an electron beam welded 718Plus	159
4-34	Optical micrograph of as-weld HAZ of 718Plus which was pre-weld solution heat treated at 950^{o}C/1hr +AC, showing absence of HAZ cracks	162
4-35	Optical micrograph of as-weld HAZ of 718Plus which was pre-weld solution heat treated at 1050^{o}C/1hr +AC, showing presence of HAZ crack	162
4-36	SEM backscattered electron image of as-weld HAZ of 718Plus, which was pre-weld solution heat treated at 950^{o}C/1hr +AC, showing absence of HAZ cracks	163
4-37	SEM backscattered electron image of as-weld HAZ of 718Plus, which was pre-weld solution heat treated at 1050^{o}C/1hr +AC, showing presence of HAZ cracks (marked with arrow heads)	163
4-38	SEM backscattered electron image of as-weld HAZ of 718Plus, which was pre-weld solution heat treated at 1050^{o}C/1hr +AC, showing grain boundary outlined by γ/Laves eutectic-like phase (marked with arrow heads)	165
4-39	TEM SADP from a) [011] zone axis of γ matrix from HAZ, b) [001] zone axis of γ matrix from base metal region, showing the absence of superlattice reflections of γ′ phase in as-weld 718Plus which was pre-weld heat treated at 950^{o}C/1hr +AC	167

List of Figures Contd.

Figure		Page
4-40	Figs. 4-40 a & b: SEM backscattered electron images showing presence of HAZ cracks in 718Plus after post-weld heat treatment. Coupon was pre-weld solution heat treated at 950^{o}C/1hr +AC	168
4-41	Higher magnification SEM backscattered electron image of a post-weld heat treatement crack in HAZ of 718Plus. Note dense network of Laves phase and acicular δ precipitate outlining the crack	169
4-42	SEM backscattered electron image showing presence of HAZ cracks in 718Plus after post-weld heat treatment. Coupon was pre-weld solution heat treated at 1050^{o}C/1hr +AC	171
4-43	SEM backscattered electron image showing presence of HAZ cracks in 718Plus after post-weld heat treatment. Coupon was pre-weld solution heat treated at 1050^{o}C/1hr +AC	172
4-44	SEM micrograph showing microstructure of HAZ grain interior of 718Plus after post-weld heat treatment	173
4-45	TEM dark field image of γ′ particles in the HAZ of post-weld heat treated 718Plus. Arrows show occasionally large γ′ particles in finer γ′ particles	174

List of Tables

Table		Page
2-1	Elemental Composition Range of Alloy 718 (wt %) [7]	4
2-2	Comparison of Nominal Composition of 718Plus and 718 [2]	14
2-3	Mechanical Properties and Thermal Stability of 718Plus in Comparison with Alloy 718 and Waspaloy [2]	15
2-4	Crystal structure and chemical composition of γ′ phase in Allvac 718Plus [25]	17
2-5	Metallic compositions (SEM-EDS) of δ phase, MC-type carbides, and Laves phase in alloys 718 and 718Plus [25]	19
2-6	Phase transformation temperatures in Allvac 718Plus [25]	20
2-7	Constitutional liquation in multicomponent alloys	62
3-1	Bulk chemical composition (wt %) of 718Plus	88
3-2	Heat Treatment Procedures	89
4-1	Semi-quantitative SEM/EDS Analysis (at. %) of particles observed in solution heat treated (1025^{o}C/1 hr) 718Plus	99
4-2	Phase transformation temperatures in 718Plus [25]	100
4-3	Chemical composition, excluding B, C and N, (wt. %), of backfilled and migrated regions of HAZ grain boundaries (GB), and interdendritic constituent in weld fusion zone of 718Plus	115
4-4	Semi-quantitative TEM/EDS Analysis (wt % and at %) of fusion zone constituents of post-weld heat treated 718Plus	154
4-5	HAZ cracking susceptibility of 718Plus during welding and post-weld heat treatment. Weld coupons were pre-weld solution heat treated at 950^{o}C/1hr +AC (coupon A) and 1050^{o}C/1hr +AC (coupon B), respectively	164

Introduction

Alloy 718 is a nickel base superalloy that is used extensively in aerospace applications because of its unique high temperature mechanical properties. Since its invention by Eiselstein [1], it has been the most widely used superalloy material for constructing aero-engine and land based turbine components. However, the recommended service temperature for parts that are made from the alloy is usually limited to intermediate range, i.e., below 650^{o}C. This temperature limitation is necessary to prevent an appreciable loss of strength due to instability of the main strengthening phase of the alloy, γ″ [2]. Above 650^{o}C, the $D0_{22}$ ordered body centered tetragonal phase of γ″ becomes unstable and transforms to an equilibrium delta (δ) phase with orthorhombic (D0a) crystal structure and a plate-like morphology, which impairs high temperature mechanical properties of the alloy. As the operating efficiencies of turbines are being increased continually, their operating conditions are becoming more stringent. Therefore, turbine designers require cost effective alloys with improved high temperature properties. Some nickel based alloys, such as Waspaloy, can be used at higher temperature of up to 700^{o}C; however, Waspaloy does not possess as good weldability as 718 [3]. Therefore, there was a need to develop an alloy that matches the high temperature properties of Waspaloy, but retains the good weldability of 718.

To address the need, ATI Allvac made some recent advances in alloy development by developing a new derivative of Inconel 718, named Allvac 718Plus (UNS N07818) [4]. The alloy is designed to offer a 55^{o}C operating temperature advantage over alloy 718 [5]. This was achieved through major compositional

modifications to 718 that resulted in a change in the main strengthening phase of the alloy from less stable γ″ to a more stable γ′, which is known to improve high temperature strength of superalloys. The differences in 718Plus chemistry compared to that of 718 are the increase in concentration of Al + Ti; the ratio of Al/Ti, the addition of W and especially Co to replace Fe. Such compositional and microstructural changes can have significant effects on the welding and post-weld heat treatment (PWHT) characteristics of the new alloy. It is of significant importance that defect-free welds are produced in critical aerospace components that will be fabricated using 718Plus. Therefore, comprehensive research was initiated to assess and understand the welding and PWHT cracking behavior of the new alloy. Limited or no information is currently available in the literature on the PWHT cracking behavior of 718Plus which may constitute a major difference between its weldability and that of 718. This study will provide a general understanding of the causes of cracking during welding and PWHT of 718Plus. Potentially, it will aid the development of new welding and heat treating procedures that are necessary to minimize or eliminate the occurrence of cracking of the alloy.

Chapter 2

Literature Review

A review of some aspects of physical metallurgy of Inconel 718; 718Plus, high energy beam welding processes, and the fundamental theories of defect formation during welding and post-weld heat treatments of nickel base superalloys are presented in this chapter. The literature review is followed by the objectives of the present research.

2.1 Physical Metallurgy of Inconel 718 Superalloy

2.1.1 Introduction

Alloy 718 is a precipitation hardenable Ni-Cr-Fe base superalloy that was developed by H.L. Eiselstein [6] in the early 1960's. A typical chemical composition range of the alloy is given in Table 2-1 [7]. The alloy was designed to have high yield, tensile and stress rupture properties at temperatures up to 650^{o}C. It is suitable for use within cryogenic to intermediate service temperatures range, i.e., below 650^{o}C. It is widely used as a turbine material in aircraft jet engine, and for high speed airframe parts such as wheels, buckets, spacers and high temperature bolts and fasteners. Also, due to its excellent corrosion resistance, it is widely used in the oil and gas industries as downhole tool components for sour gas wells and pipeline components.

Alloy 718 is strengthened by both solid solution and precipitation hardening mechanisms. The addition of solid solution elements such as Cr and Mo enhances its strength and provides the alloy with its excellent resistance to oxidation. On the other hand, precipitation hardening is provided by the precipitation of ordered γ'' and γ'

Table 2-1: Elemental Composition Range of Alloy 718 (wt %) [7].

Element	**Wt %**
Ni	50.0 – 55.0
Cr	17.0 – 21.0
Fe	Balance
Co	1.0 max
Mo	2.8 – 3.3
Ti	0.65 – 1.15
Al	0.20 – 0.80
Nb	5.0 – 5.5
B	0.006 max
C	0.08 max
Mn	0.35 max
Si	0.35 max
S	0.015 max
P	0.015 max

precipitates in the γ solid solution matrix of the alloy. The contribution from γ′ precipitation is minimal [8], while 718 derives its strength principally from the precipitation of γ′′ precipitates [8, 9]. In the peak aged condition, the volume fraction of γ′′ and γ′ precipitates have been reported to be about 15 % and 4 %, respectively [10]. The heat treatment schedule for 718 may be varied in order to attain the optimum properties required for a given application. For optimum tensile and creep rupture properties, the alloy is commonly solution treated [7] at 927 – 1010^{o}C for 1 hr followed by air cooling to ambient temperature and then aged at 718 – 760^{o}C for 8 hrs followed by furnace cooling at 38^{o}C/hr to 621 – 649^{o}C, held for 8 hrs and finally air cooled to ambient temperature.

2.1.2 Microstructure of Inconel 718

Ideally, a homogeneous alloy 718 in its annealed and aged condition consists of the following phases: 1) nickel γ solid solution matrix, 2) γ′′ precipitates, 3) γ′ precipitates, 4) Nb-rich carbides and Ti-rich carbonitrides, and 5) δ precipitates. However, other phases may be found in 718 as a result of segregation that takes place during casting, and phase formation during high temperature service exposure. These phases may include Laves phase and M_6C carbides, where M denotes one or more metallic atoms. The structure and characteristics of the major phases in 718 are described next.

1. Nickel γ solid solution matrix

The γ matrix of 718 is a FCC nickel base austenitic solid solution matrix that contains solid solution elements such as Cr, Mo, Co, Al and Ti. These elements occupy

substitutional atomic positions in the nickel crystal lattice and differ from Ni in atomic diameter by 1-15 % [11]. Thus, their presence in the nickel lattice results in the distortion of the lattice and produces a spherically symmetrical stress field around them. This stress field can interact with the stress field of a dislocation, giving rise to solute atom – dislocation interaction, and thus strengthen the γ-matrix.

2. γ″ Phase

This is the principal strengthening phase in Inconel 718. It has a DO_{22} ordered body centered tetragonal (bct) crystal lattice structure (Fig. 2-1) which is based on A_3B stochiometry, where A are principally Ni atoms; although some Ni atoms may be substituted by Cr and Fe atoms, while B are mostly Nb atoms with some possible substitution by Ti, Al and Mo. The composition of γ″ in 718 has been reported [12] to be given by $(Ni_{0.53}Cr_{0.21}Fe_{0.01})_3(Nb_{0.13}Ti_{0.06}Al_{0.04}Mo_{0.01})$. It precipitates coherently on {100} planes of γ matrix with an orientation relationship of $\{001\}\gamma'' \| \{001\}\gamma$ and $<100>\gamma'' \| <100>\gamma$ [13] and has a disc-shaped morphology [10]. Although γ″ precipitate has an ordered structure which may contribute to its strengthening ability, it has been reported that the major strength contribution from γ″ to the matrix of 718 in the near peak aged condition is due to coherency strains arising from considerable tetragonal distortion (c/a = 2.04) of its lattice [8-9] due to the mismatch between its lattice and γ FCC lattice of the matrix.

Notable among the properties of 718 are its excellent weldability and formability which generally are attributed to the sluggish precipitation kinetics of γ″ [14]. Unfortunately, the creep and tensile strength of the alloy deteriorate rapidly during

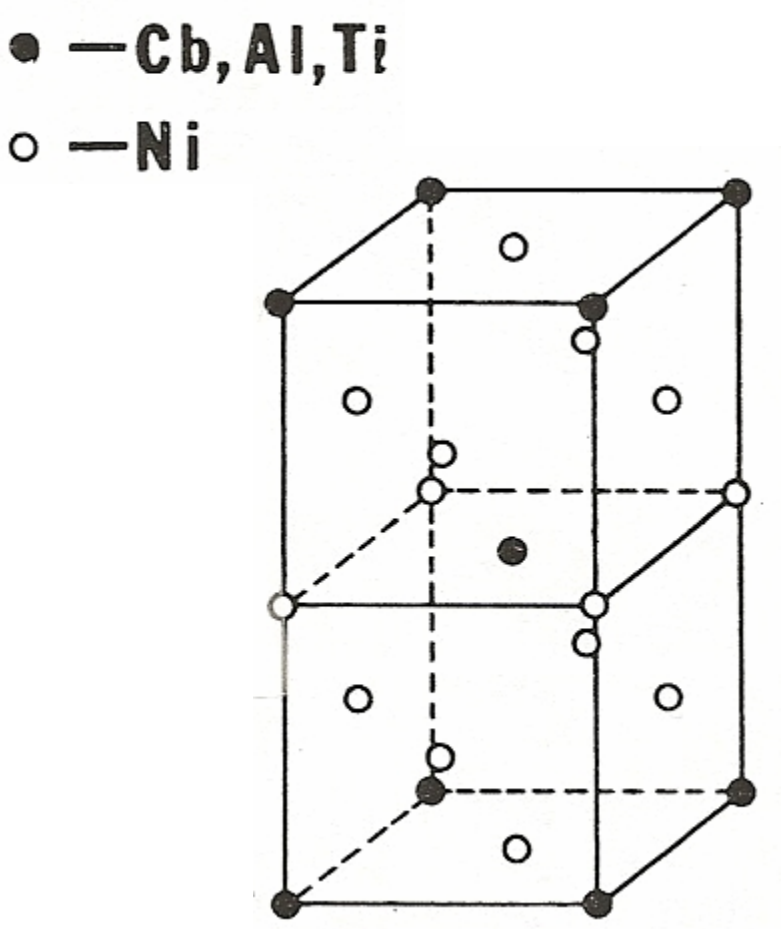

Fig. 2-1: Unit cell illustrating DO_{22} ordered structure of BCT lattice of γ'' phase [10].

service exposure at temperatures above 650°C, which is generally attributed to the instability of γ′′. Above 650°C, γ′′ transforms to a stable δ phase with Widmanstatten morphology, which impairs the high temperature mechanical properties of the alloy.

3. γ′ Phase

γ′ is a FCC $L1_2$ ordered intermetallic compound of the type A_3B (Fig. 2-2). The A atoms are predominantly Ni with possible small content of Co and Fe, while the B atoms are largely Nb with small content of Ti, Al and Mo. γ′ phase in 718 appears as fine spherical particles and is coherent with γ matrix with a cube-cube orientation relationship with the matrix. Unlike other superalloys like Rene 41 and Waspaloy where γ′ contains primarily Ni, Ti and Al, and has very fast precipitation kinetics, the kinetics of γ′ precipitation in 718 is sluggish. This has been attributed to the presence of a considerable amount of Nb in the alloy. The volume % of γ′ in the peak aged condition of 718 is considerably smaller, ≈ 4 %, compared to that of γ′′ precipitate which has ≈ 15 %, and only a small portion of strengthening in 718 is provided by γ′ precipitation in the alloy.

Although both γ matrix and γ′ precipitates have a FCC crystal structure, there is a small difference in their lattice parameters. This difference is commonly called a "misfit" or "mismatch" and its magnitude has a significant importance in determining the morphology of γ' precipitates and the strength of the alloy. It has been reported that γ′ tends to form as spheres for 0 to +/- 0.2% mismatch, becomes cuboidal at about +/- 0.5 to 1%, and is platelike above about +/- 1.25% [15]. The strengthening effect of γ′ is related to the degree of its misfit with γ lattice, particle size, volume fraction, and ordering within its crystal lattice [15, 16].

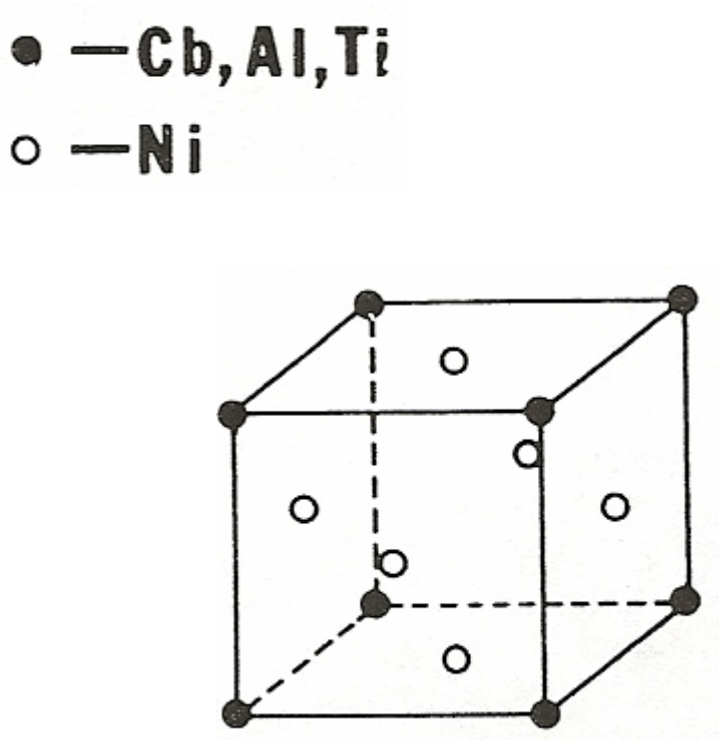

Fig. 2-2: Unit cell illustrating $L1_2$ ordered FCC lattice of γ' phase [10].

4. MC-type Carbides

MC-type (M stands for metal atoms) carbides usually form as primary solidification constituents in 718 during ingot solidification. They form as discrete particles distributed both in inter- and intragranular regions in the alloy. A variant of the carbides which is rich in Nb, with some solubility for Ti atoms, form in 718 with a blocky morphology and have grey coloration when viewed in a light microscope. Apart from the NbC, Ti-rich carbides with some solubility for Nb and nitrogen atoms are occasionally observed in the alloy. Such Ti(C, N) particles are usually angular and have pink coloration when viewed in a light microscope. Both the NbC and Ti(C, N) have a FCC crystal structure. When appropriately distributed at the grain boundaries, MC-type carbides tend to strengthen and prevent or retard grain boundary sliding. Thus, they can improve the stress-rupture properties of an alloy. Also, they may provide dispersion strengthening to the γ-matrix if they are present as finely distributed carbide particles.

5. Delta (δ) Phase

δ phase is a stable Ni_3Nb-type intermetallic with an orthorhombic (D0a ordered) crystal structure. It forms by cellular reaction at lower aging temperatures and by intragranular precipitation at higher aging temperatures. At lower temperatures, γ″ transforms to δ phase at grain boundaries by cellular reaction. During their transformation, a precipitate of delta nucleates with an orientation relationship with one grain and grows into the adjacent grain, pulling the boundary behind. More δ particles nucleate and the duplex cell of δ and γ coherent with the original grain grows consuming the γ″ precipitates [17]. Such a reaction is reportedly controlled by Nb diffusion at the

grain boundaries [18]. Intragranular δ has been also observed and its nucleation was observed to occur at geometric stacking faults within γ″ precipitates [19]. δ can also form at other interfaces such as twin boundaries, and on Laves phase. The crystallographic orientation relationship between δ and γ has been observed to be [19] $\{111\}_\gamma \| (010)_\delta$; $<1\bar{1}0>_\gamma \| [100]_\delta$. The parameters of orthorhombic lattice of δ phase are given by a = 0.514 nm, b = 0.4231 nm and c = 0.4534 nm [19].

The solvus temperature of δ phase depends on alloy composition, especially niobium content, and has been reported to be between 1005 and 1015^{o}C for 718 that has about 5.06 – 5.41 wt% Nb [20]. Its maximum precipitation rate usually occurs at about 900^{o}C. Because of its Widmanstatten morphology, δ phase does not contribute significantly to the hardening of 718. However, its presence in moderate fractions in grain boundary regions is effective in limiting grain growth during solution treatments. It also enhances the stress rupture strength of the alloy [21].

6. Laves Phase

This is a closed packed hexagonal phase with lattice parameters a = 0.47 nm and c = 0.76 nm [22]. It is an A_2B-type intermetallic with Ni, Fe and Cr in the A type atoms and Nb, Mo and Si in the B type atoms. This phase usually forms as irregularly shaped particles and is found in heavily cored or segregated regions in cast 718 or within the fusion zone of its weld. Laves phase is brittle and its presence can be harmful to the mechanical properties, especially ductility, of 718 [23]. It may also tie down alloying elements that are required for formation of the γ′ and γ″, which are essential for

strengthening the alloy. It is possible to dissolve Laves phase during thermo-mechanical processing of cast ingots of 718.

2.2 Physical Metallurgy of 718Plus Superalloy

2.2.1 Introduction

718Plus is a new γ′ precipitation strengthened Ni-Cr-Co-Fe base superalloy that was developed by ATI Allvac [2, 4]. The alloy was designed to have the high temperature stability of Waspaloy while retaining the excellent fabricability of 718. It has excellent high temperature tensile strength and stress rupture performance. Moreover, it can withstand a temperature that is at least 55^{o}C higher than the maximum service temperature, which is about 650^{o}C, for 718 [2]. The alloy offers a lower cost option than Waspaloy or Rene 41 due to its lower intrinsic raw materials cost and improved hot workability [5]. It is available in all product forms: ingot, billet, block, forged round bar, hot-rolled shapes and rectangles, bar, rod, wire, plate, sheet, strip, and castings [5]. Potential applications that are currently being considered or tested for the alloy include aero and land-base turbine disks, forged compressor blades, fasteners, engine shafts and fabricated sheet/plate components [24].

In developing 718Plus, Allvac started with a base composition of 718. However, major chemical modifications were made to the base composition that resulted in an alloy with improved mechanical properties and thermal stability compared to 718. Improved thermal stability was adjudged to be especially important for the new alloy so as to overcome the limitation encountered in the use of alloy 718. The use of alloy 718 is limited to intermediate service temperatures, around 650^{o}C, because its principal

strengthening phase, γ′′, becomes unstable above this temperature and transforms to equilibrium δ phase. Such transformation in the alloy is accompanied by loss of strength and stress-rupture properties. The nominal compositions of 718Plus and 718 are shown in Table 2-2 [2]. The elemental changes that were made to base alloy 718 are highlighted on the table. Al + Ti content were increased to about 4 at %, while a Al/Ti ratio of 4 was maintained. This was achieved through a three fold increase in Al content and a decrease in Ti content. These modifications resulted in a change in the main strengthening phase of the new alloy from γ′′ to γ′ phase, which is more stable at higher temperatures. Furthermore, about 9 wt % Co and 1 wt % W were added to improve the stability of γ′ phase and contribute to solid solution strengthening of the alloy. Finally, the Fe content of the alloy was reduced to 10 wt % in comparison to 18 wt % in alloy 718. The elevated temperature mechanical properties and thermal stability of 718Plus are compared to those of alloy 718 and Waspaloy in Table 2-3 [2]. It is seen that the alloy exhibited properties that are much better than those of alloy 718 and equal or better than those of Waspaloy up to 704^{o}C [2]. In contrast to 718, higher aging temperatures are required to attain optimum proprieties in 718Plus. The recommended heat treatment schedule that is required to optimize the tensile and creep-rupture properties of the alloy comprises of i) solution heat treatment at 954 - 982^{o}C for 1 hr and air cool to room temperature, ii) aging at 788^{o}C for 2 – 8 hrs and furnace cool at 55^{o}C/h to 649 - 704^{o}C iii) isothermal hold at 649 - 704^{o}C for 8 hrs and air cool.

Table 2-2: Comparison of Nominal Composition of 718Plus and 718 [2].

Alloy	Nominal Composition (wt %)											
	C	Ni	Cr	Mo	W	Co	Fe	Nb	Ti	Al	P	B
718Plus	0.02	Bal	18.00	2.80	1.00	9.00	10.00	5.45	0.70	1.45	0.007	0.004
718	0.025	Bal	18.10	2.90	-	-	18.00	5.40	1.00	0.45	0.007	0.004

Table 2-3: Mechanical Properties and Thermal Stability of 718Plus in Comparison with Alloy 718 and Waspaloy [2].

Alloy	ASTM G.S.	Heat Treatment	Tensile Strength at 704°C				Stress Rupture 704°C/552 MPa		Creep 704°C/483 MPa	
			UTS MPa	YS MPa	EL %	RA %	Life Hrs	EL %	$t_{0.2}$ hrs	$t_{0.5}$ hrs
718	6	As-HT [1]	1015	936	20.3	27.5	157.9	19.5	29.0	63.5
		+ 760°C/350 hrs	762	543	53.8	62.3	13.7	34.2	-	-
718Plus	7	As-HT [2]	1174	1005	24.1	30.7	433.1	35.4	226.4	456.1
		+ 760°C/350 hrs	1073	874	42.2	70.0	453.8	34.0	-	-
Waspaloy	6	As-HT [3]	1087	885	38.6	55.4	430.5	27.8	124.0	-
		+ 760°C/350 hrs	998	768	39.2	66.2	259.3	36.7	-	-

[1] heat treatment – alloy 718: 954°C x 1 hr, AC + 718°C x 8 hrs, FC at 55°C/h to 621°C + 621°C x 8 hrs, AC.

[2] heat treatment – 718Plus: 954°C x 1 hr, AC + 788°C x 2 hrs, FC at 55°C/h to 650°C + 650°C x 8 hrs, AC.

[3] heat treatment – Waspaloy: 1018°C x 1 hr, WQ + 843°C x 8 hrs, AC + 760°C x 16 hrs, AC.

2.2.2 Microstructure of 718Plus

The microstructure of 718Plus is similar to that of 718 except that the main strengthening phase in 718Plus is γ′ precipitates with spherical morphology, compared to that of 718 which is disc-shaped γ′′. Therefore, the precipitation kinetics, growth and transformation of the hardening precipitates during thermal exposure of 718Plus is different from that of 718. The volume fraction of γ′ in 718Plus is about 21% [25], compared to about 4% in 718 [10]. Also, as shown in Table 2-4 [25], the γ′ phase in 718Plus contains a higher concentration of Nb. This makes it different from the γ′ phase in other nickel-base superalloys, e.g. Waspaloy, which contains no substantial Nb but is rich in Al and Ti, apart from Ni. It has been reported [25] that the kinetics of precipitation hardening determined by variation in hardness with aging time at 650^{o}C and 704^{o}C, respectively, was much faster in 718Plus than in 718 but slower than in Waspaloy. The slower rate in 718Plus compared to Waspaloy, which contains no Nb, was attributed to the higher concentration of Nb in its γ′ precipitates, as Nb is known to have a slower diffusivity in γ austenite. Also, a study of the growth of particles in 718Plus, 718 and Waspaloy which was reported in the work of Cao [25] showed that the growth of γ′ phase in 718Plus has the lowest rate among the three alloys, implying that 718Plus may have the highest stability in terms of particle growth. It should be noted that the precipitation of γ′′, which is the main strengthening phase in 718, has not been reported in 718Plus. After standard heat treatment [26] and high temperature exposure of 718Plus at 760^{o}C for 350 hrs [27], no γ′′ precipitation was observed in the alloy. Instead, the alloy contained fine spherical γ′ with some δ phase particles. However, rapidly overaged γ′′ precipitates and significant volume

Table 2-4: Crystal structure and chemical composition of γ′ phase in Allvac 718Plus [25].

Crystal Structure		Chemistry wt %								
Lattice	a (Å)	Ni	Co	Cr	Fe	Mo	W	Nb	Al	Ti
FCC	3.62	69	3.0	3.2	1.4	0.5	0.6	14.8	4.8	2.6

fractions of δ phase were observed in 718 that was subjected to similar high temperature exposure [27]. It is known that the microstructural instability of 718 above 650^{o}C is due to the rapid coarsening of γ″ and its transformation to equilibrium δ phase. Thus, the improved stability of 718Plus at higher temperature may be attributed to the absence of the γ″ phase in its microstructure. In alloy 718Plus, the main strengthening phase is γ′ which has a very small misfit with γ matrix and shows a lower tendency for coarsening. Thus, the stability, and the high volume fraction (≈ 21 %) of γ′ provide superior mechanical properties in 718Plus relative to 718. However, this may create some potential weld cracking issues during welding and post-weld heat treatment.

Like 718, other phases which can be found in 718Plus include δ phase, MC-type carbides and Laves phase. These phases have similar crystal structure, but slightly different elemental composition, to those in 718 and which were previously discussed in this review. The compositions of the δ phase, MC-type carbides, and Laves phase found in both 718Plus and 718 are listed in Table 2-5 [25]. The critical phase transformation temperatures of 718Plus have been determined by other researchers [25] through thermodynamic modeling, differential thermal analysis (DTA), and metallography, and are given in Table 2-6 [25].

2.3 Welding, Residual Stresses in Welds and Weld Imperfections

2.3.1 General Introduction

Welding is a process of joining materials, primarily metals, by application of heat, pressure, or both, with or without the use of filler metals, to produce a localized union through fusion or recrystallization across the interface [28]. It is being applied as a viable

Table 2-5: Metallic compositions (SEM-EDS) of δ phase, MC-type carbides, and Laves phase in alloys 718 and 718Plus [25].

Phase	Alloy	Chemistry (metallic elements only) wt %								
		Ni	Co	Cr	Fe	Mo	W	Nb	Al	Ti
δ	718	64.4	-	3.4	5.3	2.2	-	20.4	0.8	3.0
	718Plus	65.1	4.6	1.0	1.4	1.2	0.5	20.1	2.7	3.5
MC	718 (Nb-rich)	3.3	-	1.7	1.2	3.4	-	86.3	-	7.4
	718 (Ti-rich)	1.4	-	0.7	0.8	0.7	-	32.6	-	63.1
	718Plus (Nb-rich)	2.6	0.5	0.8	0.6	0.8	0.5	81.1	-	13.1
	718Plus (Ti-rich)	3.6	0.6	1.7	0.7	0.1	0.2	23.3	-	69.7
Laves (in cast alloy)	718	39.5	-	13.5	13.2	5.8	-	26.5	0.3	0.9
	718Plus	35.2	9.4	11.8	6.2	5.6	1.1	29.7	0.3	0.6

Table 2-6: Phase transformation temperatures in Allvac 718Plus [25].

	Transformation Temperature (^{o}C)		
Phase	**Modeling**	**DTA**	**Metallography**
Liquidus	1346	1353	-
Bulk solidus	1201	1265	1230
MC Eutectic	1261	1292	-
Laves Eutectic	-	1173	-
δ Solvus	1065	-	1002-1018
γ′ Solvus	995	963	954-982
γ′′ Solvus	968	-	-

process for building numerous kinds of structures including aerospace structures, buildings, automotive products, bridges, and industrial transmission pipelines/ pressure equipments. The wide application of welding over other fabrication/ joining techniques, such as riveting and forging, can be attributed to its numerous advantages, which include high joint efficiency, simple structural design, and time/ cost savings. However, welding has its own problems. It often results in various types of defects, which include cracks, porosity, slag inclusion, incomplete fusion, etc. These defects can undermine the integrity of weld fabricated structures. Moreover, due to localized heating that is associated with the welding process, complex thermal and mechanical induced residual stresses are formed in welded materials. These stresses often cause cracking and distortion of welded structures. Nevertheless, welding still remains the most widely used fabrication / repair method. Over the past years, several research and development efforts have been tailored towards the improvement of existing welding processes and procedures so that the integrity of weldments can be improved and fabrication costs can be reduced. Also, a better knowledge of the dependency of the weldability of various alloys on their physical metallurgy has emerged. This section provides a review of existing fusion welding processes, with emphasis on high energy beam welding processes. Also, the residual stresses and weld defects that can undermine the integrity of welded components are reviewed. Finally, the underlying theories of weld defects formation are discussed.

2.3.2 Fusion Welding Processes

From a metallurgical standpoint, there are two basic types of welding processes, namely; solid state and fusion welding processes [29]. Solid state welds are made

between two surfaces in their solid state while fusion welds involve melting of the surfaces to be joined by the use of a heat source. The heat source may be provided by a chemical flame, an arc, an electron beam, or a laser. The sources generally define the three major types of fusion welding processes that are commonly used and listed below:

1. Gas Welding

a) Oxyacetylene Welding (OAW)

2. Arc Welding

a) Shielded Metal Arc Welding (SMAW)

b) Gas Tungsten Arc Welding (GTAW)

c) Plasma Arc Welding (PAW)

d) Gas Metal Arc Welding (GMAW)

e) Flux Cored Arc Welding (FCAW)

f) Submerged Arc Welding (SAW)

g) Electroslag Welding (ESW)

3. High Energy Beam Welding

a) Electron Beam Welding (EBW)

b) Laser Beam Welding (LBW)

Gas welding is a welding process that melts and joins metals by heating them with a flame which is produced by a reaction between fuel gas and oxygen. The most commonly used gas welding process is oxyacetylene welding because of its high flame temperature. The process is schematically illustrated in Fig. 2-3 [30]. Gas flame heats up so slowly, so a large amount of heat is conducted away into the bulk of the workpiece being welded before melting occurs. This could severely damage the metallurgical

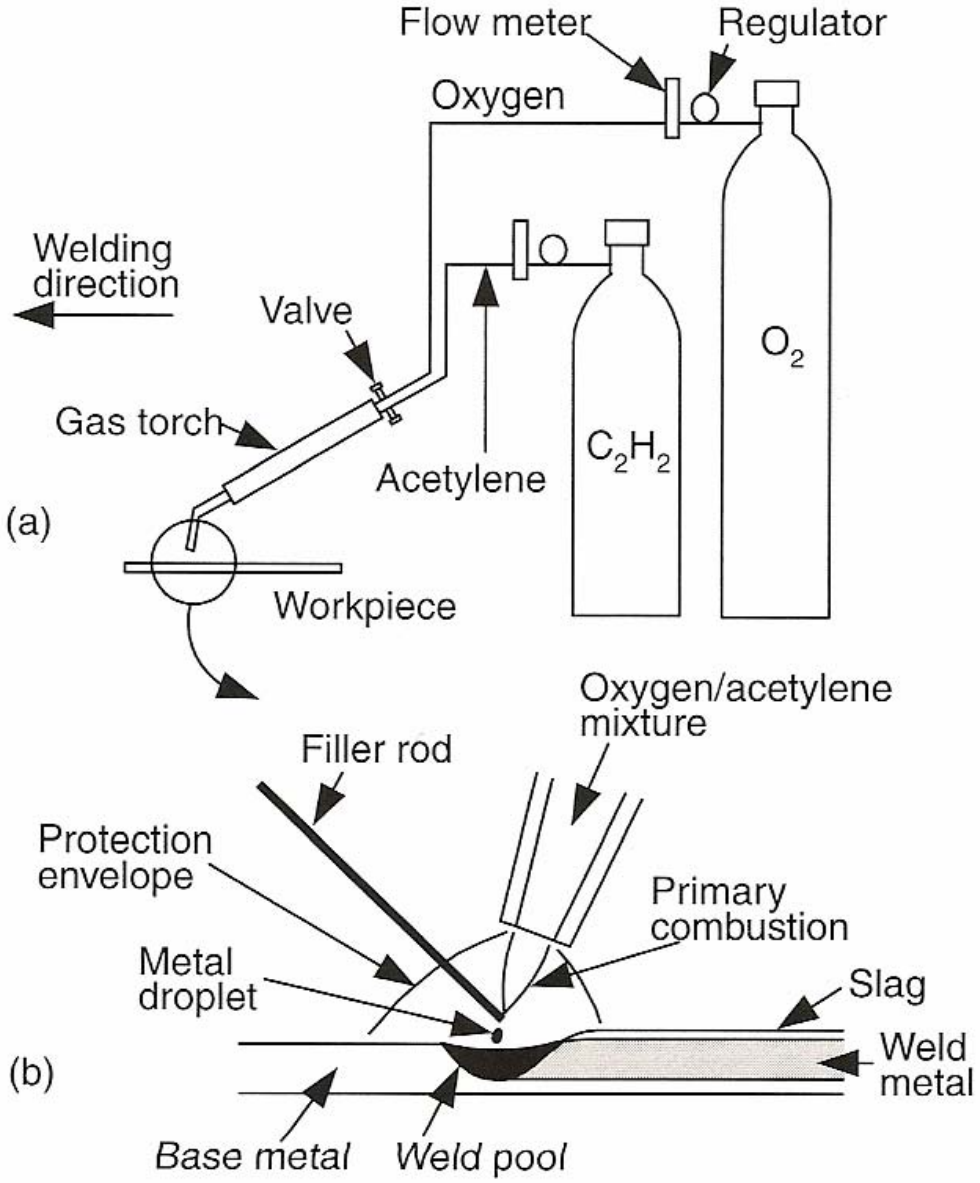

Fig. 2-3: Oxyacetylene welding: a) overall process, b) welding area enlarged [30].

structure of the workpiece and impair its mechanical properties.

Arc welding is the most commonly used fusion welding process [15]. During the welding process, an arc is first struck between an electrode and the workpiece. The heat generated by the arc is used to melt the base/ filler metal. This produces a molten pool that is protected by a slag or an inert gas blanket. Thereafter, the pool solidifies as the heat source retreats from the molten area, forming a solidified weld nugget commonly referred to as fusion zone. Also, a heat affected zone (HAZ) with a different metallurgical microstructure from the weld fusion zone and base metal is formed around the fusion zone. Generally, superalloys can be welded by all arc welding processes, however, Gas Tungsten Arc Welding (GTAW) is most widely used, especially for joining thin sections. The GTAW process is schematically represented in Fig. 2-4 [30]. The melting temperature necessary for welding a workpiece is obtained by maintaining an arc between a non-consumable tungsten electrode and the workpiece. The torch holding the tungsten electrode is connected to a shielding inert gas cylinder and a power source, while the workpiece is connected to the other terminal of the power source. Inert gas from the cylinder passes through the torch and protects the weld pool from atmospheric contamination while also sustaining the arc. For this reason, GTAW is also called tungsten inert gas (TIG) welding. It usually produces clean high-quality, low-distortion welds. However, the deposition rate is low. Also, excessive welding currents can cause melting of tungsten electrode and result in brittle tungsten inclusions in the weld metal. The deposition rate can be improved by using preheated filler metals. In the hot wire GTAW process, the wire is fed into the weld pool and resistance heating can be obtained by passing an electric current through the wire.

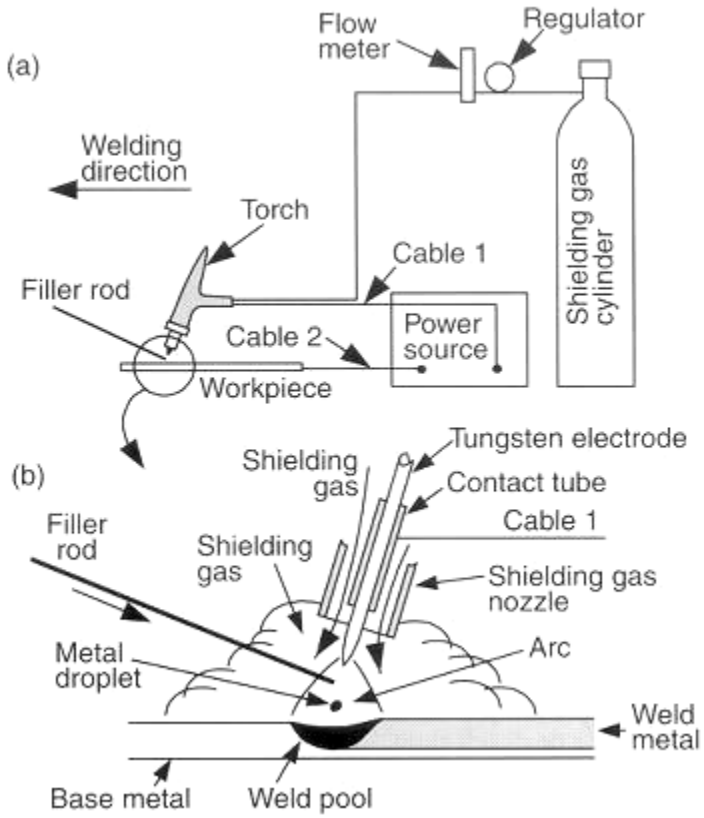

Fig. 2-4: Gas Tungsten Arc Welding: a) overall process,
b) welding area enlarged [30].

2.3.2.1 High Energy Beam Welding Processes

High energy beam welding processes were developed to provide higher welding speeds, deeper weld penetration, and better weld quality with less heat damage to the workpiece. The processes include electron beam and laser beam welding processes which are reviewed next.

2.3.2.1.1 Electron Beam Welding Process [15, 30, 31]

Electron beam welding (EBW) is a high energy density fusion welding process. It works by bombarding the joint to be welded with an intense beam of high voltage electrons which have been accelerated up to velocities of about 0.3 to 0.7 times the speed of light. Upon impact and penetration into the workpiece, the kinetic energy of the electrons is converted to thermal energy. This causes the weld seam surfaces to melt and produce the desired weld joint upon solidification of the molten material.

Figs. 2-5 a & b [30] show schematics of the main components of an electron beam welding equipment and weld joint configuration. The electron beam is produced under high vacuum conditions by employing a triode or anode-style electron gun. As shown in Fig. 2-5 a, the cathode of the electron beam gun is a negatively charged filament that emits electrons when heated up to its thermionic emission temperature. These electrons are accelerated by the electric field between a negatively charged bias electrode, which is slightly below the cathode and the anode. This produces a steady stream of electrons that flow through an aperture in the anode and focused by an electromagnetic coil to a point at the workpiece surface. Power density as high as 10^8 W/cm^2 can be obtained as the total kinetic energy of the electrons and this can be focused onto a small area, typically 0.25 – 1.3 mm in high vacuum, on the workpiece. The very high power density beam generates

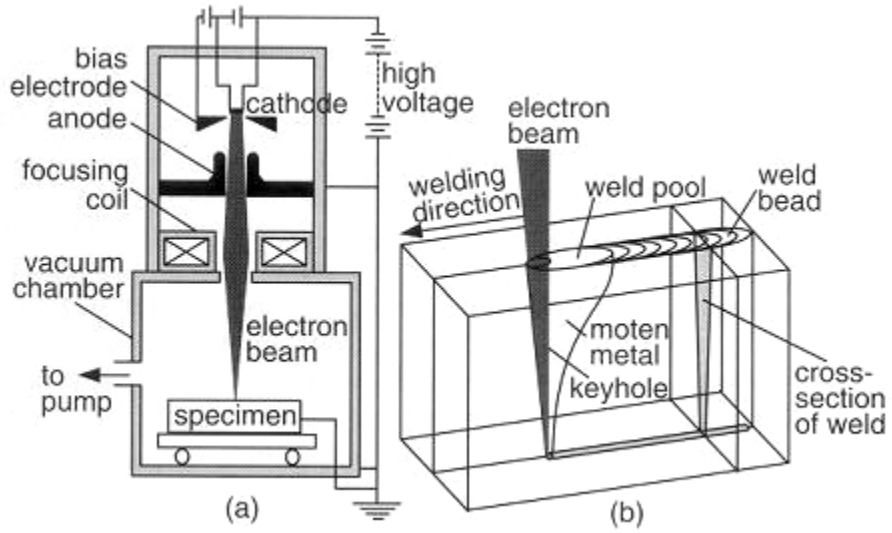

Fig. 2-5: Electron Beam Welding: a) process; b) keyhole [30].

approximate temperature of 14,000^{o}C and vaporizes the workpiece materials to form a vapor hole that penetrates deep into the workpiece. This vapor hole advances along the weld joint as the material at the leading edge of the hole melts. The molten material then flows around the sides of the hole to the trailing edge and then solidifies.

Electron guns are generally operated with applied voltages that vary from 30 to 200 KV, and beam current from 0.5 to 1500 mA. The electron beam gun region is usually maintained at a pressure about 10^{-4} torr or lower. However, the weld chamber housing the workpiece can be maintained in three distinct vacuum environments, namely; 1) high vacuum (EBW-HV) at ambient pressure of about 10^{-6} to 10^{-3} torr, 2) medium vacuum (EBW-MV) at partial vacuum ranging from 10^{-3} to 25 torr, and 3) non vacuum (EBW-NV) at atmospheric pressure in air or protective air.

The principal advantages of the electron beam welding process include:

1. EBW has the ability to make welds that are deeper, narrower, and with a much lower total heat input into the workpiece than arc welding. This enables a high weld depth-to-width ratio in a single weld pass and eliminates the need for multi-pass arc welds. Also, the much lower total heat input of EBW results in a very narrow HAZ and little distortion to the workpiece.

2. Higher welding speeds can be employed due to higher melting rates associated with high power density of the electrons. This increases productivity and results in higher energy efficiency with the EBW process.

3. High quality welds that are free of impurities, such as oxides and nitrides, can be obtained. Also, reactive and refractory metals that are not joinable by arc welding processes can be welded in vacuum using EBW.

Although EBW has numerous advantages, equipment costs are generally higher than those of conventional welding processes. Also, the size of the workpiece that can be welded using EBW process is limited by the size of vacuum chamber employed. For welding that is done in a non-vacuum EBW environment, the maximum working distance between the bottom of the electron beam column and the top of the workpiece is limited to approximately 35 mm.

2.3.2.2 Laser Beam Welding (LBW) Process

Laser beam welding (LBW) is a fusion welding process that produces coalescence of materials with the heat obtained from the application of a moving high density (10^5 to 10^7 W/cm^2) coherent optical energy source called a laser. The laser is an acronym for light amplification by stimulated emission of radiation. The coherent nature of the laser beam allows it to be focused by optical elements, e.g. mirror or lenses, to a small spot. Thus, the focused beam has a high energy density, which allows it to produce a deep-penetrating keyhole weld.

Laser beams can be produced either by a solid-state or gas laser. The schematics of the components of solid-state laser equipment and the laser energy emission process during laser production are shown in Figs. 2-6 a & b. In a solid state laser, a single crystal, e.g. yttrium-aluminum-garnet (YAG), is doped with small concentrations of transition elements or rare earth elements, such as neodymium. When the doped Nd:YAG crystal is exposed to high-intensity flash lamps, the electrons of the dopant element can be selectively excited to higher energy levels. Subsequently, a laser beam is generated when the excited electrons return to their normal energy state, as shown in Fig. 2-6 b. In a

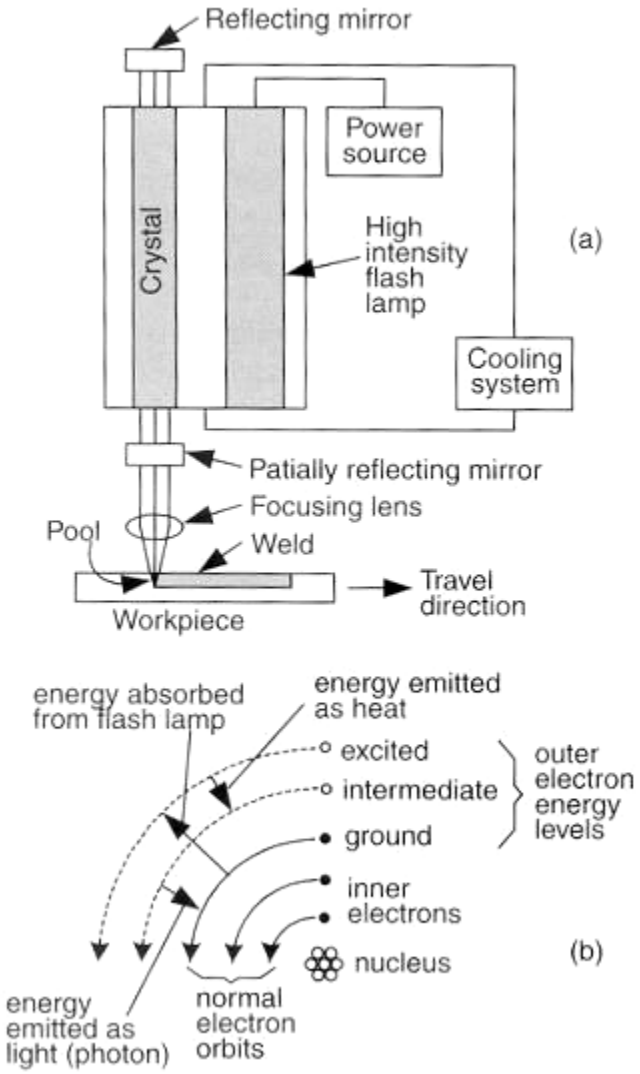

Fig. 2-6: Laser beam welding with solid state laser: a) process, b) energy absorption and emission during laser action [30].

CO_2 laser, a gas mixture of CO_2, N_2, and He is continuously excited by electrodes connected to a power source and lases continuously. A CO_2 laser is generally more powerful than solid-state lasers. Apart from solid-state and gas lasers, other laser techniques that have been developed include semi-conductor based diode lasers.

Laser beam welding offers most of the advantages of electron beam welding. It can produce deep and narrow welds at high welding speeds and with a narrow heat affected zone and little distortion to the workpiece. However, unlike EBW, vacuum and x-ray shielding are not required for LBW. This makes LBW more cost-effective than EBW. On the other hand, because lasers have a very high reflectivity on metal surfaces, the penetration depth of LBW is less than that of high vacuum EBW. For example, as much as about 95% of a CO_2 laser beam power can be reflected by a polished metal surface. The reflection can be significantly reduced by modifying the metal surface, e.g. by roughening, oxidizing or coating it. However, once a keyhole is formed in the workpiece, the absorption of the beam becomes high as it becomes trapped inside the hole by internal reflection. The cost of laser welding equipment is high and precise joint fit-up and alignment is required than in arc welding.

2.3.3 **Residual Stresses in Welds** [32, 33]

The localized application of heat during welding results in a non-uniform temperature distribution in a workpiece. This generates complex thermal stresses during welding and possibly residual stresses and distortion of the parts after welding is completed. As shown in Fig. 2-7 [32], different regions around the weld pool experience a different degree of thermal expansion and contraction as a result of variations in the thermal distribution within the region. As the temperature is increased in the HAZ during welding, the initial expansion of the section is restrained by the material further away from the heat source. The restraint generates compressive stresses in the region which changes with temperature as shown in Fig. 2-7 [32]. The corresponding variation in stress-strain relationship of the material is also shown in Fig. 2-8 [33]. The elastic region of the stress-strain curve is non-linear due to the variation of Young modulus (E) with temperature. At some critical temperature (point 2), the flow stress of the material is exceeded. Further heating results in a decline in stress as the material becomes softer. The flow stress continues to decline until it approaches zero near the peak temperature where considerable plastic strain (compressive yielding) may occur. At this point, the net strain is given by the vector $1 \rightarrow 4$. On cooling, tensile stress (following points $4 \rightarrow 5 \rightarrow 6$) is generated in the region adjacent to the weld fusion zone as the region tends to contract to a shorter dimension than its original dimension due to its inherent compressive plastic strain. The stresses remain in the region as residual stresses after welding. However, if the region had remained completely elastic during the heating cycle, the thermal stresses produced would be relieved when it is cooled to its initial temperature.

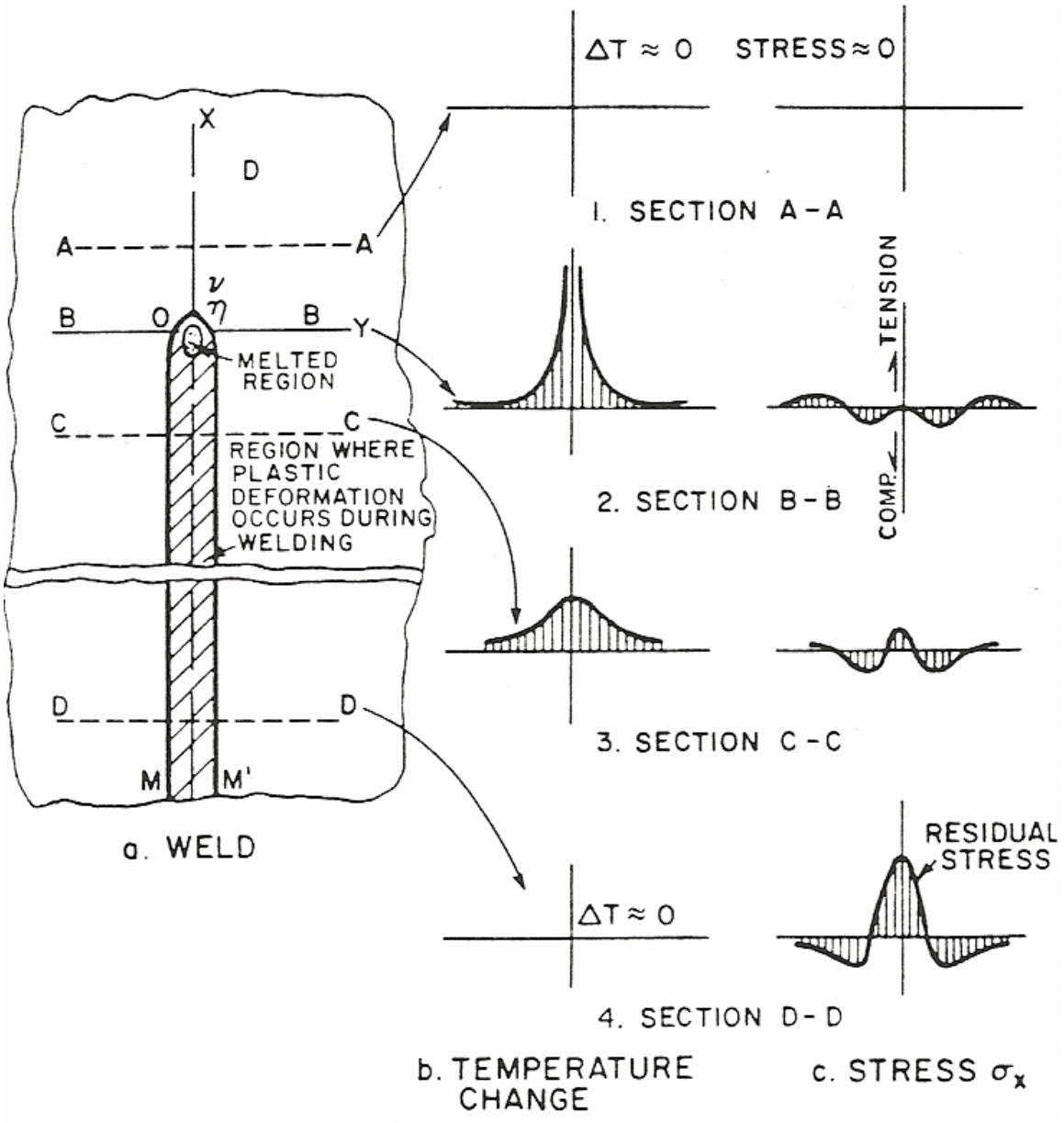

Fig. 2-7: Schematic illustration of changes in temperature and stresses during welding [32].

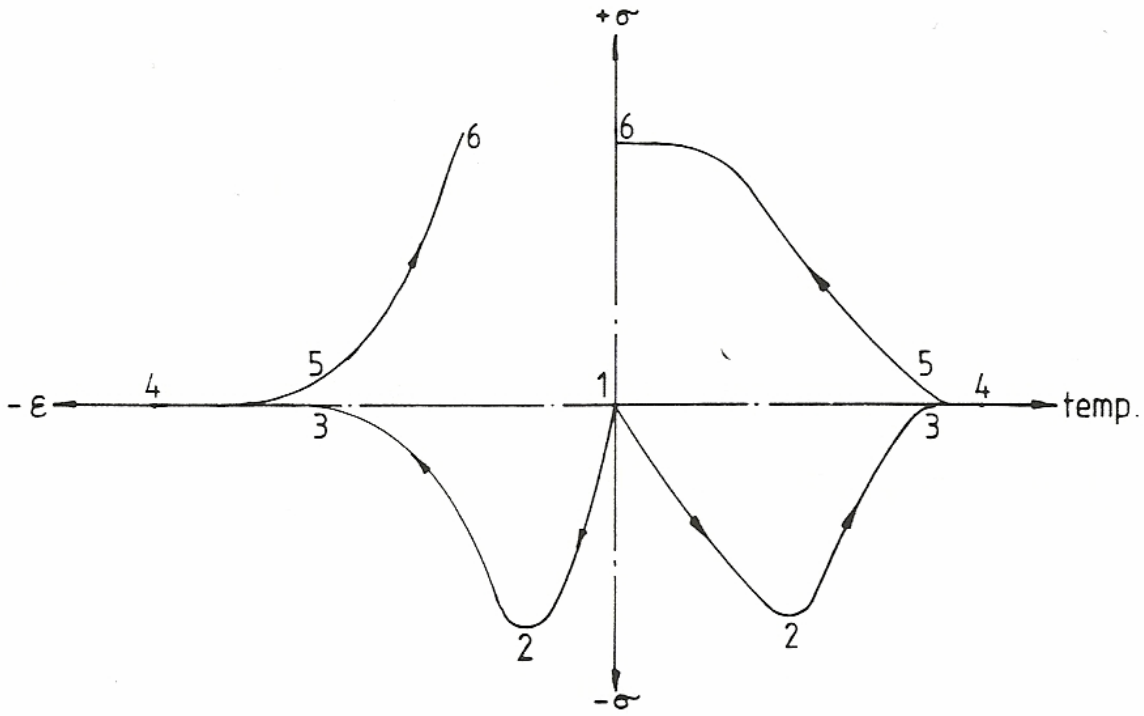

Fig. 2-8: Schematic illustration of changes in stress-temperature and stress-strain during welding thermal cycle. Point 6 refers to the final residual stress and strain after the element has cooled to ambient temperature [33].

The occurrence of cracking during welding of most superalloys has been attributed to the thermal tensile stresses that develop in their HAZ during the weld thermal cycle; apart from the metallurgical factors that also contribute to cracking. Moreover, the residual stresses that result from welding are known to contribute to post-weld heat treatment cracking of the alloys or even reduce their resistance to corrosion failure mechanisms, such as stress corrosion cracking. Therefore, an understanding of how the stresses can be minimized during welding is a key factor in improving the integrity of welded components.

2.3.4 Weld Imperfections

2.3.4.1 Introduction

Weld imperfections are interruptions in the typical microstructure of a weld. These include, lack of homogeneity in the mechanical, metallurgical and physical characteristics of the weldment. Imperfections are also known as faults, discontinuities or flaws. They may be grouped into three classifications; welding process related, design related, and metallurgical. Each of these groups, and associated defects, are discussed next, following ASM welding handbook [34]. Some of the more typical imperfections are shown in Fig. 2-9.

2.3.4.2 Weld Imperfections – Welding Process Related

1. Undercut (Internal or External):

This is a groove melted into the base metal adjacent to the toe, cap or root of a weld and left unfilled by the weld metal. It acts a stress raiser which can cause fatigue problems.

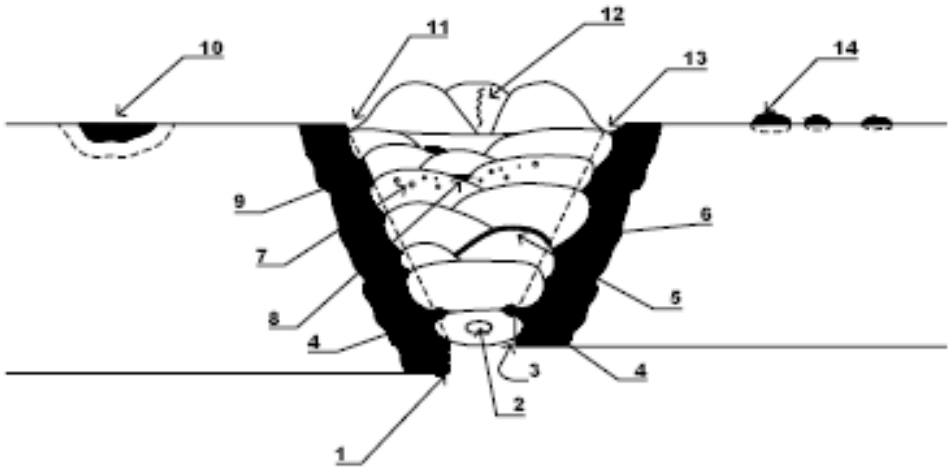

1.	High – Low	2.	Hollow bead
3.	Incomplete penetration	4.	Slag (wagon tracks)
5.	Lack of fusion between passes	6.	Under – bead crack
7.	Porosity	8.	Slag pockets
9.	Lack of side wall fusion	10.	Arc strike
11.	Underfill	12.	Centreline crack
13.	External undercut	14.	Spatter

Fig. 2-9: Weld Imperfections

It can be prevented by decreasing the welding current, travel speed and electrode diameter. Also, electrode angle can be changed so that the arc force holds the weld metal at the corners.

2. Slag Inclusions

The slag inclusions are non-metallic solid materials entrapped in weld metal or between base metal and the weld. They are caused by improper cleaning of welds between passes.

3. Porosity

Porosity is a cavity-type imperfection that is formed by gas entrapment during solidification. It can be caused by the exposure of weld area to contaminants such as oil, paint, rust, moisture or water; ineffective shielding of molten pool from oxygen, and short solidification times.

4. Overlap

An overlap is a protrusion of weld metal beyond the toe, face or root of the weld.

5. Shrinkage Voids

Shrinkage voids are cavity-type imperfections that form by shrinkage during solidification.

6. Oxide Inclusions

The oxide inclusions are particles of surface oxides, usually Al or Mg oxides, which have not melted and are mixed in with the weld metal. The best method of prevention is to clean the weld area thoroughly prior to welding.

7. Lack of Fusion

This defect forms when fusion is incomplete. It occurs when insufficient heat is absorbed by the base metal or weld metal of the preceding pass, causing incomplete melting at the interfaces of the base metal or the preceding weld metal pass.

8. Lack of Penetration

This defect forms when joint penetration is less than specified. It is caused by incorrect welding technique (e.g. low amperage, high travel speed, or wrong electrode angle), improper electrode (too large, wrong type) or improper root gap. It can result in a severe stress raiser which can promote fatigue failure.

9. Craters

Craters are depressions at the termination of weld beads.

10. Arc Strikes (Arc Burns)

These imperfections result from the localized remelting of metal surface. They are caused by inadvertent contact between an electrode and the metal surface. Arc strikes can cause problems as they can change the microstructure of the base metal. Also, they are very hard and can contain cracks due to the rapid solidification of the small amount of melted metal. They must be totally ground away.

11. Underfill

This is a depression on the face of the weld or root surface extending below the surface of the adjacent base metal.

2.3.4.3 Weld Imperfections – Design Related

1. High – Low Condition

This is caused by the misalignment of the pieces that are being welded. It can also occur when the pieces have unequal thicknesses. Its occurrence can cause other imperfections, such as lack of penetration to be formed more readily. Also, it introduces a notch effect at the root of the weldment and may become a severe defect if coupled with lack of penetration.

2.3.4.4 Weld Imperfections – Metallurgical

These are usually crack-type imperfections that are characterized by a sharp tip and high length to width ratio. They include: 1) cold cracking, 2) lamellar tearing, 3) solidification cracking, 4) HAZ liquation cracking, and 5) post-weld heat treatment cracking. Cold cracking and lamellar tearing will be discussed briefly below while the other types of metallurgical imperfections and their formation mechanisms are discussed in detail in the following sub-sections due to their relevance to this study.

1. Cold Cracking:

Cold cracking is the term used for cracks that form after the weld has solidified and cooled. Mostly, it occurs in the HAZ or the weld metal of low alloy and hardenable steels. It occurs under conditions of high restraint and caused by entrapment of atomic hydrogen in susceptible areas, e.g. areas with lattice discontinuities, in the HAZ or weld metal. This embrittles the region, which if under stress can cause cracks to initiate and grow; a term referred as Hydrogen Induced Cracking (HIC). Factors required for cold cracking to occur in steels include: 1) a crack sensitive microstructure i.e. HAZ or weld

metal that is susceptible to hydrogen embrittlement, 2) sufficient concentration of atomic hydrogen, 3) rigid tensile restraint, and 4) a temperature between approximately 300F to -150F. Thus, the cracking can be prevented or minimized by employing the following during welding: 1) low hydrogen consumables, 2) sufficient interpass temperature, 3) clean and dry weld area that is free of hydrocarbon and water, 4) high pre-heat, 5) lower restraining conditions.

2. Lamellar Tearing:

Lamellar tearing is a form of base metal cold cracking that occurs parallel to the surface of a weld plate and adjacent to the weld. It occurs in metals containing non-metallic inclusions such as oxides, sulfides, and silicates that are elongated in the direction of rolling. The inclusions decrease the through-thickness ductility of the metal and result in tearing when weld joints are highly constrained. Lamellar tearing can be prevented by using clean steels in locations where the design of the equipment would make this a potential problem.

2.3.4.4.1 Solidification Cracking in Welds

Solidification cracking is an imperfection that can occur in the fusion zone of welds. It results from the inability of the semisolid weld material to accommodate thermal shrinkage strains that develop during weld cooling and solidification [35]. As solidification of weld liquid reaches a terminal stage, the shrinkage associated with it could cause tensile stresses to develop within the semisolid weld metal, which is constrained from shrinking by adjacent rigid base metal. At this stage, the presence of liquid films between the grains of the solidifying metal could reduce their surface-to-

surface contact strength, thus lowering the strength and ductility of the weld metal. Therefore, the weld metal is in a crack susceptible state, and will crack when the tensile stresses generated exceed the cohesive strength of the grains. The factors that affect the susceptibility of an alloy to solidification cracking during welding are both metallurgical and mechanical in nature. These factors include;

1. Solidification temperature range of weld pool: the presence of a liquid film on grain boundaries during the terminal stage of solidification can drastically reduce the surface – to – surface contact strength of the grains and lower the strength and ductility of the weld metal. Therefore, a wider solidification temperature range, which can result from the presence of positively partitioning elements (elements with k <1) in an alloy, would widen the region of weakness and increase the susceptibility of an alloy to solidification cracking.
2. Amount of liquid during terminal stage of solidification [30]: the schematic in Figs. 2-10 a – f describe the effects of the amount of terminal liquid on the crack susceptibility of an alloy during solidification. A pure metal is not susceptible to cracking because there is no low melting point eutectic present at the grain boundaries to cause solidification cracking. In highly alloyed metal, on the other hand, the eutectic liquid can be enough to heal incipient cracks. Somewhere in between, however, the liquid volume between grains can be just large enough to form a thin, continuous grain boundary film to make the alloy rather susceptible to solidification cracking and without extra liquid for healing cracks. A fine equiaxed dendritic structure with abundant liquid between grains (Fig. 2-10 f) can deform more easily under stresses than a coarse columnar dendritic structure and,

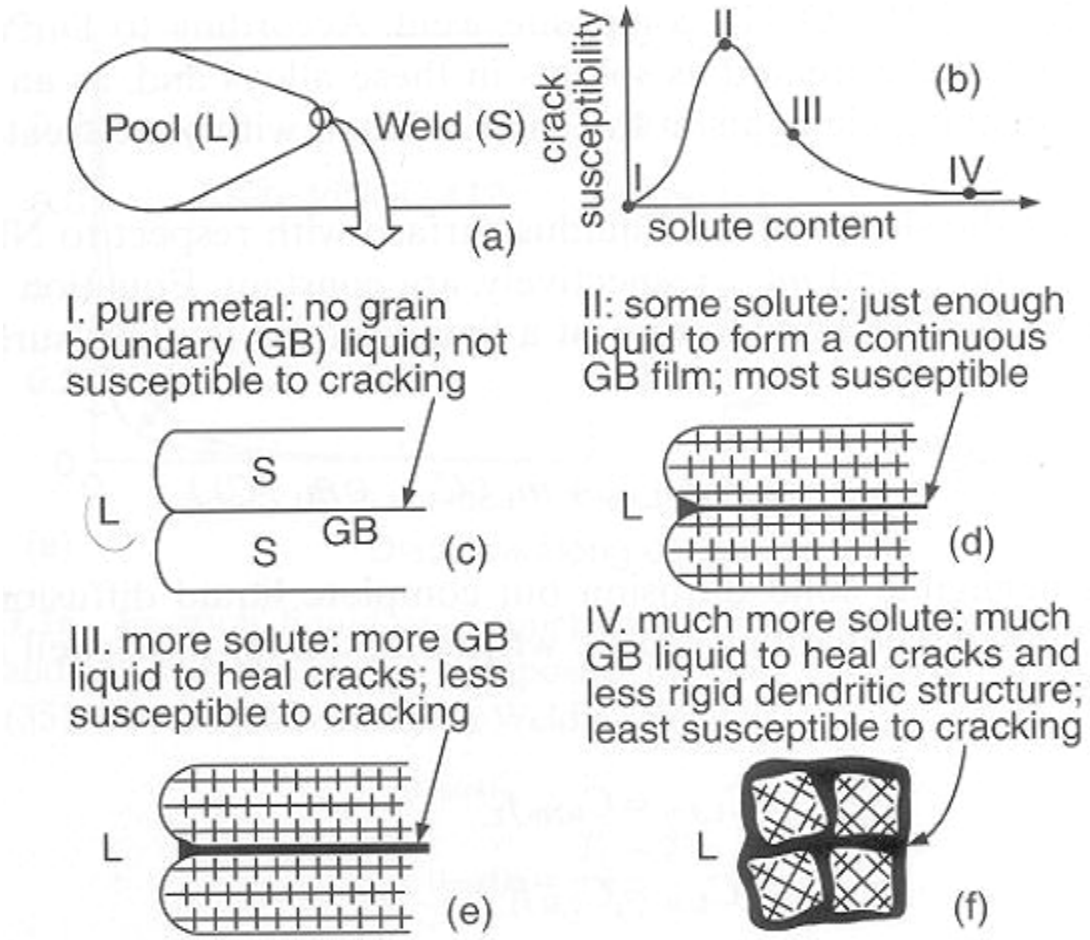

Fig. 2-10: Effect of the amount of liquid on crack susceptibility: a) weld, b) crack susceptibility curve, c) pure metal, d) small liquid amount e) more liquid, and f) much more liquid [30].

thus, is less susceptible to cracking. This pattern has been reported by some researchers [36 – 41] who observed variations in the cracking susceptibility of aluminum alloys, depending on their solute content, which determines the amount of terminal liquid. Michaud et al [41] reported an increase in total crack length of Al with an increase in Cu concentration up to 4 wt %. However, the addition of Cu beyond 4 wt % resulted in a decrease in the degree of solidification cracking in the alloy.

3. Liquid distribution: in addition to the amount of liquid present between adjoining grains, the distribution of the liquid also has a significant effect on solidification cracking. For the liquid to easily cause cracking, it must wet and spread out over a wider grain boundary surface area. Otherwise, it will be more localized, which will create a smaller area of liquid – solid contact and more solid – solid bridging that can improve the resistance of the alloy to cracking. Elements such as boron, sulphur, etc, may increase the wettability of liquid on grain boundaries of iron and nickel base alloys [35], so they are normally added to the alloys in controlled amounts to minimize cracking.
4. Grain structure of weld metal: fine equiaxed grains are often less susceptible to solidification cracking than coarse columnar grains [42, 43]. This is attributed to the better ability of fine equiaxed grains to deform in order to accommodate contraction strains [30]. Liquid feeding and healing of incipient cracks can also be more effective in fine equiaxed grains.
5. Magnitude of contraction stresses: even if an alloy has a crack – susceptible microstructure, no solidification cracking would occur without the presence of

sufficient tensile stresses acting on adjoining grains during solidification. The stresses can be produced by thermal contraction or solidification shrinkage (or both) that accompany solidification of the alloy. As a result, alloys with high thermal expansion coefficients and high solidification shrinkage, e.g. aluminum alloys, are susceptible to solidification cracking [44].

6. Degree of restraint: joints with higher degree of restraint are usually more susceptible to solidification cracking, as compared to those that are unrestrained. The practical approach taken to minimize cracking is to reduce overall weld restraint by proper design of weld joints [35], for example, weld joint gaps are kept at a minimum by using hardware with good fit-up or designing the joint as a standing edge for small parts.

The theories governing solidification cracking are reviewed below.

2.3.4.4.1.1 Theories of Solidification Cracking

2.3.4.4.1.1.1 Shrinkage Brittleness Theory (SBT)

This theory is based on the view that cracking occurs in the brittle temperature range (BTR) during solidification. The upper temperature limit of the BTR is defined by the solidification stage when dendrites come into contact with each other and interlock, thus, preventing the flow of liquid around them [45, 46]. The temperature at which this occurs is also known as the coherent temperature. The lower temperature limit of the BTR is the temperature at which the strength of grain boundaries is sufficient to absorb the loads imposed upon them. The origin of shrinkage brittleness theory (SBT) results from numerous studies [36, 47 – 49] of hot cracking (tearing) of aluminum alloys, but is

equally applicable to other alloy systems. Thus, the mechanism of cracking as described by SBT is described next.

At some time during solidification, primary solid dendrites grow until they come into contact and interlock to form a coherent network. During subsequent cooling beyond the coherent temperature, contraction strains develop, and when the critical rupture stress is exceeded, a rift will occur in the network. The rift (fissure) will persist if there is insufficient liquid to heal it. Once the alloy is cooled below the lower limit of BTR (solidus), fissures are unlikely to form because it is assumed that the solid metal is ductile at sub-solidus temperatures. Therefore, cracking is only likely to occur in the BTR [45], between the coherent temperature and solidus, which is graphically shown in Fig. 2-11.

The BTR of an alloy lies within its solidification temperature range; therefore, it is dependent on the composition of the alloy. Also, it is affected by liquid distribution and the factors that influence it. The experimental observations of Pumphrey and Jennings [49] led them to conclude that during the solidification of an alloy, coherency is gained when the amount of interdendritic liquid (as distinct from liquid entrapped within dendrite arms) falls below approximately 5%. A eutectic alloy that contains 5% or more of interdendritic liquid will not gain coherency until the eutectic temperature is reached, consequently it will possess no brittle temperature range. This is confirmed by the fact that aluminum binary and tertiary alloys show no tendency to cracking when the total alloy content exceeds a certain level.

Vero [47] introduced the concept of “healing” whereby incipient cracks are considered to be filled with liquid and their harmful effects are, thus, overcome. He postulated that if a solidifying metal contains more than a critical volume of eutectic, any

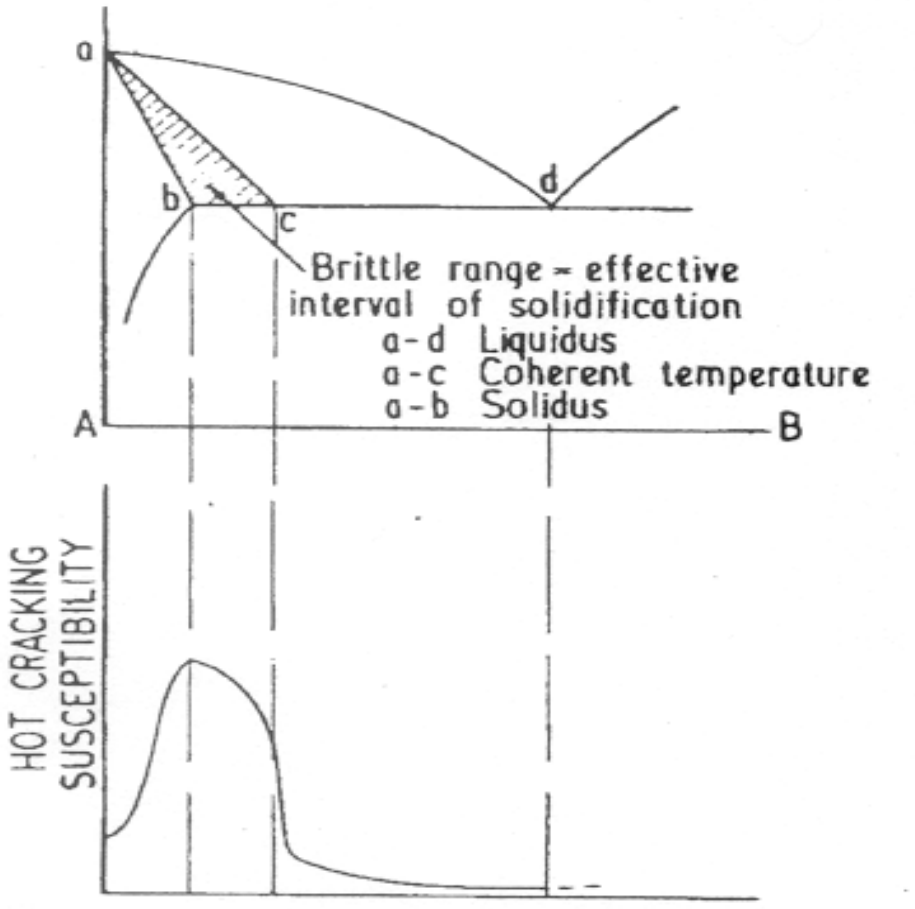

Fig. 2-11: Hot cracking susceptibility of eutectiferous alloys [45]

crack formed by the contraction of the primary crystals would be healed by the inflow of eutectic liquid. Pumphrey [49] later introduced the concept of "accommodation" and distinguished it from the concept of healing. Accommodation was defined as the degree to which an alloy is able to withstand shrinkage strains by movement of grains within the solid-solid mass when the alloy is solidifying in the BTR, thus preventing cracking. It was argued that in welds and small castings, accommodation is more likely to occur than healing, because for healing to occur there needs to be a critical volume fraction of liquid which may not be present in most cases.

These various ideas were expanded by Medovar [50], who stated that the variation of hot cracking with alloying additions, for elements which form continuous solid solutions, is determined by the length of the freezing range. If the alloying elements are mutually soluble in either the liquid or the solid state, then hot cracking should not occur. For systems that do form primary solid solutions, very small additions of second element may cause severe cracking, owing to the increase in the freezing range.

2.3.4.4.1.1.2 Strain Theory of Hot Cracking [51]

The strain theory of hot cracking was proposed by Pellini and his co-workers [51 - 53]. In their proposition, they suggested that hot cracking is caused by localized strains. These strains are set up by thermal gradients and tend to tear apart masses of solidifying materials, which are separated by "continuous thin liquid films." It was argued that hot cracking does not occur in the "mushy" stage of solidification since the shrinkage strains are uniformly distributed. Cracking only takes place when liquid film stage is reached and localized strains are exceedingly high.

In order to appreciate the strain theory it is necessary to understand the concept and significance of the liquid film stage. In passing through the solidification temperature range, irrespective of whether the process entails heating or cooling, an alloy will develop a condition of essentially continuous liquid film near its solidus. The strength and ductility of a mass of solid grains separated by continuous liquid film is extremely low. Thus, the time/temperature period in which the film exists is very critical. If the grain boundaries contain a continuous network of low-melting segregated material, the liquid film would form near the solidus temperature of the segregate. However, as the composition of an alloy approaches that of a pure metal, the amount of segregated material which may be formed is greatly reduced. Hence, the distribution of the segregate becomes less continuous and less effective in lowering the film stage temperature. The significance of the film stage is that separation can occur, as shown in Fig. 2-12, through the liquid films which exist near either the true solidus temperature of the metal or in the range of temperatures between the true solidus and the effective solidus of the segregated material.

Figs. 2-13 a-c taken from Pellini [51] illustrates schematically the process of combined hot cracking of weld and HAZ. As the liquid pool behind the arc passes the segregate region, melting occurs between the grains; the lateral distance from the weld that develops melting is determined by the thermal gradients perpendicular to the welds and, thus, by welding parameters. Fig. 2-13 a shows that grain boundary melting occurs to the distance at which the gradient temperature corresponds to the solidus temperature of the segregate film. At this stage, the HAZ is in a state of compression due to the thermal expansion of the hot metal near the fusion zone. As the arc passes on, cooling

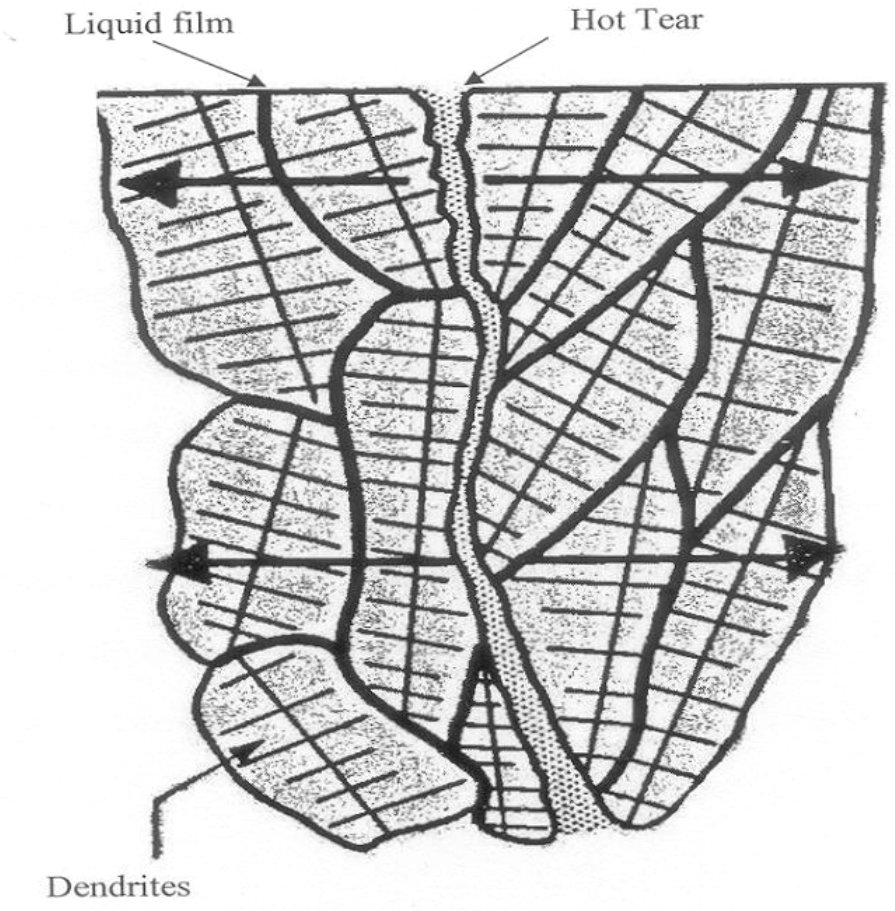

Fig. 2-12: Schematic illustration of hot cracking in castings by fracture through interdendritic liquid films existing near solidus temperature [51].

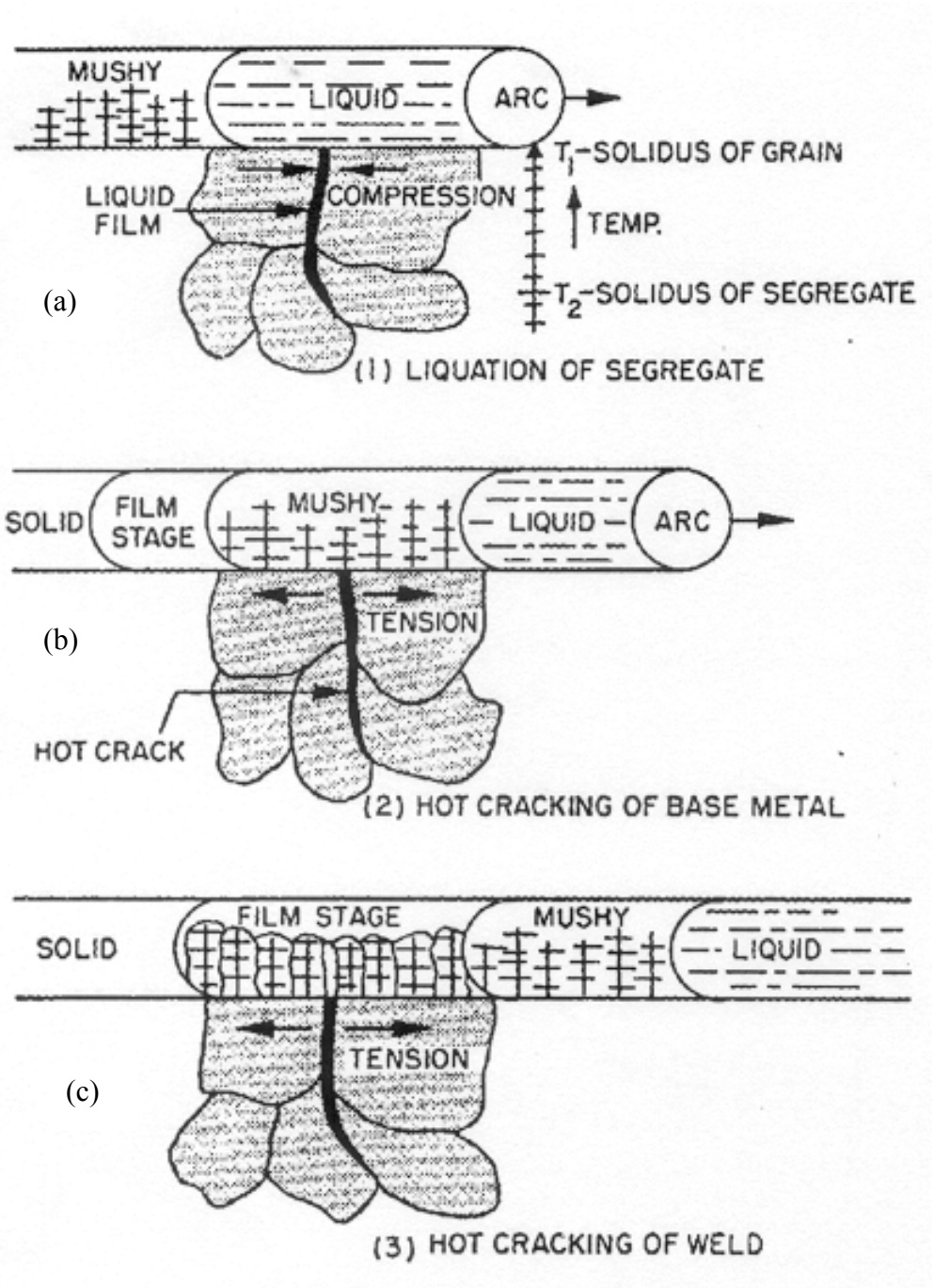

Fig. 2-13: Schematic illustration of weld hot cracking processes a) liquation of segregate, b) hot cracking of base metal c) hot cracking of weld [51].

takes place and the HAZ contracts. This results in the development of tensile stresses which cause parting of the film region and cracking in the HAZ. At this point, the weld metal is in a mushy condition, thus hot tearing would not occur. At a later time, however, the weld metal reaches the film stage and a strain concentration is developed at the HAZ.

Pellini [51] used the strain theory to explain the reason why liquid films formed by segregated species are more effective in causing hot cracking than the liquid films which form at the true solidus during solidification of an alloy. The strain theory provides a generalized mechanism of hot tearing in terms of the time-rate of extension developed in the liquid film stages. Based on this theory, the presence of liquid film leaves an alloy in a metallurgical condition that permits hot tearing. However, the actual occurrence of hot tearing is determined by mechanical factors inherent in the rate of extension per unit time imposed within the short time before the liquid film solidifies. In a non-segregated condition, the metal passes through the film stage over shorter times, while under segregated conditions the liquid film condition exists over a wider range of temperature, i.e. for a longer time. Therefore, the rates of extension which do not develop sufficient separation of the liquid film to cause fracture in shorter times may be very effective with longer times, since the separation developed in the films is additive with time. The strain theory rebuffs the assumption that hot tearing may occur when the solidifying metal is in the mushy stage. As illustrated in Fig. 2-14, it is believed that stresses/ strains are more evenly distributed at this stage, and also that stress relaxation occurs by general flow of the pasty mass. However, as the hot zone approaches liquid film stage, its extension is necessarily forced into narrow liquid films, which have no appreciable strength and ductility compared to the adjoining solid. The occurrence of hot cracks resulting from the

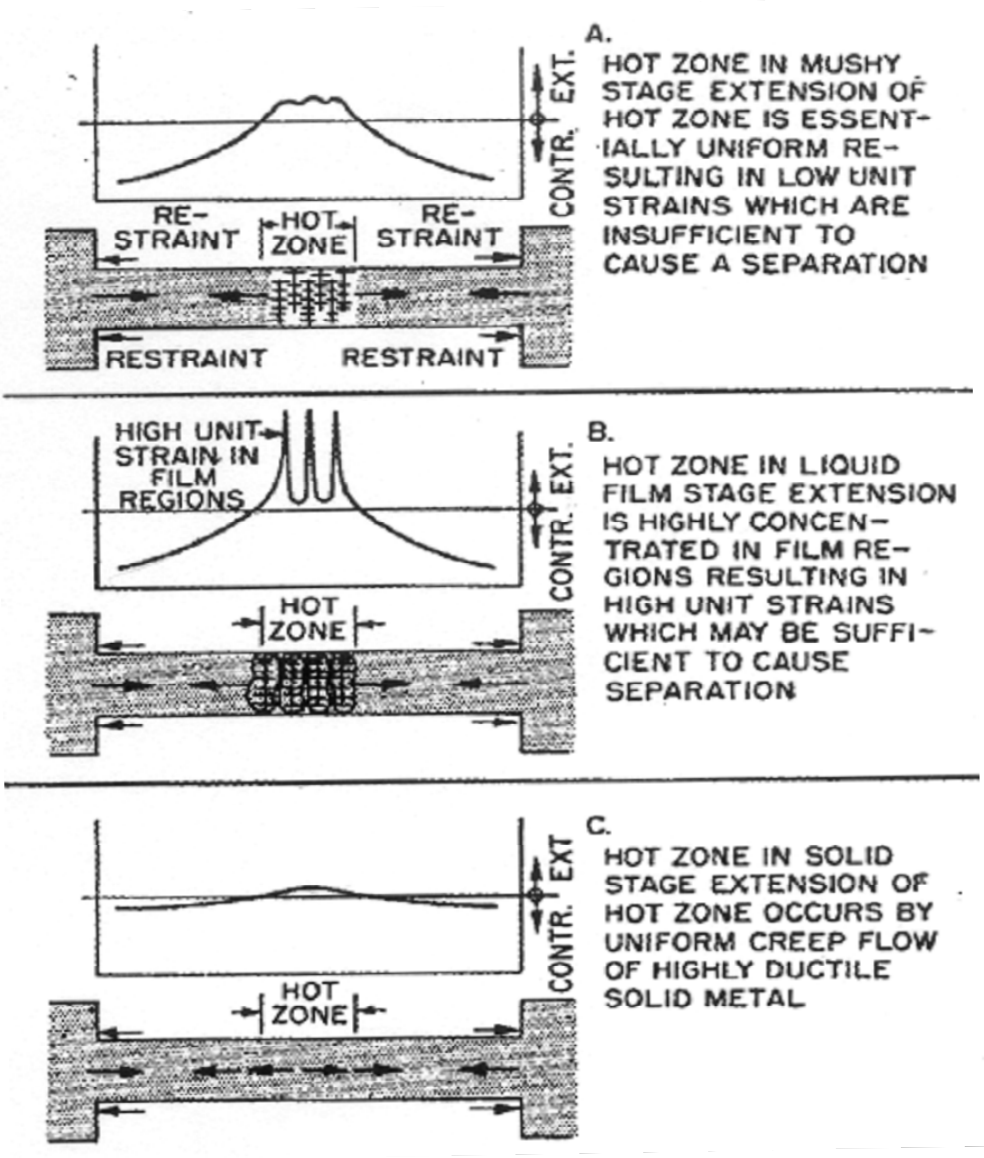

Fig. 2-14: Schematic illustration of strain distribution during various stages of solidification in a casting system containing hot spot [51].

comparatively high value of strains developed at the liquid film stage is illustrated in Fig. 2-15. The several observations of interrelated effects of metallurgical and mechanical variables led Pellini [51] to generalize the hot cracking problem to the following principal elements:

1. The primary mechanical factor that determines hot cracking is the time rate of extension of the hot zone during its liquid film stage of solidification. If the liquid film stage lasts for only a relatively short time, hot cracking will occur only if a sufficient rate of extension is forced on the film regions during this short time.
2. The rate of extension of the liquid film regions depends on: (a) the overall extent of the hot zone, (b) the degree of mould restraint, and (c) the cooling rates of the adjoining sections of the hot zone.
3. The presence of positively partitioning elements ($k<1$) extends the liquid film condition to lower temperatures and therefore increases the duration of the film stage.
4. The longer the interval of the liquid film stage, the greater is the total amount of separation that develops in the films.

2.3.4.4.1.1.3 Generalized Theory of Super-solidus Cracking [45, 46]

The generalized theory of super-solidus cracking was proposed by Borland [45, 46] to include relevant ideas from both shrinkage-brittleness and strain theories. It emphasized the effects of solidification mode, interphase / grain boundary energies and solute additions on hot cracking susceptibility of an alloy.

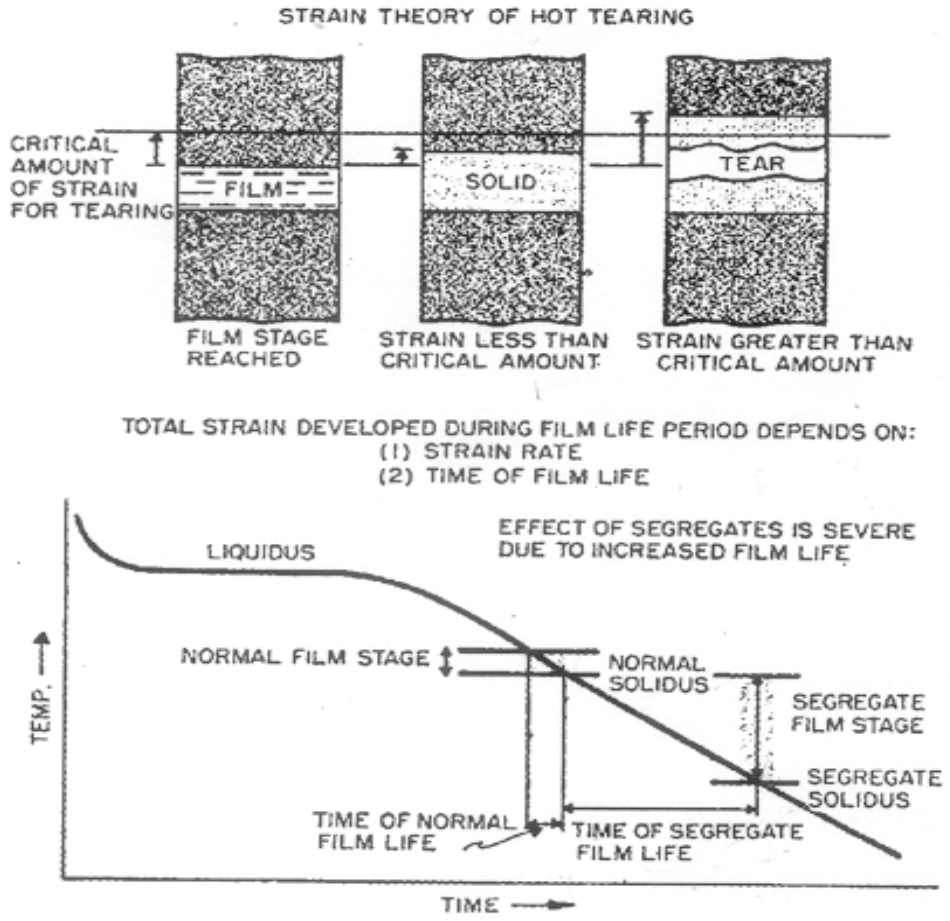

Fig. 2-15: Schematic illustration of strain theory of hot cracking [51].

The solidification sequence of a molten alloy was divided into four stages, as shown in Fig. 2-16, and described below:

1. Stage 1 – primary dendrite formation: the solid phase is dispersed while the liquid is continuous. In this stage, both the liquid and solid phases are capable of relative movement.
2. Stage 2 – dendrite interlocking or coherent stage: both the liquid and solid phases are continuous, but only the liquid is capable of relative movement and is able to circulate freely between the interlocking dendrites.
3. Stage 3 – grain boundary development: the solid crystals are in an advanced stage of development and the semi-continuous network restricts the free passage of liquid. Relative movements of the solid and liquid phases are impossible at this stage.
4. Stage 4 – complete solidification of the remaining liquid.

Borland [45, 46] suggested that materials are susceptible to cracking once the coherent temperature is reached at stage 2. However, if a crack is initiated at this stage, it is possible for it to be healed by the flow of liquid into the fissure formed, particularly if a relatively high volume fraction of liquid is present. At stage 3, the formation of solid crystals would have reached an advanced stage, therefore, the flow of liquid will be restricted and no crack healing will occur. This stage is referred to as the "critical solidification range (C.S.R)" and its commencement temperature is referred to as critical temperature (T_c). According to the generalized theory, cracking

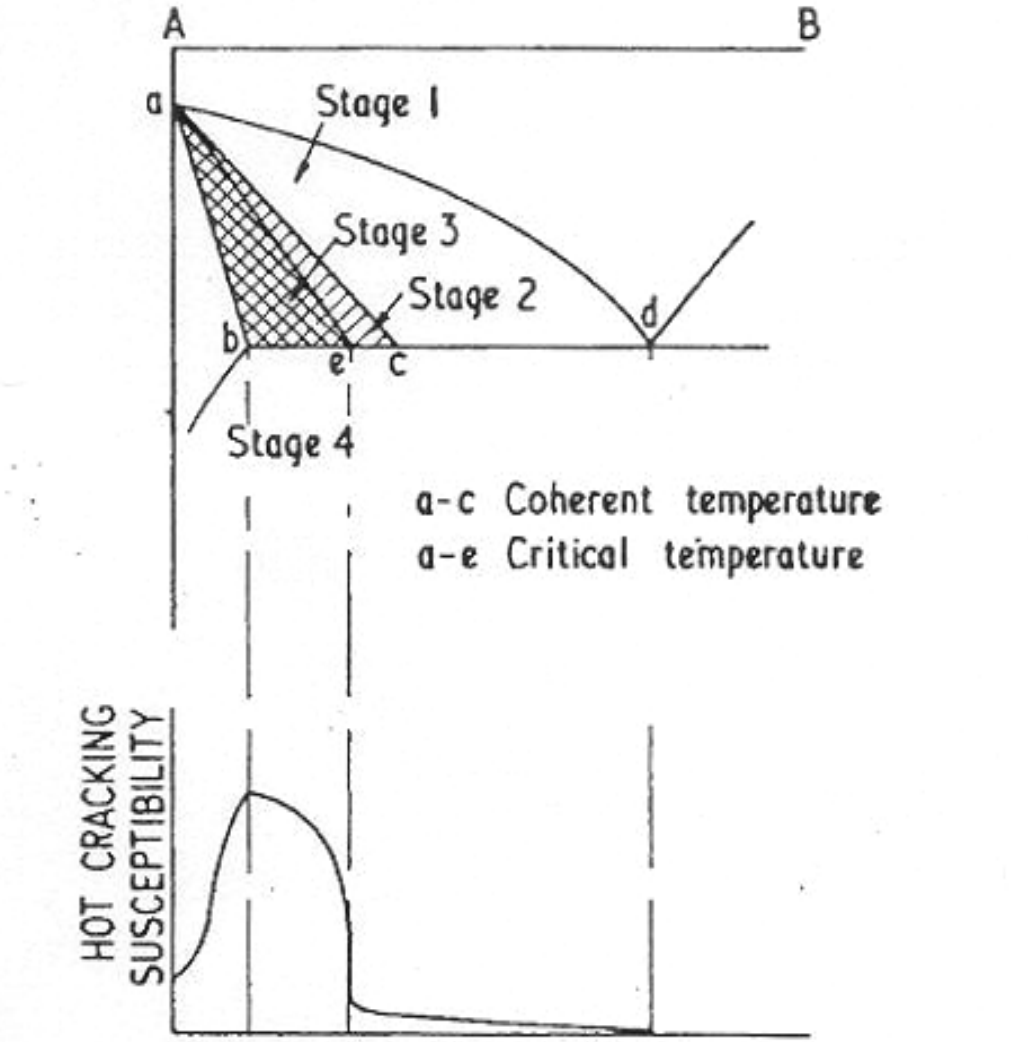

Stage 1—Dendrites freely dispersed in liquid. No cracking
Stage 2—Interlocking of grains. 'Liquid healing' possible if cracks form. 'Accommodation' not important
Stage 3—Critical solidification range. No 'healing' of cracks possible if 'accommodation' strain exceeded
Stage 4—Solidification. No cracking
a-c-e—Brittle range

Fig. 2-16: Effect of constitutional features on cracking susceptibility in binary systems (Generalized theory) [45].

can occur when there is a build up of high stresses between grains or where by reason of lack of constraint, a parting of the liquid phase can occur as a result of the development of highly localized strains. In concept, the generalized theory is very close in concept to strain theory, except that it considers the possibility of cracking during mushy zone stage of solidification as suggested by shrinkage–brittleness theory.

For cracking to occur, an alloy should not only pass through a liquid – solid stage, but the liquid should be present over a relatively wide temperature range to allow the build up of high stresses between grains. The liquid should also be continuous along the surface of the grains. The distribution of liquid along grain boundaries depends on the free energies of the grain boundaries (γ_{SS}) and solid-liquid interphase energy (γ_{SL}), which is related to the liquid – grain boundary dihedral angle θ as given by:

$$\frac{\gamma_{SL}}{\gamma_{SS}} = \tau = \frac{1}{2COS\left(\frac{\theta}{2}\right)} \qquad (2\text{-}1)$$

The value of τ is of particular importance to grain boundary liquid distribution, as summarized below and schematically illustrated in Fig. 2-17.

When,

$\theta = 0^o$, $\tau = 0.5$ $\Rightarrow$ Liquid forms as continuous films on grain surfaces

$\theta = 60^o$, $\tau = 0.57$ $\Rightarrow$ Liquid forms at grain edges

$\theta > 90^o$, $\tau = 0.7$ $\Rightarrow$ Liquid forms on grain corners

A value of τ near 0.5 would allow liquid to remain at grain faces as an almost continuous film and prevents their quick joining. If this condition exists over a relatively large temperature interval, it will allow stresses to build up locally to a critical amount to cause cracking between grains. A higher value of τ, say 0.57, would allow liquid to form at

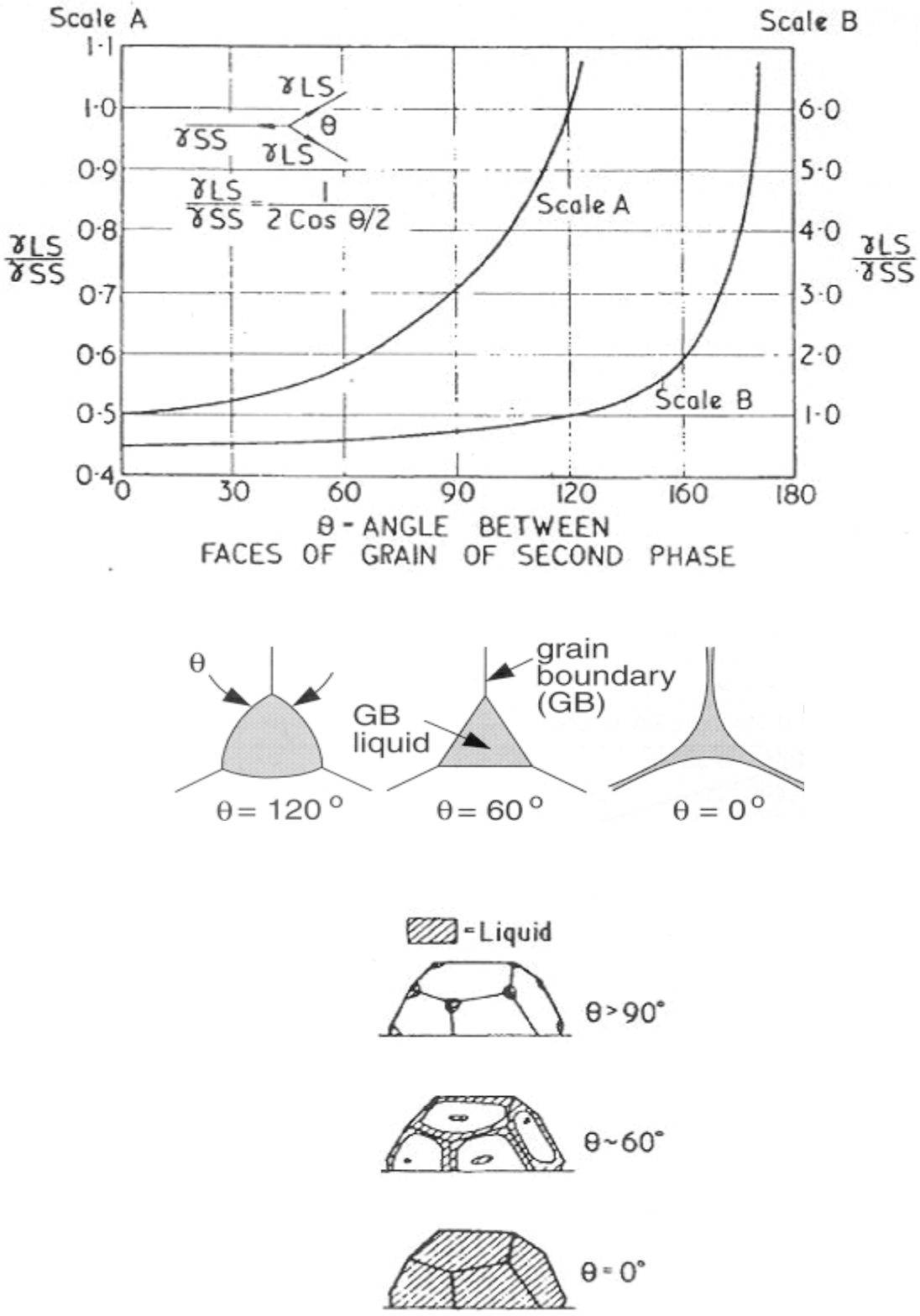

Fig. 2-17: Effect of dihedral angle (θ) on the shape and distribution of liquid phase on grain corners, edges and faces [45].

grain edges while grain faces join and provide a strong bond, and thus prevents the formation of cracking. In alloy systems where solid solutions form over an extended composition range during solidification, wetting of the grain faces and edges will almost be complete. If this occurs in a weld over a relatively large temperature interval while the weld solidifies, then cracks could form easily, since only small areas of the grain surfaces will be joined. When metals are immiscible in the molten state and one metal solidifies, τ will be much greater than 0.5. Thus, the liquid will be largely confined to grain edges and corners, thereby reducing susceptibility to cracking.

The C.S.R of an alloy is also affected by its solute content. With an increase in solute concentration, Tc will be depressed because a greater amount of liquid will persist to lower temperatures. Also, the solidus will be lowered due to changes in solid solubility. As the extent of the non-equilibrium solidification range increases, so does the C.S.R which makes the alloy to be more susceptible to cracking. This will continue until the solidus is not depressed further (limit of solid solubility) and if at the same time Tc is lowered further, cracking will decrease due to shortening of the C.S.R.

2.3.4.4.2 Weld Heat Affected Zone Liquation Cracking

HAZ liquation cracking is used to denote the cracking that occurs in the HAZ of a weldment during welding. It is a problem that plagues a large number of highly alloy cast and wrought nickel base superalloys and stainless steels. The alloys are also susceptible to fusion zone cracking, however, fusion zone cracking does not pose as great a challenge as HAZ liquation cracking because it can be effectively minimized by the selection of appropriate filler materials and welding procedures. HAZ liquation cracking is more

difficult to prevent because the factors that contribute to its occurrence in a material are often related to the composition and microstructure of the material, both of which have been optimized to achieve desirable material properties.

The cause of HAZ liquation cracking is generally attributed to a combination of mechanical driving force for cracking; threshold tensile welding stresses, and a crack susceptible microstructure, such as with liquated grain boundaries. The liquation of HAZ grain boundaries during welding causes a solid-solid interfacial bond of the boundaries to be replaced by a weaker solid-liquid bond. Consequently, this reduces the threshold tensile welding stresses that the boundaries can withstand before decohesion occurs. Thus, the inherent resistance of the alloy to HAZ cracking is reduced by grain boundary liquation. HAZ grain boundary liquation can occur either by a non-equilibrium phase transformation below the bulk solidus of an alloy, or by supersolidus melting above the equilibrium solidus of the alloy. The occurrence of non-equilibrium subsolidus melting is particularly more harmful as it widens the temperature range over which liquid film remains on grain boundaries, and thereby increases their susceptibility to cracking [54]. The mechanisms of HAZ liquation in a wide variety of austenitic alloys have been investigated by several researchers [55 – 66] and have been mainly attributed to the following, which are discussed in the next few subsections:

1. Constitutional liquation of second phase particles and the wetting of grain boundaries with liquid produced from the liquation process.
2. Grain boundary segregation of melting point depressants, such as boron, during thermo-mechanical or thermal treatments of an alloy prior to welding.

2.3.4.4.2.1 Theories of Weld Heat Affected Zone Liquation Cracking

2.3.4.4.2.1.1 Constitutional Liquation Theory

The theory of constitutional liquation was first proposed by Pepe and Savage [56] after they observed the liquation of titanium sulphide precipitates in 18 Ni maraging steel. Since then, the concept has been observed by several researchers in different alloy systems, some of which are listed in Table 2-7, and has been used to explain non-equilibrium liquation of various precipitates in the alloys during welding. The theory describes the formation of intergranular liquid films on grain boundaries through a eutectic-type reaction between second phase particles and their surrounding matrix. Under extremely slow (equilibrium) heating rates, second phase particles e.g. MC type carbides, will dissolve in the matrix by a slow diffusion-controlled process. If the heating rates are extremely rapid (non-equilibrium), as observed in the HAZ of most alloys during welding, sufficient time may not be available for the particles to completely dissolve before reaching a temperature at which eutectic reaction occurs between them and their surrounding matrix. Thus, at the elevated temperature, a localized liquid will be formed along the particle – matrix interface. The amount of liquid that forms depends on factors such as the heating rate, size of liquating particles, and their dissolution kinetics at elevated temperatures.

Constitutional liquation was illustrated using a simple binary phase diagram of a hypothetical binary alloy which is shown in Fig. 2-18 [56]. At temperature T_1, the alloy with composition Co consists of α solid solution matrix and high melting point intermetallic particles of AxBy, which are distributed as second phase particles within the matrix. At an infinitely slow heating rate, the solubility of element B in the α matrix

Table 2-7: Constitutional liquation in multicomponent alloys.

Alloy	Liquating Phase
Udimet 700	M_3B_2[55]
Hastelloy X	M_6C[55]
18 Ni Maraging steel	TiS [56]
Inconel 600	Ti (CN), Cr7C3 [57]
Austenitic alloy A286	TiC[58]
Inconel 718	NbC and Laves phases [61]
Incoloy 903	MC carbide and MNP phosphides[62]
Inconel 738	MC-type carbides, γ', M_3B_2, M_2SC[67]
Allvac 718Plus®	MC-type carbides [68]

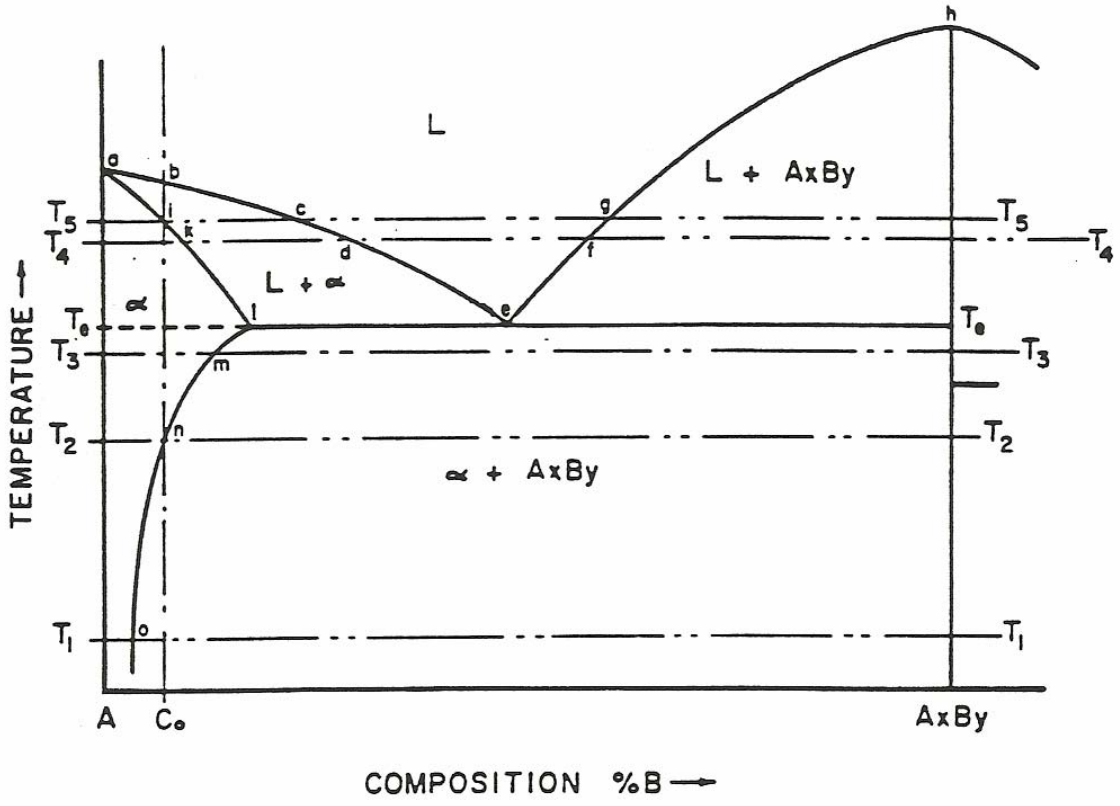

Fig. 2-18: Schematic diagram of a portion of hypothetical phase diagram for an alloy system exhibiting constitutional liquation [56].

increases, resulting in a gradual dissolution of AxBy particles until the last particle dissolves at temperature T_2 and the alloy becomes a homogeneous single solid solution phase. Continued heating at an infinitely slow rate beyond T_2 to just below T_5 would cause no further changes other than normal grain growth and equilibrium grain boundary segregation of impurity solute elements. At T_5, the solidus of the alloy, melting begins and causes the formation of liquid of composition c. The behavior of the alloy under a non-equilibrium rapid heating rate would, however, be different from the one just described above. Assuming that AxBy particles are spherical, Figs. 2-19 a – c show schematically the changes expected in the vicinity of the particles during rapid heating to temperatures of T_3, T_e and T_4, also marked on the phase diagram in Fig. 2 -18. During heating to T_3, AxBy begins to dissolve since it is unstable with respect to α matrix at this temperature. Thus, the AxBy particle would shrink somewhat from its original size (represented by the dashed circle in Fig. 2-19 a) to a smaller size (represented by the solid circle in Fig. 2-19 a). The solute B atoms released from AxBy particles should diffuse into adjacent α matrix. However, as shown in Fig. 2-18, the AxBy phase must be in contact with α phase of composition 'm' for the two phases to coexist. Thus, a concentration gradient is set up in α matrix with a maximum of 'm' at the AxBy interface and a decrease towards the original matrix composition 'o' further away into α phase. The slope of the concentration gradient produced would depend on the following:

1. Heating rate: the faster the heating rate, the steeper whould be the concentration gradient.
2. Solute diffusivity: the faster the diffusivity of solute atoms B, the shallower would be the concentration gradient.

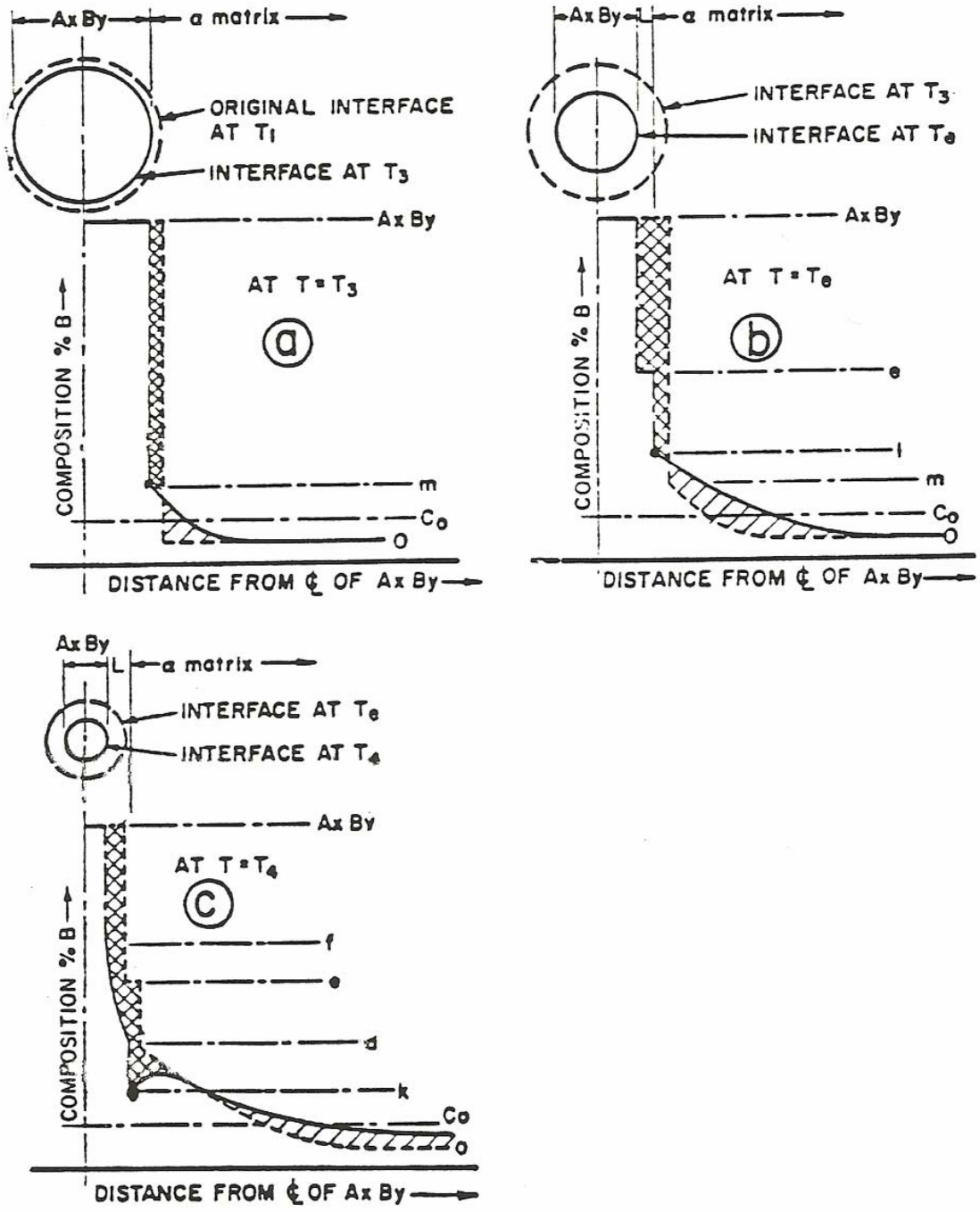

Fig. 2-19: Schematic representation of the concentration gradients at various temperatures during constitutional liquation [56].

3. Accommodation factor: the easier the solute atoms are accommodated within α matrix, the shallower would be the concentration gradient.

Fig. 2-19b shows further changes that would occur during heating from temperature T_3 to T_e, the eutectic temperature. The dashed line represents the solute distribution at temperature T_3, while the solid line represents a modified solute distribution at T_e. During the time interval of heating the alloy from T_3 to T_e, AxBy continues to dissolve. Thus, its particle size would continue to decrease, as shown in Fig. 2-19 b, where the dashed circle represents the particle interface location at T_3 while the solid circle represents the particle interface at T_e. At T_e, the composition corresponding to point 'e' permits the formation of liquid phase at the interface of AxBy particles. Thus, at the instant the temperature of the alloy reaches eutectic temperature Te, the undissolved portion of AxBy particle should be surrounded by a liquid phase of composition 'e', which, in turn, should be surrounded by α matrix. The distribution of solute atom B in the three phases coexisting at Te is shown in Fig. 2-19 b.

Further heating to T_4 would allow additional time for dissolution of AxBy phase. During heating above T_e, the equilibrium solubility of B atoms in the α phase decreases along the solidus line 'akl'. Therefore, as the temperature rises above T_e, the concentrations of the solid solution and liquid phase in contact with one another should correspond to 'k' and 'd', respectively (Fig. 2-18). This readjustment in composition would create an inverted region in the concentration gradient similar from to that shown in Fig. 2-19 c. The excess solute in the α phase would cause the α/liquid interface to move epitaxially into the α matrix until the excess solute is consumed by forming liquid

of composition ‘d’. This results from the fact that a solid metal cannot be superheated above its liquidus temperature by more than an infinitesimal amount.

At T_4, each undissolved AxBy particle would be completely surrounded by liquid phase with variable composition ranging from ‘f’ at AxBy interface to ‘d’ at the interface with α matrix. Hence, localized melting would be possible with rapid heating rates at temperatures below the equilibrium solidus temperature T_5. This phenomenon, which in theory could occur at all temperatures above T_e, is termed constitutional liquation. Evidence of constitutional liquation should be observable whenever an intermetallic compound and the surrounding matrix phase react to form a low melting liquid phase, provided that the heating rate is rapid enough to preclude complete dissolution of the compound prior to reaching the minimum liquidus temperature. However, if the initial composition of the alloy is above the solubility limit ‘l’ (Fig. 2-18), the occurrence of eutectic type melting at Axby/α interface would be independent of heating rate as AxBy would be thermodynamically stable up to the eutectic temperature T_e [69].

Fig. 2-20 illustrates the changes in solute distribution that occur in a specimen exhibiting constitutional liquation when heated rapidly to temperature T_4 and then held isothermally for varying times. During holding, solute atoms ‘B’ would diffuse from liquid into α-matrix resulting in a gradual decrease in the width of the liquid phase. Eventually, nearly complete homogenization would occur, thereby permitting the liquid to solidify completely. After the solidification of the liquid, the composition gradient of B atoms in α-matrix would exhibit a maximum corresponding to composition ‘k’ (the maximum solubility of B atoms in α phase at T_4) at the original centerline of AxBy and decrease towards a composition corresponding to point ‘o’ at the interior of the α-matrix.

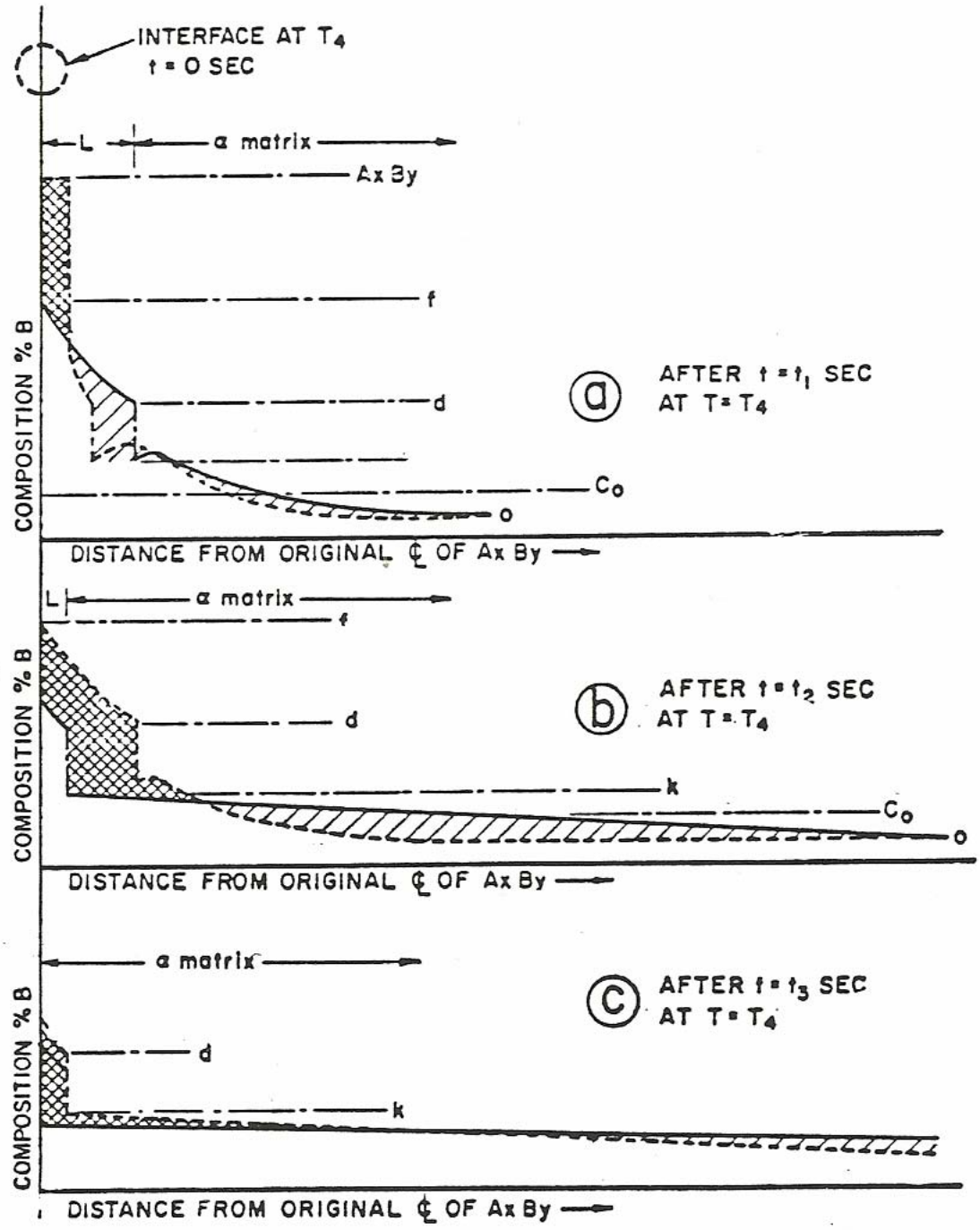

Fig. 2-20: Schematic representation of the effect of holding time on stability of liquid film produced by constitutional liquation [56].

Thus, the liquid films produced by constitutional liquation should experience a gradual modification in composition once the AxBy phase is completely dissolved and should ultimately disappear by solidification if subjected to a sufficiently long isothermal holding at any temperature below the equilibrium solidus.

The occurrence of constitutional liquation in an alloy is significantly influenced by the solid-state dissolution behavior of its second phase precipitates. With interstitial compounds, such as Fe_3C, the ease of dissolution and rapid diffusion of interstitial solute atoms of carbon make constitutional liquation unlikely, except in the case of electric resistance spot welding with extremely rapid heating and cooling rates. This was verified by Aronso [70] who studied constitutional liquation in plain carbon eutectoid steel and concluded that with a heating rate of 625^oC/sec, Fe_3C phase with less than 2 μm in diameter would dissolve completely prior to reaching the eutectic temperature of 1271^oC. On the other hand, less readily dissolvable alloy carbides or intermetallic compounds with substitutional type solute would make constitutional liquation almost unavoidable except for welding conditions with extremely slow heating rates. Some of the alloy systems in which constitutional liquation has been observed and the corresponding liquating phases are shown in Table 2-7.

2.3.4.4.2.1.2 Grain Boundary Segregation Mechanism

Grain boundary liquation can also occur by the segregation of melting point depressants, e.g. boron, phosphorous, sulphur, etc, to grain boundary regions. These elements reduce the melting temperature of the grain boundary regions relative to their surrounding matrix and cause preferential non-equilibrium subsolidus melting of the

boundaries during welding. This could cause HAZ liquation cracking to occur even when constitutional liquation of precipitate particles does not, or cannot occur. The segregation of elements to grain boundaries prior to welding can occur during different thermal processes such as casting, hot deformation and pre-weld heat treatments. It is a diffusion-controlled process and can occur by either equilibrium [71-73] or non-equilibrium mechanisms [74-80].

Equilibrium segregation refers to the movement of misfit impurity atoms from within the grain of a polycrystal to disordered regions such as grain boundaries, precipitates/ matrix interfaces and stacking faults. Under this condition, the interfacial free energy of the system is lowered by an amount E_b, which is the difference between the binding energy of the impurity atoms to the parent lattice compared to their binding to a grain boundary [78]. Hence, the driving force for equilibrium segregation of elements to interfaces in a material is the minimization of the free energy of the interface. Equilibrium segregation is usually restricted to within a few atom layers of grain boundaries. Also, it reduces with a reduction in solute content or an increase in temperature. As temperature is increased, the vibrational amplitude of lattice atoms increases. This reduces the driving force for the impurity or solute atoms to move from the grains to the grain boundaries, and thus, reduce the degree of equilibrium segregation. At lower temperatures, it is difficult for the segregating atom to diffuse to the grain boundaries, despite the fact that the driving force is high. As a consequence, the rate of segregation becomes progressively reduced beyond an initial increase which accompanies the decrease in temperature [64]. Therefore, there is an optimum temperature at which the highest degree of equilibrium segregation occurs.

The occurrence of non-equilibrium segregation to grain boundaries during thermal treatments was first reported by Westbrook, Aust and co-workers [74-77] and by Anthony [80]. It is considered to result from the formation of atom-vacancy complexes within the lattice of a polycrystalline material, and the presence of a gradient in the concentration of the complexes between grain interiors and grain boundaries. If the material is subjected to a thermal cycle where non-equilibrium conditions exist, such as rapid cooling from high temperature, a supersaturation of vacancies will develop within the lattice at lower temperatures, i.e. the grain interiors will retain excessive vacancies at a concentration corresponding to the higher heat treatment temperature. While the grain interior remains supersaturated with vacancies, the grain boundaries will act as efficient sinks for the vacancies. Thus, a concentration gradient is set up, allowing the vacancies to diffuse towards the grain boundaries. Provided a positive attraction (binding energy) occurs between the vacancies and solutes, solute-vacancy complexes will be formed [64]. The complexes within the diffusion range of grain boundaries will migrate to the interface where the vacancies are annihilated while the solutes occupy grain boundary positions. This will lead to a gradual accumulation of the solute atoms (segregant) at, and within, regions of a few nanometers about grain boundary plane. The effective uphill diffusion of solute atoms, producing the solute-rich boundary region, is thermodynamically driven by the decrease in free energy associated with the annihilation of excess vacancies at boundary sinks [64]. Non-equilibrium segregation is reversible, and its extent is dependent on the binding energy of solute atoms to vacancies. Other important factors are heat treatment temperatures, cooling rates and bulk concentration of the solute / impurity atoms in a material. Apart from cooling from higher temperatures,

other non-equilibrium processes, such as neutron irradiation and deformation, can also induce non-equilibrium segregation [78]. However, the principal source of segregation in welded components results from their pre-weld heat treatments.

Previous investigations have been carried out by some researchers on the contributions of grain boundary segregation mechanisms to HAZ liquation cracking of Ni-Fe based superalloy 718 and these are summarized in section 2.4 of this thesis.

2.3.4.4.3 Post-Weld Heat Treatment Cracking in Superalloys

Post weld heat treatment cracking, also commonly referred to as strain age or reheat cracking, often occurs during post weld heat treatment of age hardenable nickel base alloys. The PWHT for the alloys usually consist of a solution anneal followed by a period of aging at about 700 – 850^{o}C. The purpose is to relieve welding residual stresses and develop optimum microstructure and, hence, mechanical properties in weldments. However, cracking may occur during the heat treatments. The cracks are usually intergranular in nature, and range in size from microscopic to a few centimeters in length. They usually initiate in the HAZ, and may propagate into regions that are unaffected by welding heat in the base metal. It is widely believed that post-weld heat treatment cracking occurs from the cumulative effects of residual welding and aging contraction stresses acting on the HAZ which has been embrittled by various metallurgical reactions. The development of post-weld heat treatment cracking in the HAZ of welds, and the contributing factors are discussed in the next sections.

2.3.4.4.3.1 Development of Post-Weld Heat Treatment Cracking in Superalloys

Several researchers [81 – 88] have investigated the causes of post-weld heat treatment cracking in γ′ age hardenable superalloys, especially Rene 41 and Waspaloy. The common theory proposed by the researchers was that post-weld heat treatment cracking was the result of a combination of residual welding and aging contraction stresses acting upon the HAZ during post-weld heat treatment and after it has been embrittled by metallurgical reactions which take place during welding. A schematic of this development is shown in Fig. 2-21 [30]. During welding, the peak temperatures reached by the weld and HAZs alter their microstructure and result in high residual stresses being retained after the weld has cooled and solidified. To restore the properties of the welded alloy, post weld heat treatments comprising of high temperature solution anneal, followed by aging are carried out. However, on heating the alloy to solution treatment temperature, it passes through γ′ precipitation temperature range, T_1 to T_2, as shown in Fig. 2-21. Thus, two processes occur simultaneously for an alloy with very fast γ′ precipitation kinetics. The residual welding stresses tend to be relaxed while the alloy also undergoes a rapid stiffening (loss in ductility) of its grain interior due to γ′ precipitation. Also, since the lattice parameter of γ′ is less than that of γ matrix, the precipitation of a significant volume fraction of γ′ during aging may result in shrinkage contraction of the alloy. In restrained weldments, or welds made on thicker sections, such contraction could lead to the development of high stresses that could further aggravate the stress condition of the alloy and result in the initiation or propagation of cracks. The various factors which affect post-weld heat treatment cracking susceptibility of alloys are summarized next.

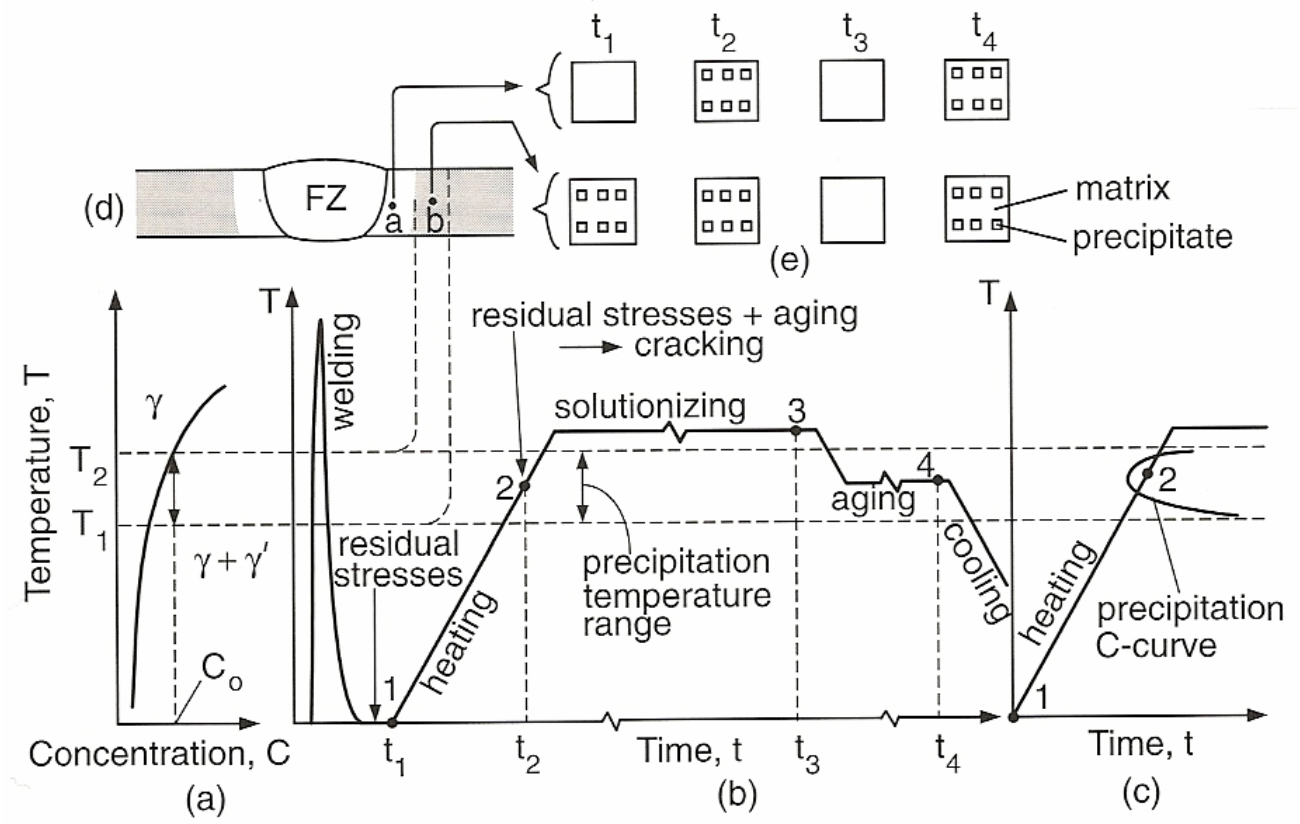

Fig. 2-21: Post weld heat treatment cracking: a) phase diagram, b) thermal cycles during welding and heat treating, c) precipitation C curve, d) weld cross-section, e) changes in microstructure [30].

2.3.4.4.3.2 Factors Affecting Post-Weld Heat Treatment Cracking in Superalloys

1. Al + Ti Composition:

Fig. 2-22 [89] shows the effects of Al and Ti content on cracking (both welding and post-weld heat treatment cracking) of Ni-base alloys. As shown in the figure, alloys above the dashed line have high Al + Ti concentration, and are difficult to weld because of their high susceptibility to cracking during welding and post-weld heat treatment. On the other hand, alloys below the dashed line have low content of Al and Ti, and are readily weldable. Alloys like Rene41 and Waspaloy are on the borderline and are relatively weldable with some difficulty but they crack during post-weld heat treatment. The variation in cracking with Al + Ti content is attributed to the fact that these two elements are major γ′ forming elements. Thus, the rate of precipitation, and volume fraction of γ′ increase with an increase in Al + Ti concentration. Consequently, the alloy will age harden rapidly with the attendant rapid stiffening of its matrix and formation of aging contraction stresses, which could promote cracking of weak HAZ grain boundaries. The addition of niobium as the primary strengthening element, such as in 718, promotes the formation of γ′′ precipitates instead of γ′. The γ′′ has a sluggish aging response, and as such, alloys that are predominantly strengthened by it are generally more resistant to post-weld heat treatment cracking.

2. Prior Grain Boundary Liquation:

Post-weld heat treatment cracks preferentially initiate on HAZ grain boundaries which have been embrittled/ weakened by prior liquation reactions that had occurred on the grain boundaries during welding. Thus, by controlling the metallurgical reactions, e.g. grain boundary liquation, which embrittle the grain boundaries, the susceptibility of an

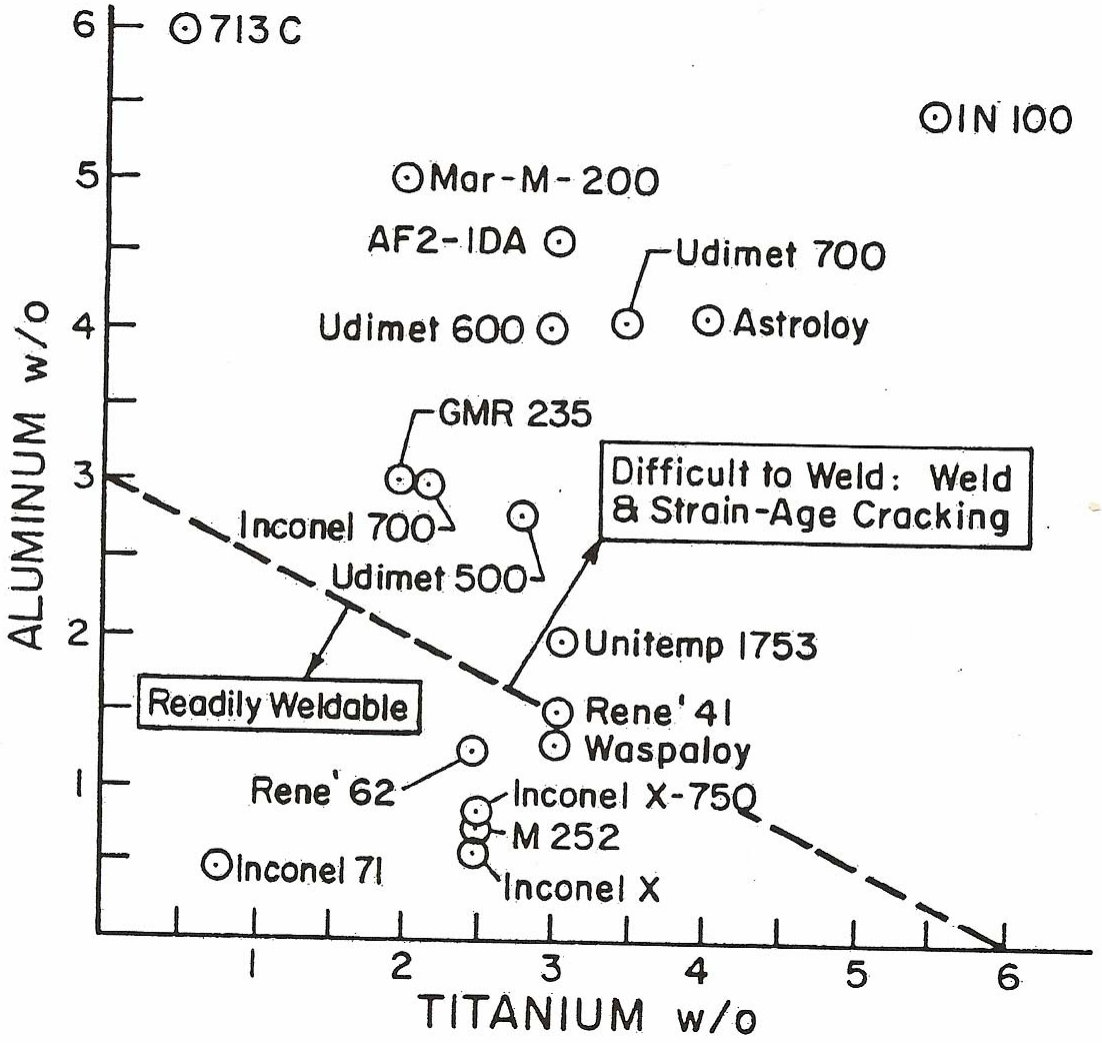

Fig. 2-22: Separation between γ′ strengthened alloys that are difficult to weld and those readily weldable [89].

alloy to post-weld heat treatment cracking can be significantly reduced.

3. Grain Size:

It has been reported [90 – 92] that fine-grained alloys are more resistant to post-weld heat treatment cracking than those having relatively coarse grains. This may be due to a relative ease of stress relaxation by grain boundary sliding in fine-grained alloys. Also, the linking up of voids formed at individual grain boundary facets can be slower in fine-grained materials due to the presence of a greater number of grain boundary triple points.

4. Pre-Weld Heat Treatments:

The condition of an alloy prior to welding influences its susceptibility to cracking during welding and post-weld heat treatment. It has been reported [88] that superior resistance to post-weld heat treatment cracking was observed in Rene 41 by slow cooling from pre-weld solution annealing temperature. The heat treatment resulted in the formation of coarse, overaged γ', which softened the alloy. Sidhu et al [93] studied the post-weld heat treatment cracking of autogenous gas tungsten arc welded Inconel 738LC superalloy, which was pre-weld heat treated in two different heat treated conditions. The first heat treatment, designated as SHT, consisted of annealing at 1120^{o}C for 2 hrs in vacuum followed by argon quenching, while the second heat treatment, designated as UMT, consisted of solution annealing at 1120^{o}C for 2 hrs in vacuum followed by argon quenching and subsequent aging at 845^{o}C for 24 hrs in vacuum. Compared to SHT, UMT resulted in the formation of coarse, overaged γ', which softened the alloy. After PWHT, UMT samples had ≈ 43% less cracking than that observed in SHT. Thus, as observed in Rene 41 [88], 738 was more resistant to post-weld heat treatment cracking in an overaged

condition. This is attributed to the fact that the overaged base metal remains soft and ductile while the HAZ becomes comparatively stronger and less ductile, owing to aging during post-weld heat treatment. Thus, stress relaxation could then be transferred to the weaker, more ductile and voluminous base metal than the HAZ, which has relatively little capacity to accommodate strain.

5. Post Weld Heat Treatment Cycle:

The general experience is that cracking will be severe if components are aged directly following welding [94]. This is because the aging temperature may be too low to effect sufficient stress relief before a considerable hardening of the matrix. Therefore, normal post-weld heat treatments consist of solution annealing before aging. Rapid heating to the post weld solution anneal temperature has been reported to reduce the occurrence of post-weld heat treatment cracking in most heats of Rene 41 [95]. It is suggested that rapid heating allows sufficient stress to be relaxed before the grain boundaries are embrittled by aging reactions. Jordan and Richards [96] found that rapid heating rates could be used to avoid post-weld heat treatment cracking in Ni-base superalloy with an Al + Ti content of about 4 wt%. However, the technique was not successful with an alloy of significantly higher hardener content, Al + Ti ≈ 9 wt%. It can be difficult to achieve a uniform heating rate in the various sections of a massive welded assembly. Therefore, employing rapid heating rates in such cases may induce a high level of thermal stresses, which may be detrimental. A solution proposed [97] for this difficulty is a stepped heating technique in which the component is slowly heated to about 500^{o}C, soaked at this temperature to reduce thermal gradients in the component, and then rapidly

heated through the mid-range ductility dip (precipitation range of γ′) to the solution treatment temperature.

6. Heat Treating Environment:

Post-weld heat treatment cracking can be significantly reduced by carrying out post-weld heat treatments in vacuum or inert atmosphere. The heat treating atmosphere was found by Thompson et al [88] to be effective since little or no oxygen would be available to embrittled grain boundaries during post-weld heat treatment. The detrimental effects of oxygen were found to be active even at low concentration of 2 vol. %. Post-weld heat treatment cracking was eliminated in high purity dry argon, argon containing 0.5 vol. % oxygen, and vacuum atmospheres. It was suggested that the detrimental effects of oxygen-rich atmospheres could be due to the rapid diffusion of oxygen along grain boundaries, and the consequent formation of oxides, which are not able to resist plastic deformation.

2.4 Previous Investigations on the Weldability of 718-Type Alloy

A great number of investigations have been carried out over the past 40 years on the weldability of alloy 718. The wrought form of the alloy is generally considered to be weldable, although it suffers from HAZ cracking during welding. Earlier studies [98 – 101] attributed the HAZ cracking to constitutional liquation of MC-type carbides which occurs during welding. In addition to the cracking caused by constitutional liquation of carbide particles, Thompson et al [102] suggested that the segregation of sulphur to grain boundaries during pre-weld heat treatment also contributed to the liquation and cracking

of the boundaries. In a later study, Kelly [103] reported boron to be the most detrimental tramp element that contributed to the liquation cracking of 718.

By secondary ion mass spectroscopy, Huang et al [63, 64] observed the grain boundary segregation of boron in cast 718. The segregation occurred by equilibrium and non-equilibrium mechanisms during pre-weld solution heat treatments of the alloy. The amount of equilibrium segregation decreased with an increase in solution treatment temperature, while it was unaffected by variation in cooling rates. Non-equilibrium segregation, on the other hand, increased with an increase in temperature, and a decrease in cooling rate. A very fast cooling rate, which was obtained by water quenching after solution treatment, inhibited non-equilibrium segregation of boron as it did not allow sufficient time for diffusion of boron–vacancy complexes to grain boundaries. Non-equilibrium segregation was enhanced by cooling at an intermediate rate, such as with air cooling. In order to study the effect of the boron segregation on weld HAZ cracking of cast 718, Huang et al [63, 64] carried out bead on plate electron beam welding on the alloy after it was solution heat treated at various temperatures in the range of 1037^{o}C to 1163^{o}C, and air cooled. It was reported that the total crack length (TCL) in the weld HAZ of the alloy varied in a similar pattern as the variation of boron segregation with pre-weld heat treatment temperature after air cooling. As boron segregation increased so did the weld cracking. Chen et al [65, 104] further investigated the effect of boron segregation on the cracking behavior of wrought 718. As reported for cast 718 by Huang et al [63, 64], they also found that the weldability of wrought 718 was closely related to the degree of grain boundary segregation of boron. While the extent of grain boundary segregation of boron and weld cracking in 718 was influenced by pre-weld heat treatment temperature

and cooling rates, Guo et al [105, 106] investigated other possible influence that may arise from the nature of grain boundaries that are present in the alloy. In their work, alloy 718 was pre-weld solution heat treated at 1050^{o}C followed by water quenching. The heat treated alloy was then subjected to simulated weld HAZ cycles using a Gleeble 1500 machine. SEM examination of the thermally simulated HAZs revealed that grain boundary liquation was heterogeneous in nature, i.e. while some grain boundaries liquated, others which witnessed same temperature did not. Further analyses using OIM (orientation image microscopy) and SIMS revealed that the grain boundaries that liquated were mostly non-special (random) boundaries where boron preferentially segregated. Thus, the overall cracking of the alloy is dependent on the nature of its grain boundaries.

In a fairly recent work, Qian and Lippold [107] reported that the presence of δ phase on the grain boundaries of 718 could assist grain boundary liquation and thus, increase the susceptibility of the alloy to liquation cracking. Wrought alloy 718 was subjected to long-term isothermal solution heat treatments at 954^{o}C/ 40hrs and 954^{o}C/ 100 hrs, respectively. The heat treatments resulted in an extensive intergranular and intragranular precipitation of δ phase. Thereafter, the heat treated alloy, along with its as-received form which contained a considerably smaller volume fraction of δ phase, were subjected to Gleeble hot ductility testing in which susceptibility to HAZ liquation cracking was determined by observing the liquation temperature range (LTR) of the alloy (as LTR increases, HAZ liquation cracking increases). The LTR of the alloy increased from as-received, to 954^{o}C/ 40hrs, and 954^{o}C/ 100 hrs. This was attributed to an increase in the volume fraction of δ-phase as a function of holding time at 954^{o}C. It was proposed that the dissolution of δ-phase which occurred during welding of 718 enriched its

surrounding nickel γ-matrix on grain boundary region with niobium atoms. This extended the LTR of the alloy by depressing the melting point of the grain boundaries and forming a low temperature eutectic on them. It should be noted that this theory, as proposed by Qian and Lippold [107], is still questionable as it was not sufficiently proven that the eutectic products observed on the grain boundaries resulted from δ-phase dissolution-assisted liquation, and not from constitutional liquation of second phase particles, e.g. carbides, or liquation induced by grain boundary segregation of minor elements such as boron.

Vishwakarma [108] studied the weldability of 718Plus and reported that the alloy is susceptible to HAZ liquation cracking during welding. The liquation cracking was attributed to the constitutional liquation of MC-type carbides, and grain boundary segregation of minor elements. Weld cracking measurements and result of hot ductility tests revealed that cracking in 718Plus was comparable to that of 718. However, cracking was more pronounced in Waspaloy than in 718Plus.

2.5 Scope and Nature of the Present Study

As discussed earlier, to produce alloy 718Plus, major compositional modifications were made to its base alloy 718. The modifications changed the main strengthening phase of the alloy from a less stable γ″ to a more stable γ′ phase. This resulted in significant improvements in the microstructural stability and mechanical strength of 718Plus at higher temperatures. Although, 718Plus can withstand higher service temperatures, pioneering investigation [108] on its weldability showed that it is susceptible to HAZ liquation cracking during welding. The cracking was attributed to the constitutional

liquation of MC-type carbide and segregation- induced grain boundary liquation. No detailed study exists in open literature on the cracking behavior of the alloy during post weld heat treatment, despite the fact that γ′ - strengthened Ni base superalloys have been found to be prone to cracking during post-weld heat treatment. Adequate comprehensions of the cracking behavior of the alloy during welding and post-weld heat treatment, and how the cracking is affected by pre-weld and post-weld heat treatments, are essential for its successful commercial application in critical aero-engine components. Therefore, the current investigation was undertaken to achieve the following objectives:

1. To study and gain a comprehensive understanding of the susceptibility of Allvac 718Plus to HAZ cracking during low and high heat input high energy beam welding process.
2. To investigate the effects of pre-weld heat treatments on weld cracking. This is aimed at finding an adequate heat treatment schedule that could reduce or eliminate cracking during welding. Specifically, this study investigates the effects of various pre-weld heat treatments on segregation of boron to grain boundaries, and variation in grain size. Both of these are known to significantly affect the weld cracking characteristics of Ni-base superalloys.
3. To study the PWHT microstructure, cracking behavior, and possible cause(s) of PWHT cracking in Allvac 718Plus.

It is believed that fundamental information from this work will aid the development of welding repair procedures that could eliminate or minimize weld and PWHT cracking of 718Plus weldments. In order to achieve above-stated research objectives, the following approaches, shown in the flow charts (Figs. 2-23 a-c) below, were undertaken:

a)

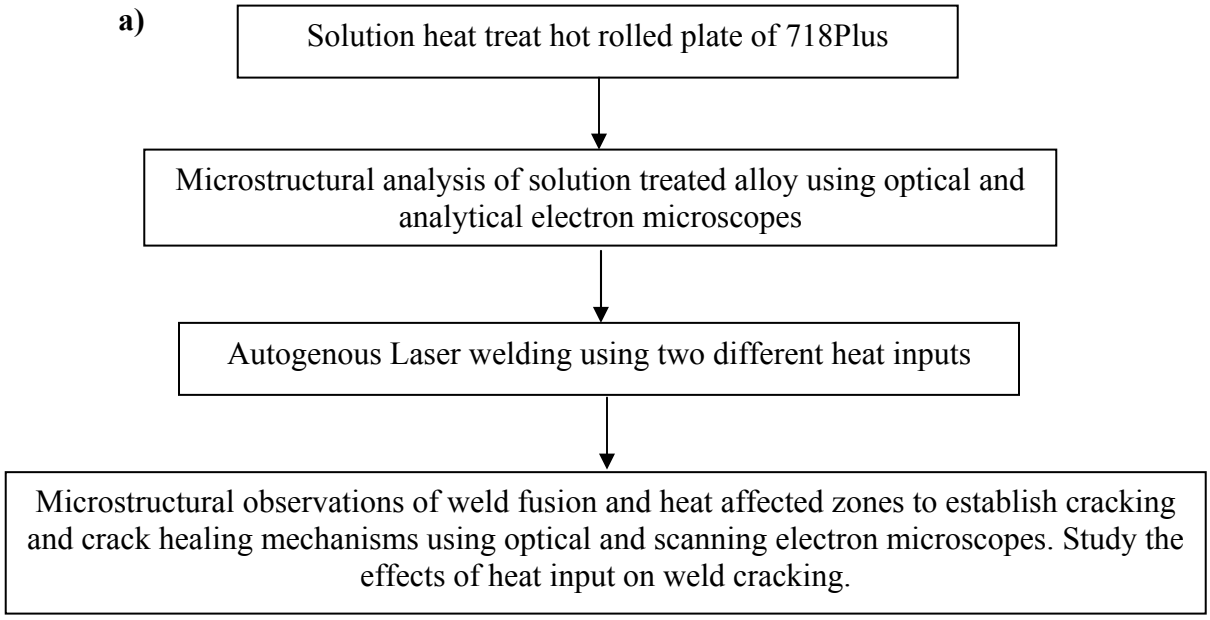
Solution heat treat hot rolled plate of 718Plus
Microstructural analysis of solution treated alloy using optical and analytical electron microscopes
Autogenous Laser welding using two different heat inputs
Microstructural observations of weld fusion and heat affected zones to establish cracking and crack healing mechanisms using optical and scanning electron microscopes. Study the effects of heat input on weld cracking.

b)

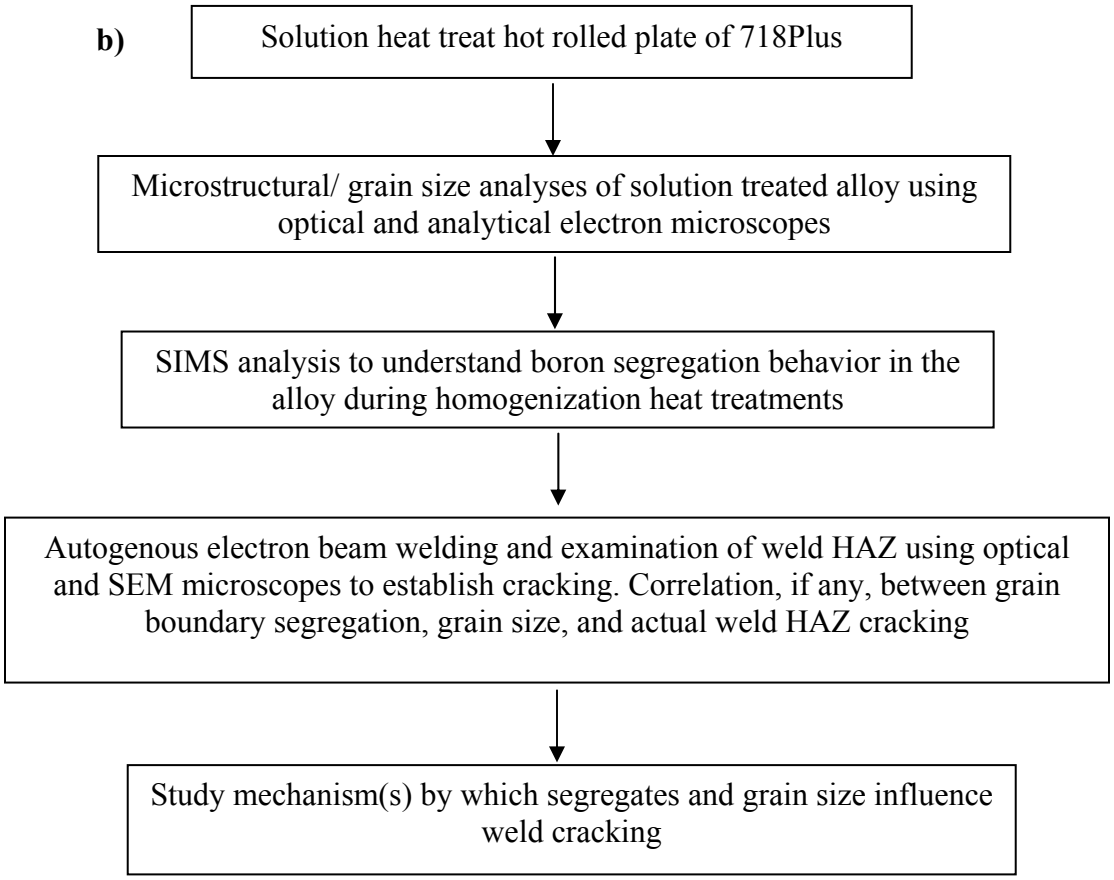
Solution heat treat hot rolled plate of 718Plus
Microstructural/ grain size analyses of solution treated alloy using optical and analytical electron microscopes
SIMS analysis to understand boron segregation behavior in the alloy during homogenization heat treatments
Autogenous electron beam welding and examination of weld HAZ using optical and SEM microscopes to establish cracking. Correlation, if any, between grain boundary segregation, grain size, and actual weld HAZ cracking
Study mechanism(s) by which segregates and grain size influence weld cracking

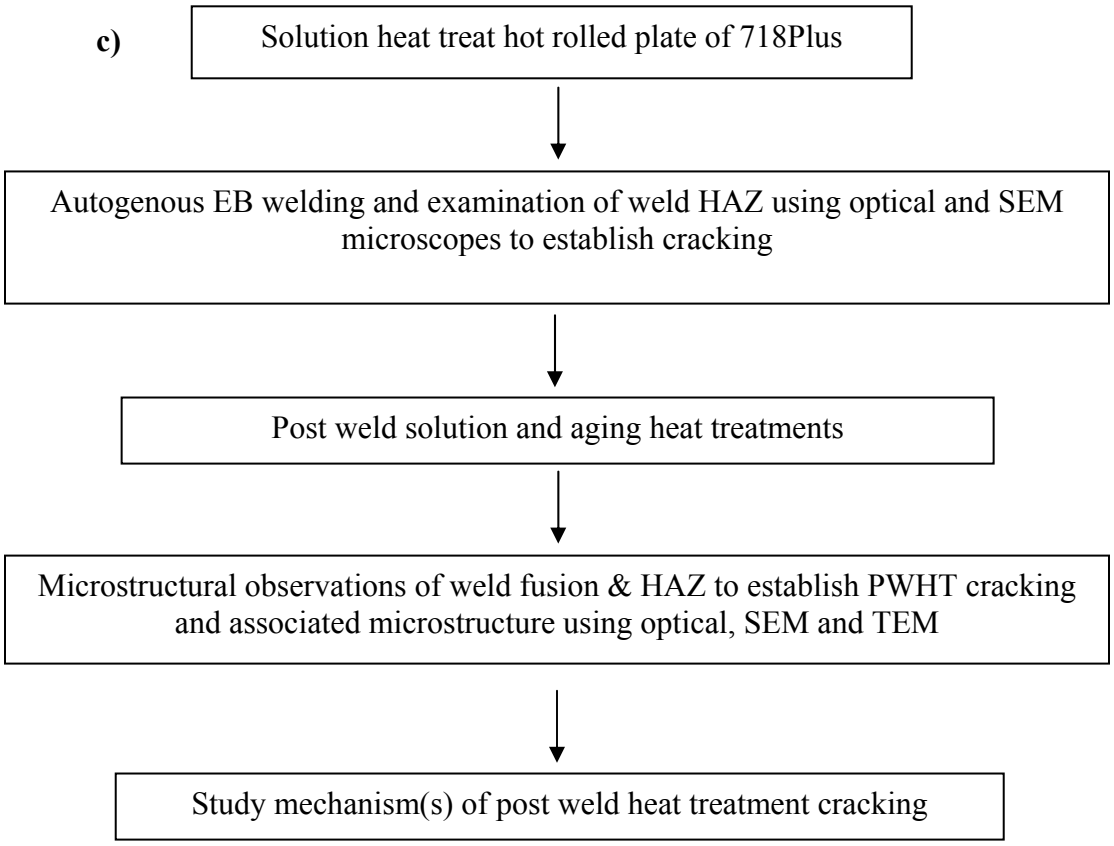

Fig. 2-23: Flow chart of research approach on: a) HAZ cracking during low and high heat input laser welding, b) influence of pre-weld heat treatments on weld HAZ cracking, c) PWHT microstructure and cracking in 718Plus.

Chapter 3

Experimental Procedures

3.1 Materials and Processing

3.1.1 Materials and Pre-weld Heat Treatments

The Allvac 718Plus superalloy that was used in this study was supplied by ATI Allvac in the form of 305 x 127 x 16 mm hot rolled plate. The alloy contained about 30 ppm of boron. The rest of its elemental composition is given in Table 3-1. Rectangular sections measuring 12 x 12 x 100 mm and 3 x 3 x 2 mm were cut normal to the rolling direction of the plate, and then solution heat treated for 1 hour in an argon atmosphere in a furnace. Various pre-weld solution heat treatments were selected for different part of the investigation as summarized in Table 3-2. The heat treatment temperatures ranged from 950^{o}C to 1150^{o}C, while the cooling rates employed varied from iced-water quenching (≈ 500^{o}C/s), air cooling (≈ 25^{o}C/s), to furnace cooling (≈ 0.25^{o}C/s).

3.1.2 Welding

In order to investigate the effect of weld heat input on cracking, pre-weld solution heat treated (1025^{o}C/ 1hr + water cool) rectangular plates with 12 x 12 x 100 mm dimension were autogenously welded using laser lamp power of 2.5 KW and 1.5 KW, and at welding speed of 110 mm/min and 20 mm/min, respectively. These welding parameters correspond to heat inputs of 137 J/mm and 472 J/mm, and are henceforth referred to as low and high heat input, respectively. Also, to investigate the effects of various pre-weld heat treatments on HAZ cracking of 718Plus during welding,

Table 3-1: Bulk chemical composition (wt %) of 718Plus.

Element	**Wt %**
Ni	Bal
Cr	17.92
Fe	9.33
Co	9.00
Nb	5.51
Mo	2.68
Al	1.50
W	1.04
Ti	0.74
Mn	0.03
C	0.022
Si	0.02
V	0.02
P	0.006
B	0.003
Mg	0.0008
S	0.0003

Table 3-2: Heat Treatment Procedures

Pre-weld solution heat treatment:

1025°C/ 1hr + water cool

Pre-weld solution heat treatments:

Temperature (°C)	950 °C/ 1hr	1050 °C/ 1hr	1150 °C/ 1hr
Cooling method	ID-WQ* AC+ FC#	ID-WQ AC FC	ID-WQ AC FC

*ID-WQ: Iced water quench at ≈ 500°C/s
+AC: Air cooled at ≈ 25°C/s
#FC: Furnace cooled ≈ 0.25°C/s

12 x 12 x 100 mm heat treated specimens were welded autogenously along the 100 mm length using a focused electron beam at 44 kV voltage, 79 mA beam current and 152 cm/min welding speed. A switch was made from Laser beam to electron beam welding technique due to unavailability of Laser beam welding equipment.

3.1.3 Post-Weld Heat Treatment (PWHT)

To study the PWHT microstructure, cracking behavior, and the cause(s) of cracking in 718Plus during post-weld heat treatments, electron beam welded coupons were solution heat treated at 950 ^{o}C / 1hr + AC and aged at 788^{o}C/ 8 hrs + furnace cool to 654^{o}C/ 8 hrs + air cool. The aging heat treatment employed was the commercial treatment recommended by Allvac [7]. The post-weld heat treatments were carried out in an argon-filled furnace, and on samples which were solution heat treated at 950^{o}C/ 1hr + AC and 1050^{o}C/ 1hr + AC, respectively, before welding.

3.2 Optical and Scanning Electron Microscopy

The microstructural conditions prior to high power beam welding were examined by optical microscopy, scanning electron microscopy (SEM) and X-ray microanalysis (energy dispersive spectroscopy - EDS). Mean grain size under all pre-weld conditions were determined on an inverted-reflected light microscope equipped with quantitative image analysis software, Clemex Vision 3.0 software. Also, the microstructure of the pre-weld heat treated samples were examined using a JEOL 5900 scanning electron microscope (SEM) operated in both secondary and backscattered electron emission modes. Semi-quantitative chemical composition analyses were carried out using an

Oxford-Inca ultra thin window energy dispersive spectrometer (EDS) system which was attached to the SEM.

Transverse sections of bead on plate welds and post-weld heat treated samples were sectioned by electro-discharge machining and prepared by standard metallographic polishing technique for microstructural study. The polished samples were examined under optical microscope to observe the morphology of cracking (if any) in the welds. To further reveal the microstructure of the base metal, fusion and heat affected zones of the welds, the polished samples were etched electrolytically at 6V for 5 seconds in a solution of 10% oxalic acid. The microstructures were examined using an optical microscope and a JEOL 5900 scanning electron microscope (SEM) in both secondary and backscattered electron (BSE) imaging modes. The susceptibility of 718Plus to HAZ cracking during welding and post-weld heat treatments was evaluated by measuring total length of cracks (TCL) observed in 8 sections of each weld.

3.3 Secondary Ion Mass Spectroscopy

The SIMS technique was used to analyze grain boundary distribution of boron in this study. In the SIMS, a solid sample is bombarded with primary ions of few keV energy. This results in the sputtering of atomic species from the surface of the sample. Fractions of the species are emitted as negative, neutral or positive secondary ions and their mass are analyzed by a mass spectrometer to determine the elemental, molecular or isotopic composition of the surface. Due to the extremely high signal/background ratio of the mass spectrometer, SIMS can detect trace amounts of elements on a surface. It provides ion images with spatial resolution of a few μm and elemental resolution to a few

ppm. The primary ion beam species used in SIMS include Cs^+, O_2^+, O^-, Ar^+, Ga^+ and Xe^+. Electronegative elements such as O, S, and P are most sensitive to Cs^+ beam, while $O_2^+$is used for most other elements.

In preparation for SIMS analysis in this study, 3 x 3 x 2 mm pre-weld heat treated coupons were mounted in an epoxy base resin and polished to 1 μm finish using standard metallographic techniques. Thereafter, they were electro-etched in 10% oxalic acid at 6V for 5 seconds. This revealed the grain boundaries, which were the areas of interest for SIMS analyses. A Vickers micro-hardness indenter was used to mark the grain boundaries, and the coupons were repolished to remove the etched surface layer while leaving the indentations. Finally, the coupons were removed from the epoxy base resin in which they were mounted. The coupons were then examined for grain boundary segregation of boron using a Cameca IMS-7f magnetic sector secondary ion mass spectrometer. The equipment was operated in a scanning microprobe mode. A primary ion beam of O_2^+ with impact energy of 10 kV and 180 pA beam current was rastered over an approximate surface are of 150 μm x 150 μm of the coupon. Mass resolved images of boron were obtained by imaging positive secondary ions of $^{11}B^+$.

3.4 Transmission Electron Microscopy

Analytical electron microscopy analyses were carried out on thin foils from the base, fusion, and heat affected zones of as-welded and post-weld heat treated samples, using a field emission gun JEOL 2100F scanning transmission electron microscope equipped with an Oxford ultra-thin window energy dispersive spectrometer, electron energy loss spectrometer and Gatan imaging filter system. The TEM was used to perform

selected area diffraction analyses, and X-ray microanalyses on the constituents present in the thin foils. To produce the thin foils, 3 mm diameter rods were machined by electro-discharge machining from the areas of interest. Disks of 150 – 200 μm thickness were sectioned from the rods and mechanically polished to about 70 μm. Thereafter, electron-transparent foils were produced by polishing the foils in a twin-jet stream of 10% H_2SO_4 solution at -20 to -40^oC using a current of 1.8 – 3.5 A. Electro-polishing produced a very thin foil with perforation suitable for TEM examination. However, when this was not achieved, the foils were further polished by ion milling for about 15 – 120 minutes in a Gatan precision ion polishing system (PIPS) equipped with liquid N_2 cooled stage. A voltage of 4.5 KeV (Ar+) was used in a vacuum atmosphere of less than 1 x 10^{-5} torr. The incident angle of the ion gun was kept between 5^o-8^o.

Selected area diffraction pattern analysis was used to identify the crystal structure of various phases present in the areas of interest on the thin foils. The lattice parameters of the phases were accordingly determined from the reflections obtained from the selected area diffraction patterns (SADP). Camera length calibration was carried out using ring patterns obtained from thin films of evaporated high purity aluminum placed on a copper grid.

Semi-quantitative chemical microanalyses were performed with the ultra-thin window Oxford EDS equipped with Genesis thin-film analytical software. The program uses Kramer's law for background modeling but does not perform any deconvolution routine for assessment of any relative contribution of elements to overlapped peaks. Nevertheless, X-ray acquisition was mostly from very thin areas and also from precipitates that were not aligned along strongly diffracting orientations. Raw X-ray data

were converted to weight percentages using theoretical Cliff-Lorimer independent sensitivity factor k_{AB}, which is given by:

$$k_{AB} = (C_A/C_B) \times I_B/I_A \qquad (3.1)$$

Where C_A and C_B are the weight percents of A and B respectively and I_A and I_B are the characteristic X-ray intensities.

Due to the limitation of the EDS system in reliably quantifying light elements, the EDS analyses carried out in this work are semi-quantitative in nature. The accuracy is around +/- 0.01 depending on the atomic number and concentration of element present.

Chapter 4

Results and Discussion

4.1 Effect of Weld Heat Input on the Microstructure and Heat Affected Zone Cracking of 718Plus

4.1.1 Introduction

The present investigation was undertaken to study and understand the cracking behavior of Allvac 718Plus during low and high heat input high power beam welding process. Prior to welding, the as-received alloy was solution heat treated at 1025^{o}C/1 hr and water cooled. This heat treatment was above the solvus temperature of delta (δ) phase in the alloy [25] and it was carried out to dissolve the δ phase and homogenize the alloy. After the solution heat treatment, the alloy was autogenously welded using CO_2 laser lamp power with heat inputs of 137 J/mm and 472 J/mm, respectively. The microstructures and occurrence of HAZ cracking developed during the weld fabrication are reported and discussed here.

4.1.2 Microstructure of Pre-weld Solution Heat Treated Alloy

Optical and SEM micrographs of pre-weld solution heat-treated 718Plus alloy are shown in Figs. 4-1 a and b, respectively. The alloy had an average grain size of 94 ± 7 μm (ASTM No. 3.5) and contained dispersed blocky shaped particles in intergranular and intragranular regions of γ solid solution matrix. SEM/EDS spectra from the particles, shown in Figs. 4-2 a and b, indicated that apart from metallic elements, some of the particles had C and B in them, while others contained C and N. Due to the limitation of

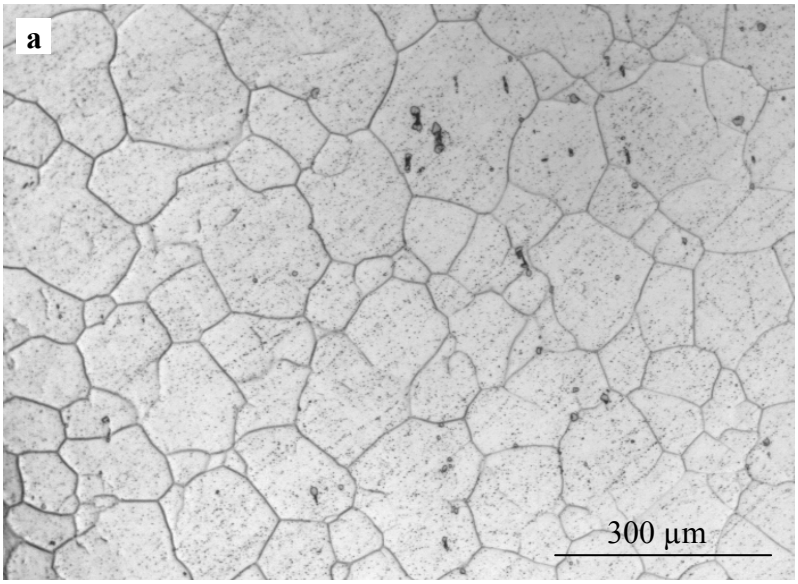

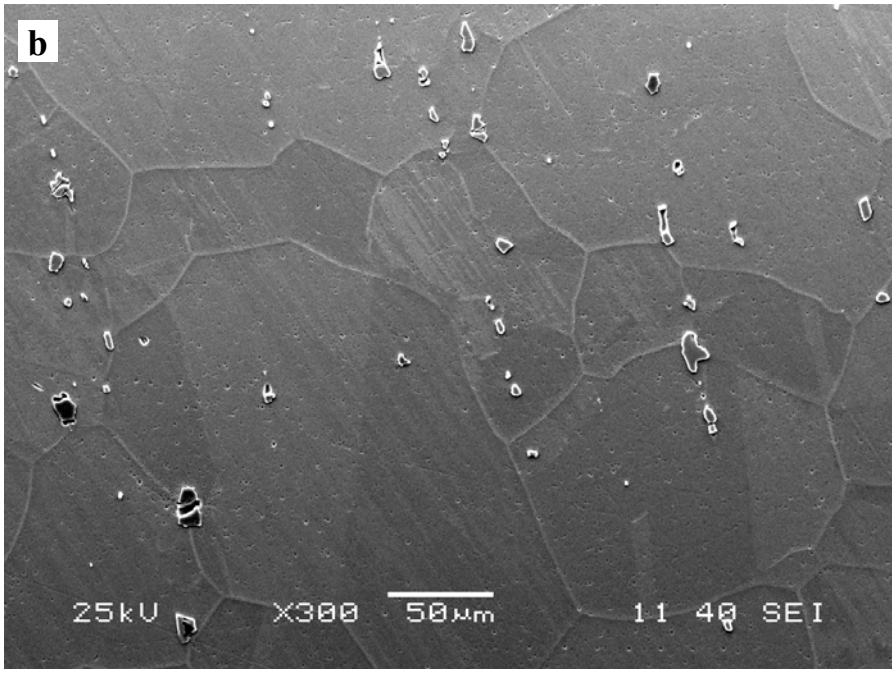

Fig. 4-1: a) Optical and b) SEM microstructure of solution heat treated (1025^{o}C/1 hr + water cool) 718Plus superalloy showing intergranular and intragranular particles within γ matrix.

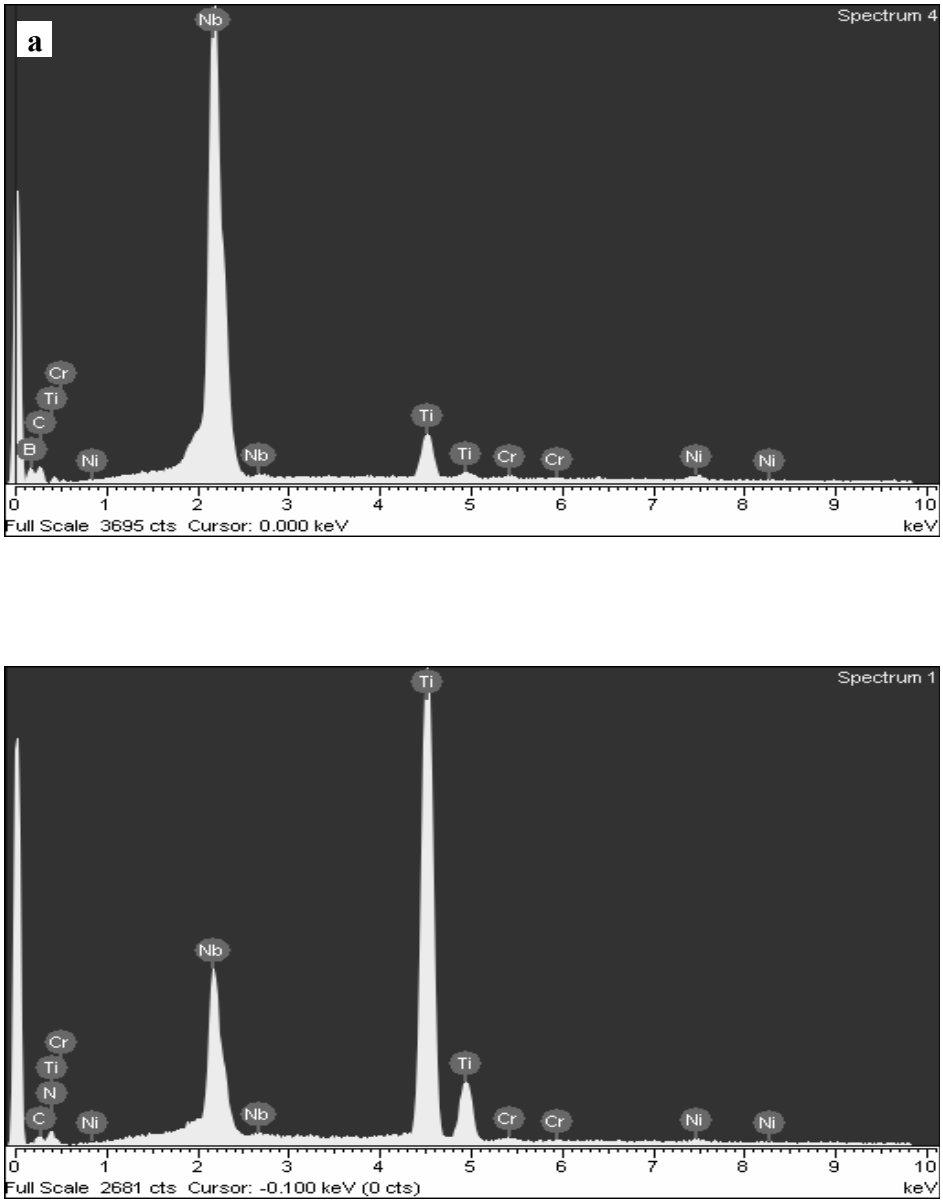

Fig. 4-2: SEM/EDS spectrum from (a) Nb, Ti-rich carboboride, (b) Ti, Nb-rich carbonitride in 718Plus solution heat treated at 1025^{o}C/1h + water cool.

the EDS system in reliably quantifying light elements, C, B, and N were not quantified. However, the SEM/EDS analyses of the rest of the elements in the particles, shown in Table 4-1, indicated them to be Nb, Ti-rich carboborides and Ti, Nb-rich carbonitrides, respectively. Owing to the occasionally large average size (approximately 12 μm) of the carbide insolubles, and their presence with a similar morphology in as-cast form of 718Plus [25], it is reasonable to assume that the carbides observed in the microstructure of solution treated samples are primary solidification constituents of the alloy. The critical phase transformation temperatures of 718Plus have been determined by other researchers [25] through thermodynamic modeling, differential thermal analysis (DTA), and metallography, and are given in Table 4-2. It is seen from Table 4-2 that MC-type carbides formed above the solidus temperature of 718Plus during ingot solidification. Further SEM microstructural examination did not reveal the presence of any other microconstituent in the γ matrix of the solution treated alloy. This was primarily due to the fact that the solution heat treatment temperature was above the formation temperature of most of the second phase particles found in 718Plus (Table 4-2). Moreover, examination of the as-received alloy revealed the absence of Laves phase, which normally forms as a solidification constituent during ingot solidification. Although it has been claimed [25] that in comparison to 718, 718Plus has a lower volume fraction of Laves phase due to its significantly reduced Fe concentration, a complete absence of Laves phase in the as-received wrought form suggests that this solidification constituent was completely dissolved during hot working of cast billets.

Table 4-1: Semi-quantitative SEM/EDS Analysis (at. %), excluding B, C and N, of particles observed in solution heat treated (1025^{o}C/1 hr) 718Plus.

Element (at. %)	Nb	Ti	Cr	Ni
Nb, Ti (C,B)	79.0	17.1	1.1	2.8
Ti, Nb (C,N)	14.5	84.0	0.8	0.7

Table 4-2: Phase transformation temperatures in 718Plus [25].

	Transformation Temperature (^{o}C)		
Phase	**Modeling**	**DTA**	**Metallography**
Liquidus	1346	1353	-
Bulk Solidus	1201	1265	1230
MC Eutectic	1261	1292	-
Laves Eutectic	-	1173	-
δ Solvus	1065	-	1002-1018
γ′ Solvus	995	963	954-982
γ′′ Solvus	968	-	-

4.1.3 Fusion Zone and HAZ Microstructures of Low and High Heat Input Welds of 718Plus

Optical micrographs of the fusion and heat affected zones (HAZs) of samples welded with the two heat inputs are shown in Figs. 4-3 a and b. No cracking was observed in the fusion zones of either of the two welded samples. However, the low heat input welds suffered HAZ cracking, while high heat input welds were free of HAZ cracks. SEM examination of the fusion zones of the welds revealed that they consisted of similar microstructure. As shown in Fig. 4-4, the weld fusion zones consisted of γ dendrites and Nb-enriched Laves-type phase in the interdendritic region. Also, large discrete carboboride and carbonitride particles, shown in top right and top left insets of Fig. 4-4, were observed within the fusion zone. Since fusion zone cracking did not occur in the samples welded with either of the two heat inputs, this work focuses mainly on the heat affected zone microstructures with an objective of understanding HAZ cracking in lower heat input weld and its absence in the higher heat input weld.

The SEM micrograph in Fig. 4-5 shows the HAZ microstructure of 718Plus plate that was welded using the low heat input welding conditions. Carboboride/ carbonitride particles that were present in the intergranular and intragranular HAZ regions closer to the weld fusion boundary exhibited interfacial liquation and were surrounded by resolidification constituents (inset of Fig. 4-5). Moreover, intergranular micro-cracks were observed, as shown in Fig. 4-5, in the HAZ regions while no cracking occurred in the weld fusion zone. The cracks were observed to have irregular/zigzag morphology that is typical of liquation cracks, and were often associated with grain boundary carboborides/carbonitrides, as shown in Figs. 4-6 a & b. Also, the cracks were usually outlined with re-solidification products marked with arrowhead on the inset in Fig. 4-6 b.

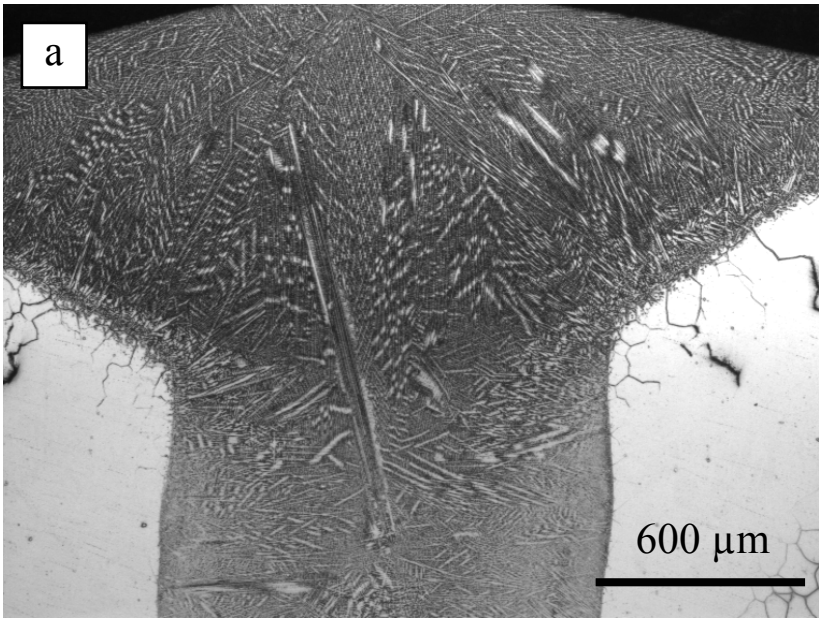

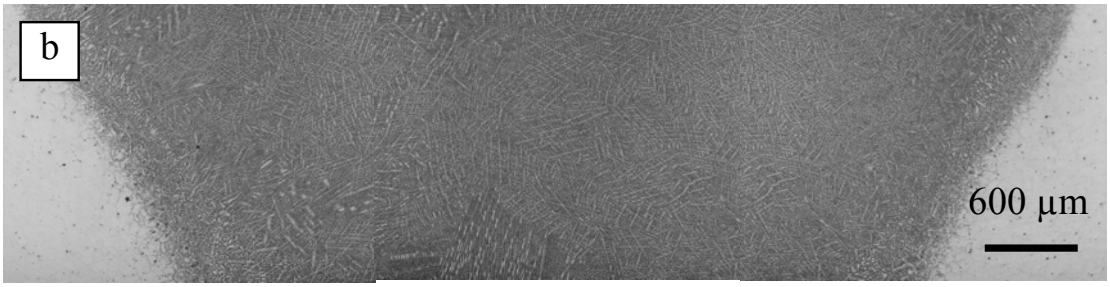

Fig. 4-3: Optical micrographs of the fusion and heat affected zones of (a) low heat and (b) high heat input welds of 718Plus

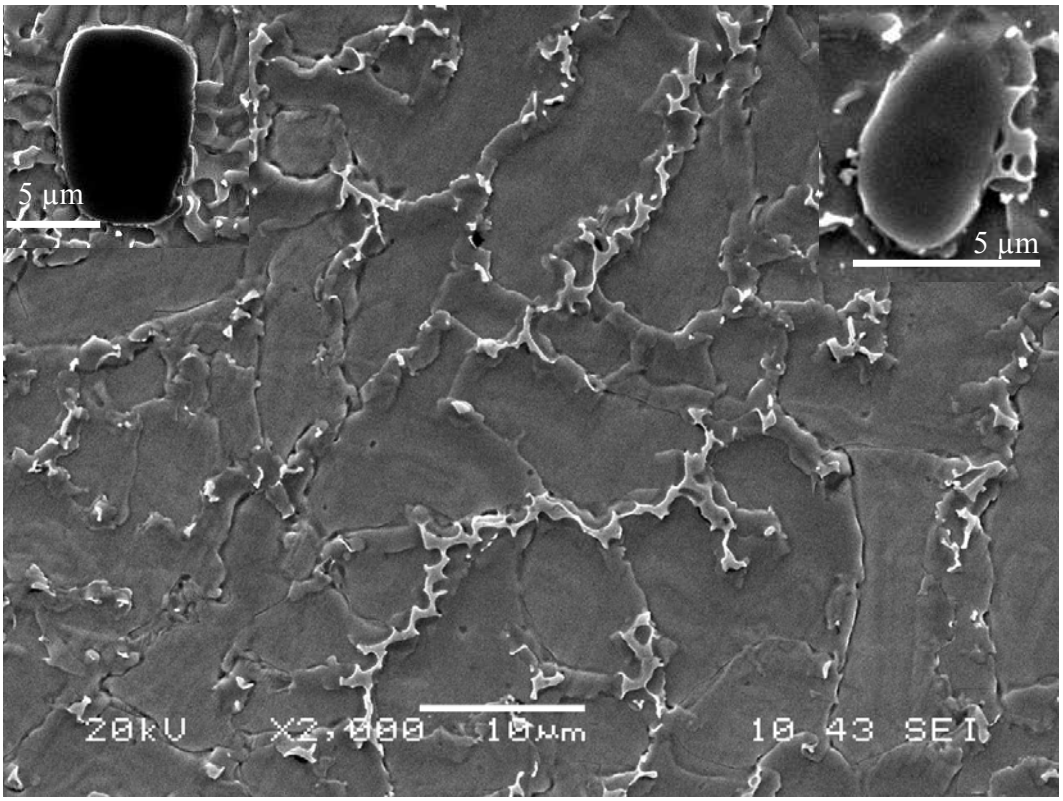

Fig. 4-4: SEM microstructure of the fusion zone of a laser weld of 718Plus. Top right inset shows Nb, Ti-rich carboboride while top left inset shows a Ti, Nb-rich carbonitride in the fusion zone.

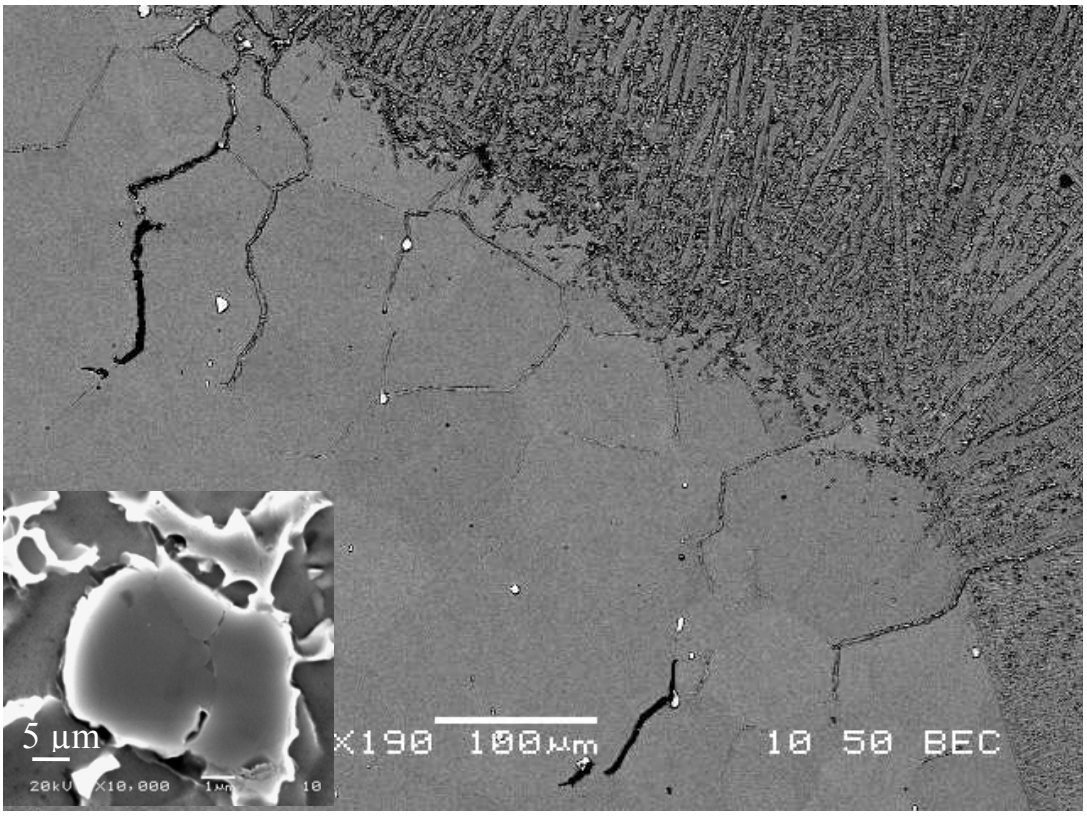

Fig. 4-5: SEM micrograph showing HAZ cracking in low heat input laser weld of 718Plus. Base inset shows interfacial liquation of Nb, Ti-rich carboboride in the HAZ.

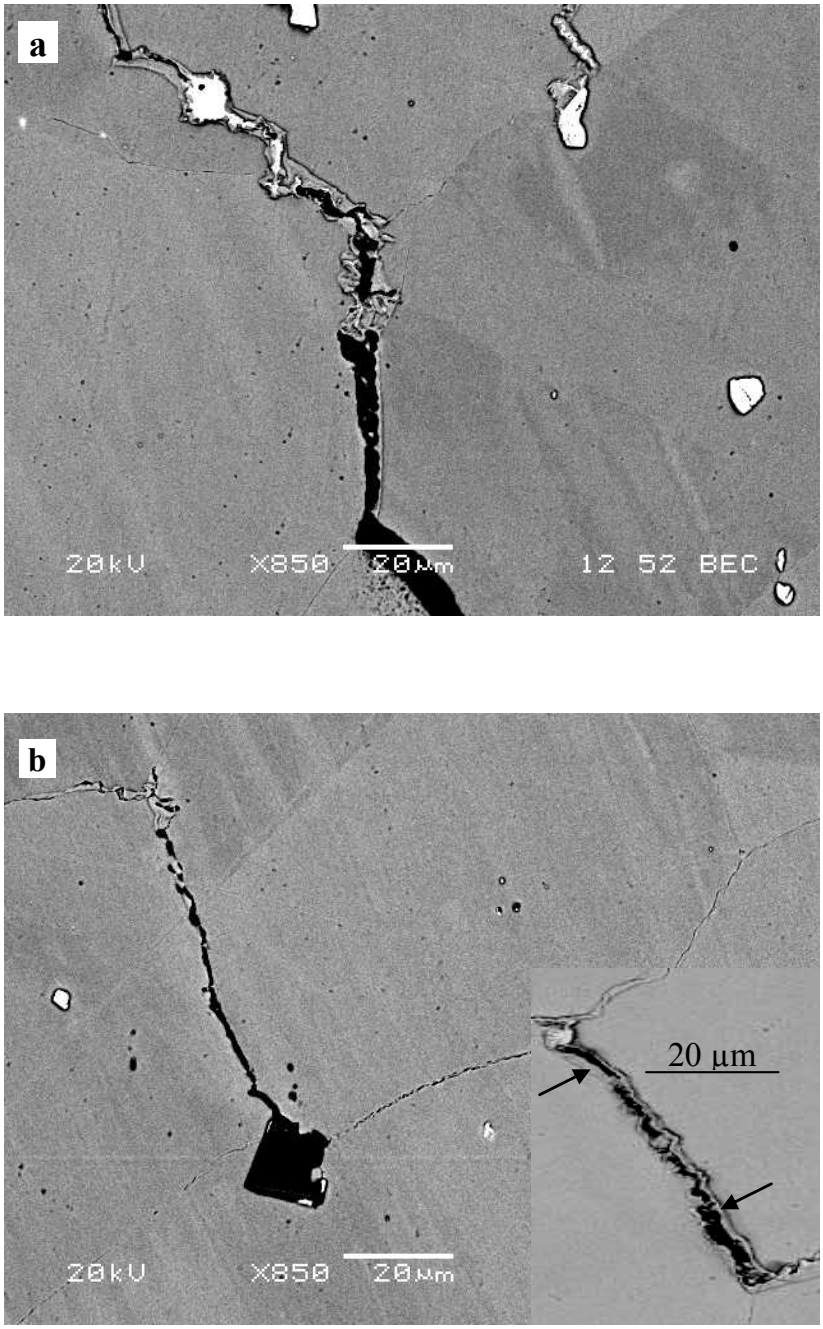

Fig. 4-6: SEM backscattered electron images of HAZ cracks associated with (a) Nb,Ti-rich carboboride and (b) Ti, Nb-rich carbonitride. Inset in (b) shows resolidification product outlining a crack

This suggests that HAZ cracking in the alloy is associated with the formation of liquid film on HAZ grain boundaries during weld thermal cycle. The SEM microstructure of HAZ of 718Plus plate that was welded using the higher heat input welding conditions is shown in Fig. 4-7. It is seen that the HAZ of the weld was marked with a more extensive liquation of grain boundaries and grain interior, but despite that, no evidence of cracking was observed in the samples.

As was discussed in the literature review (Chapter 2) HAZ grain boundary cracking occurs due to a combination of mechanical driving force, threshold tensile stress, and a crack susceptible microstructure such as with liquated grain boundaries. The liquation of a grain boundary in the HAZ during welding causes a solid-solid interfacial bond of the grain boundary to be replaced with a weaker solid-liquid bond. Consequently, this reduces the threshold stress that is required to cause grain boundary decohesion and, thus, the inherent resistance of an alloy to HAZ cracking during welding is reduced. However, if the induced stress in the HAZ is minimized, cracking can be reduced significantly or prevented, notwithstanding the occurrence of grain boundary liquation. In the absence of a substantial mechanical restraint, stresses are normally generated by differences in the rates of expansion and contraction of different regions in the HAZ as a result of thermal gradient created during welding. The magnitude of these stresses is influenced by weld cooling rates, which in turn is dependent on weld heat input. An increase in heat input during welding generally causes the rate of cooling to decrease for a given base metal thickness [109]. Although welds that were made with a relatively high heat input had more extensive grain boundary liquation and wider HAZ, the slow drop in temperature would reduce the magnitude of thermally generated stresses during cooling

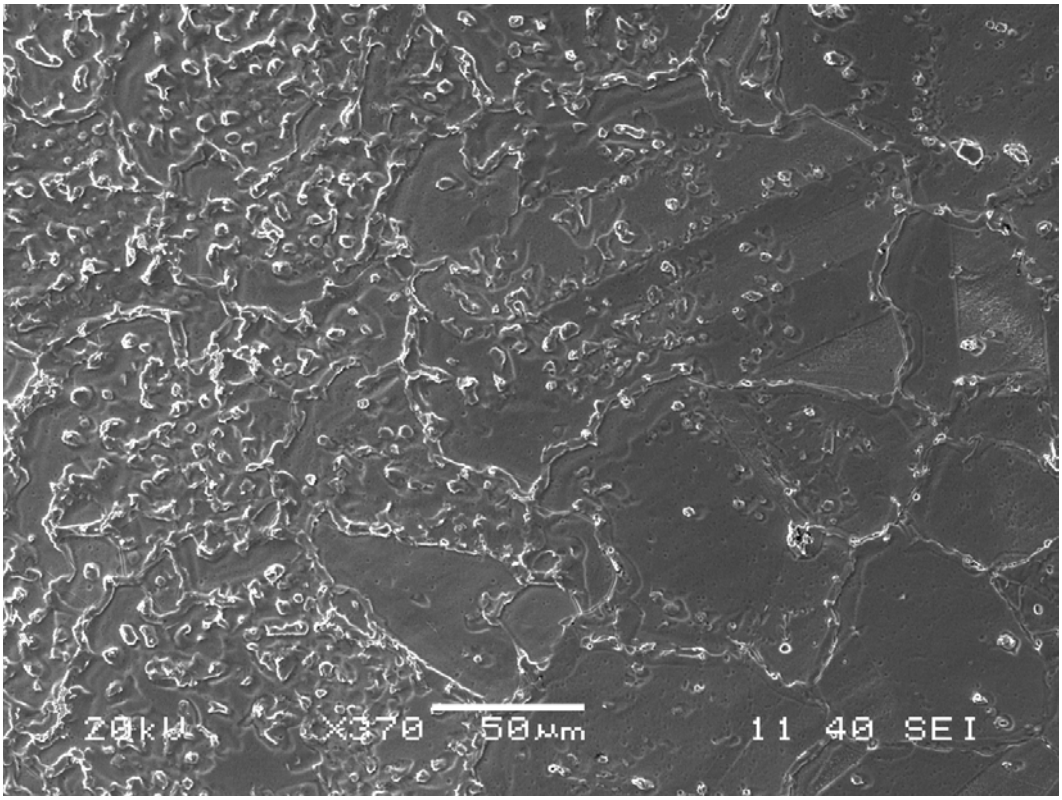

Fig. 4-7: SEM micrograph showing a crack-free HAZ of a high heat input laser weld of 718Plus. Note extensive liquation within HAZ grain interior and of grain boundaries.

of the welds [110]. Experimental evidence [110- 112] exists to show that HAZ cracking in engineering alloys was minimized by increasing heat energy input during welding. Therefore, thermally induced stresses in HAZ of welds can be reduced by increasing the weld heat input; such that cracking can be effectively reduced or prevented, as observed in the present work where high heat input laser welds of 718Plus were crack-free in comparison to welds made using low heat input welding conditions.

In addition to the thermal stresses, another possible factor that can affect the susceptibility of an alloy to intergranular HAZ cracking is the thickness of grain boundary liquid in the HAZ. Miller and Chadwick [113] have shown that for a grain boundary that is completely wetted by a thin liquid film of thickness h, the tensile stress, F_γ, required to overcome the grain boundary cohesion due to surface tension of the liquid, γ_L, is given by $F_\gamma = 2\gamma_L/h$. Thus, it is expected that the inherent resistance of HAZ grain boundaries to cracking during welding will decrease with an increase in the thickness of liquid produced by liquation in the heat affected zone. However, this does not mean that the actual occurrence of HAZ liquation cracking will monotonically increase with increase in liquid film thickness in a given alloy system. Cross et al [114] have reported that the degree of hot cracking of an aluminum alloy used in their study, as measured by total crack length (TCL), increased with an increase in the amount of terminal eutectic liquid up to a peak value beyond which further increase in the amount of liquid resulted in a decrease in the observed TCL. Moreover, it was reported in the classical work of Pellini [51] on hot tearing of castings, which to a first approximation is synonymous to HAZ cracking during welding, that hot tearing occurs when a “liquid film stage” is reached during solidification of castings. The liquid film stage is characterized by the

presence of a very thin film of liquid in the interdendritic regions of castings. Pellini [51] further reported that hot tears did not occur when the casting was in the "mushy zone" stage, which is characterized by the presence of a relatively wide interdendritic liquid. The prevention of hot tears during the mushy stage of solidification was attributed to a more uniform distribution of stresses/strains along the broader width of the interdendritic liquid that resulted in a generous flow of the pasty mass. Thus, a thicker film would be able to accommodate stresses/strains better than a thin liquid film [51]. Several other studies on the criteria necessary for hot cracking of castings, many of which were discussed in a detailed review by Eskin et al [115], have attributed hot cracking to the occurrence of insufficient interdendritic liquid flow and imposition of stresses/strains due to solidification shrinkage and thermal contraction during solidification. According to Clyne and Davies [116], hot tearing occurs during the last stage of solidification when the volume fraction of interdendritic liquid is too small to cause an appreciable relaxation of induced stresses/strains through liquid flow. Although, conventional wisdom may suggest that the strength of a grain boundary is reduced with a corresponding increase in thickness of liquid film on it, it seems the presence of an appreciable amount of liquid on intergranular regions of HAZ could favor stresses/strains relaxation in the liquated regions during welding, thereby reducing the occurrence of cracking. It is also possible for some of the cracks to be healed by intergranular liquid. Several investigators [60, 117-119] have reported the prevalence of HAZ cracking in sub-solidus regions of HAZ where extensive liquation did not occur, but significantly reduced level or absence of cracking in HAZ grain boundary regions that exhibited extensive liquation. According to Owczarski et al [118], the HAZ of Udimet 700 and Waspaloy, which contained relatively

small quantities of liquation products, exhibited a very high sensitivity to cracking, while cracking was prevented or reduced significantly close to the fusion zone where considerable liquation of grain boundaries occurred. Also, Ojo and Chaturvedi [119] recently reported that extensive grain boundary liquation could result in a reduced HAZ cracking. In the present work, HAZ cracking was not observed in high heat input welds (Fig. 4-7) where a significantly more liquation of grain boundaries occurred as compared to the low heat input welds (Fig. 4-5) which suffered a considerable amount of HAZ cracking. 718Plus was also autogenously TIG welded using a current of 60 Amps DC and 10 V at 76 mm/min, which translates to weld heat input of 472 J/mm. This heat input is the same as the one that was used for the high heat input laser welds. The TIG weld exhibited a wide HAZ marked with an extensive liquation, both of grain boundaries and within grain interiors, as shown in Fig. 4-8. However, it is of interest to note that no HAZ cracking occurred in the weld, despite the extensive HAZ liquation. Therefore, as was observed by Owczarski et al [118] in Udimet 700 and Waspalloy welds, 718Plus may be more susceptible to HAZ cracking when a relatively thin liquid film is present on the HAZ grain boundaries during welding.

In summary, welding of alloy 718Plus using a high heat input laser can minimize HAZ cracking by reducing the stresses generated in the HAZ. An increased volume of grain boundary liquid and the resultant relaxation of welding stresses is also another factor that could contribute to prevention of HAZ cracking in high heat input welds of the alloy.

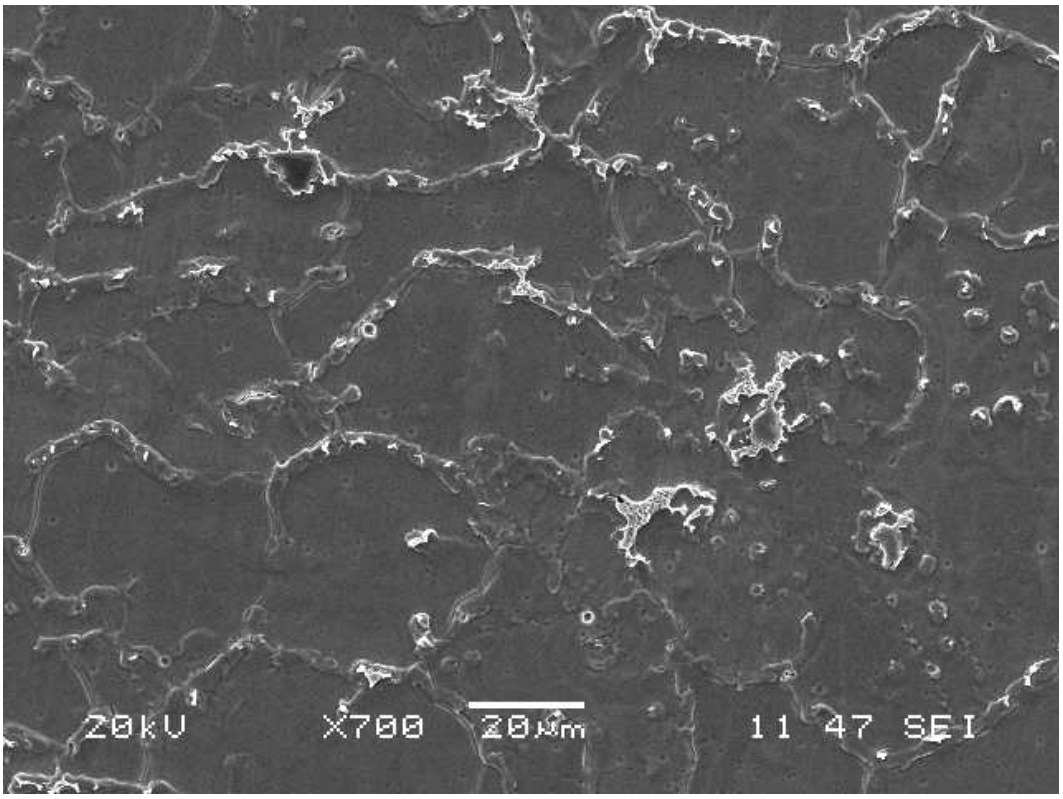

Figure 4-8: SEM micrograph showing a crack-free HAZ of a TIG weld of 718Plus. Note extensive liquation within HAZ grain interior and of grain boundaries.

4.1.5 The Occurrence of Liquid Backfilling in the HAZ of Low Heat Input Welds of 718Plus

An important phenomenon of liquid backfilling of cracks was observed in the HAZ grain boundaries of low heat input welds, which suggests that the extent of cracking observed in the welds was less than the amount of cracking that might have actually occurred during welding. SEM examination of the HAZ of the low heat input welds revealed that some of the grain boundaries, henceforth referred to as GX, one of which is shown in Fig. 4-9, contained densely distributed resolidification product and formed a continuous channel with terminal solidification constituents in the interdendritic regions of weld fusion zone. However, most other boundaries in the HAZ, henceforth referred to as GY, exhibited a thickened appearance (Fig. 4-10). Typically, the dense product on GX with thickness ranging from 6-10 μm, exhibited backscattered electron (BSE)-SEM contrast similar to that of the BSE-SEM of the terminal solidification constituents in the interdendritic regions of the weld fusion zone, but different from the BSE-SEM image contrast from GY boundaries. This suggests that the resolidification constituents on GX and GY have different chemical composition. Semi-quantitative SEM/EDS analyses, given in Table 4-3, confirmed that the dense product on GX grain boundaries has a composition similar to that of the terminal solidification constituents in the interdendritic regions of the weld fusion zone, but contained a significantly higher concentration of niobium than the liquation product present on GY grain boundaries. It has been reported by several investigators [120] that the nature of resolidification products formed on HAZ grain boundaries depends to a large extent on the solidification mode of the dominating grain boundary liquid. Resolidification of HAZ grain boundary liquid can occur through either of two different solidification modes, viz., normal dendritic solidification or liquid

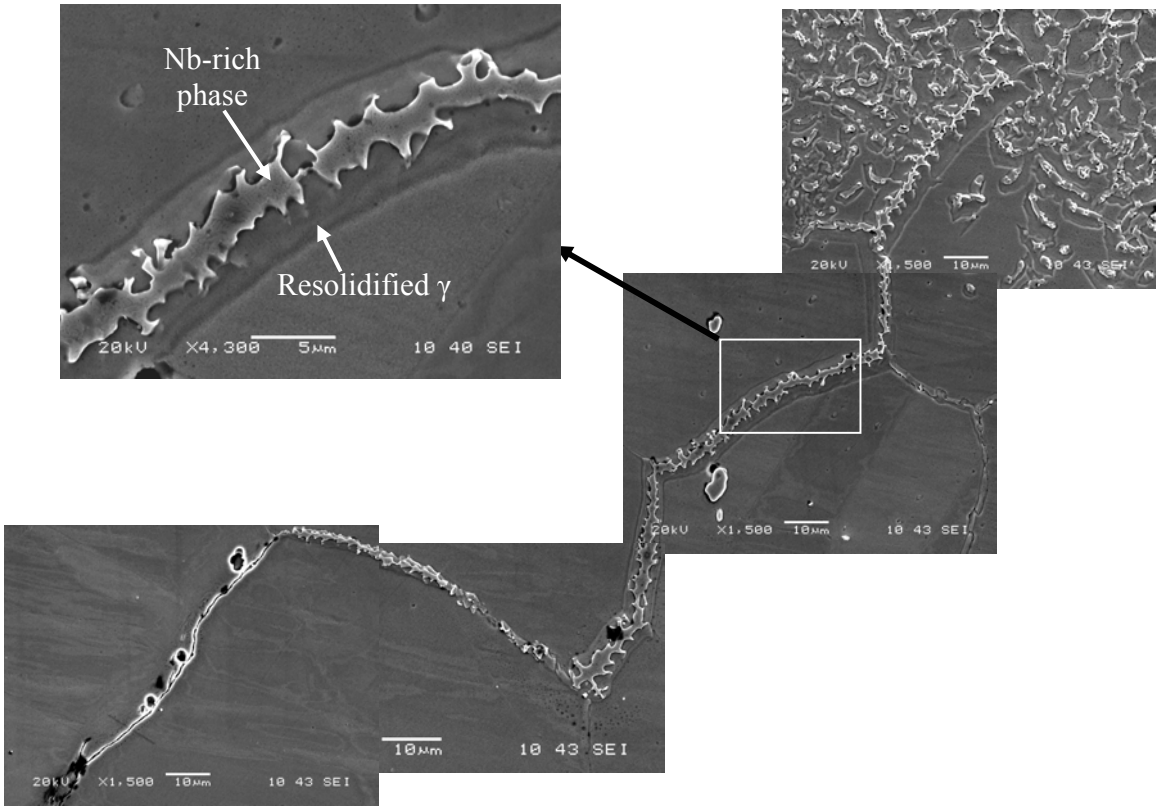

Fig. 4-9: SEM micrograph of incompletely backfilled crack in weld HAZ of low heat input laser weld of 718Plus. Resolidification products on the boundary are shown at higher magnification (x4300).

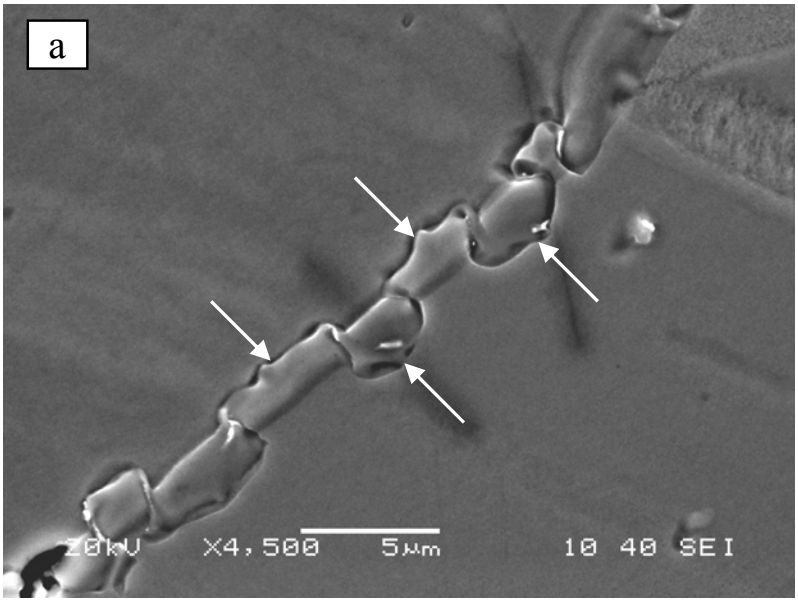

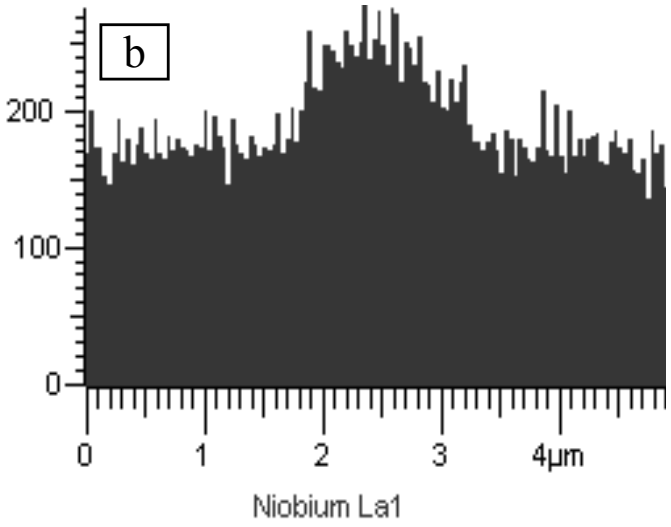

Fig. 4-10: SEM a) micrograph showing the thickened appearance and reverse curvature of HAZ grain boundary (GY) due to LFM, b) X-ray line scan showing Nb-enrichment of a migrated region around GY compared to adjacent γ matrix.

Table 4-3: Chemical composition, excluding B, C and N, (wt. %), of backfilled and migrated regions of HAZ grain boundaries (GB), and interdendritic constituent in weld fusion zone of 718Plus.

	Al	Ti	Cr	Fe	Co	Ni	Nb	Mo	W
Backfilled GB	1.0	1.6	14.0	6.2	8.5	44.5	19.6	3.5	1.1
Migrated GB	1.4	0.9	18.2	9.4	9.9	51.7	6.0	2.5	-
Interdendritic constituent	1.1	1.2	14.7	6.7	9.0	41.6	20.9	3.4	1.4

film migration (LFM). In a system where solidification by LFM is predominant vis-à-vis normal dendritic solidification, the formation of secondary terminal solidification products, which normally result from dendritic mode of solidification of grain boundary liquid, can be prevented. One of the significant factors which determine the effectiveness of LFM in a system is the initial thickness of the liquid film produced during welding. According to Baker and Purdy [121] the time t required to solidify an initial liquid film of thickness $\delta(o)$ is given by $t = \delta(o)/2kv_o$, where k is the equilibrium solute distribution coefficient and, v_o is the initial migration velocity of the liquid film which is given by the expression, $v_o = D_L(\Delta C)_o/(C_{L,T} - C_{S,T})\delta(o)$. D_L is the diffusivity of solute in the liquid, $(\Delta C)_o$ is the initial concentration difference across the liquid film, $C_{L,T}$ and $C_{S,T}$ are the equilibrium interfacial concentrations of solute in the liquid and solid phases. From these expressions, it can be deduced that the initial velocity of liquid film migration is reduced with an increase in the liquid film thickness, while the time required for solidification through LFM is increased. Thus, a critical liquid film thickness may be reached beyond which LFM becomes more or less ineffective with a consequential solidification of the liquid into terminal secondary products via normal dendritic solidification. LFM seems to be the predominant solidification mode on GY, as the reverse grain boundary curvature peculiar to GY, shown in Fig. 4-10, is one of the main characteristic of the occurrence of liquid film migration [122-124]. Due to the migration of liquid film segments on GY into γ matrix, the chemical composition of the region around GY is expected to change. Therefore, the thickened resolidification regions, which are slightly richer in niobium compared to the adjacent austenitic γ matrix of 718Plus, as seen in the SEM X-ray line scan on Fig. 4-10 b, confirmed the occurrence of LFM on GY grain boundaries. As stated

earlier, a dense resolidification product was observed on GX (Fig. 4-9). Moreover, the boundaries showed no features or evidence of the occurrence of LFM. Instead, the liquid predominantly solidified at the solid-liquid interfaces in a normal solidification mode, which is characterized by a simultaneous nucleation/growth of γ dendrites and rejection of positively segregating solute(s), e.g. Nb, into the liquid. This resulted in the formation of Nb-enriched secondary terminal solidification product, which was outlined by resolidified single phase γ solid solution, as shown in the higher magnification SEM micrograph of Fig. 4-9. It is of interest to note that the initial thickness of liquid film, i.e. the width of newly formed solid γ and Nb-rich product (Fig. 4-9), on GX boundaries was measured by SEM to be approximately 8 μm. This was far greater than the average thickness of 2-3μm of the initial liquid film on GY boundaries that solidified by LFM mode (Fig. 4-10). Thus, the ensuing normal mode of solidification of GX boundaries may be attributed to the initial relatively large volume of liquid on the boundaries which prevented an alternative mode of liquid solidification by LFM. The deep and continuous penetration of these HAZ boundaries by thick liquid film, which transformed to Nb-rich products during terminal stage of solidification, suggests the occurrence of backfilling from weld fusion zone. Although the constitutional liquation of HAZ carbides, which can be another major source of grain boundary liquid, was observed in the present work, it should be noted that no preferential liquation of these carbides was observed on or close to the GX boundaries compared to the GY boundaries in regions within a comparable distance from the weld fusion zone. Thus, the secondary terminal solidification product on GX boundaries, which formed continuous channels to the fusion zone and had chemical composition similar to that of the terminal solidification constituents in the

interdendritic regions of weld fusion zone, may have resulted due to backfilling of liquid from the fusion zone. It has been reported in the works of Savage et al [125], and Lundin et al [126] that for a HAZ grain boundary crack to be backfilled, it should be contiguous to the weld fusion zone when sufficient liquid is present in interdendritic regions of weld fusion zone to flow into the cracks. Thus, the suggestion that the dense resolidification product resulted from liquid backfilling of cracks from weld fusion zone is further supported by the observation of cracks beyond the backfilled length of the grain boundaries, as shown in Fig. 4-9. The presence of the cracks might be due to the insufficient penetration of liquid from fusion zone interdendritic region into pre-existing cracks before a complete "freezing" of the liquid during weld cooling cycle. Also, no evidence of backfilling was observed on HAZ cracks that were not contiguous to the weld fusion zone. In summary, the observations of this work suggest that backfilling of liquid into cracked grain boundaries that are contiguous to weld fusion zone occurred in low heat input laser welds of 718Plus alloy.

During welding of an alloy, the existence of grain boundary liquation and sufficient level of tensile stress induced by thermal gradients and/or mechanical constraints may result in intergranular cracking in the HAZ. If the HAZ cracks are contiguous to weld fusion zone, and cracking occurs at a time when significant amount of liquid is present in interdendritic regions of weld fusion zone, the liquid may wet the cracked surfaces and be drawn into the cracks through a capillary action [125-127]. Liquid backfilling may be an important crack healing mechanism for alloys that are susceptible to HAZ cracking during welding. However, for the cracks to be effectively healed through liquid backfilling mechanism, the liquid should be drawn into and fill the

cracks within a time, t, that is shorter than the time required for a complete solidification of the terminal liquid in the weld fusion zone. To a first approximation, the time required to backfill a crack is governed by the rate of penetration of capillary spaces and can be estimated by classical surface tension theory [120]. For the early stage of penetration into a capillary space of any inclination, the time, t, required for a liquid to reach a height h is given by [128], $t = 2\eta h^2 / (r\gamma Cos\theta)$, where η is the viscosity of the liquid, θ is the contact angle, r is radius of the capillary and γ is the surface tension of the liquid. This expression suggests that substantial backfilling of HAZ grain boundary cracks can occur within a short period of time if the interdendritic liquid has a sufficiently low viscosity, high surface tension and good wetting property. These properties are affected by composition of the alloy. Savage et al [125] have reported that the addition of Mn, P, S and Si to Inconel 600 enhanced the occurrence of backfilling during welding of the alloy. Some of these elements, which were reported to lower the viscosity and improve fluidity of Inconel 600 [125], are also present as minor additions in 718Plus (Table 3-1). Moreover, the occurrence of positive segregation of Nb ($k < 1$) during dendritic solidification, as was observed during solidification of 718-type alloys [129], can lower the effective solidus temperature of the interdendritic liquid involved in backfilling of HAZ cracks in 718Plus. This will allow the liquid in 718Plus welds to exist to a much lower temperature which would provide the time required for backfilling of HAZ cracks to occur. Therefore, the chemical composition of 718Plus might be also promoting the backfilling and healing of HAZ cracks in its low heat input welds.

4.2 Influence of Pre-weld Heat Treatments on Weld Heat Affected Zone Cracking of 718Plus

4.2.1 Introduction

Although HAZ cracking was prevented by welding with a high heat input laser, it resulted in a significant damage to the parent microstructure through its extensive liquation. Therefore, such a technique is not usually recommended in order to ensure high integrity of weld structures. Thus, it is necessary that another approach be employed to minimize or eliminate HAZ cracking of the alloy during welding. The use of suitable pre-weld heat treatment to engineer pre-weld microstructure capable of reducing or eliminating cracking during welding has been widely reported. For example, extensive work in our research group has shown that cracking may be significantly minimized in Inconel 718, of which 718Plus is a derivative, through the selection of an adequate pre-weld thermal treatment which minimized segregation of deleterious elements like boron to HAZ grain boundaries before welding. Therefore, the aim of the present work was to investigate the influence of pre-weld heat treatments on the cracking behavior of 718Plus. Ultimately, a pre-weld heat treatment schedule that would be capable of preventing the occurrence of HAZ cracking during welding would be sought.

Prior to welding, as shown in Table 3-2, 718Plus was thermally solution heat treated for 1 hour in an argon atmosphere in a furnace at 950^{o}C, 1050^{o}C, and 1150^{o}C. The heat treated coupons were cooled from the solution heat treatment temperatures at various rates ranging from iced-water quenching (≈ 500^{o}C/s), air cooling (≈ 25^{o}C/s), to furnace cooling (≈ 0.25^{o}C/s). The SIMS technique was used to analyze grain boundary distribution of boron in the coupons, while microstructural analyses were carried out on

solution heat treated and welded coupons using optical microscope and SEM. The results of these analyses, which establish the influence of pre-weld heat treatments on the cracking behavior of 718Plus are presented and discussed.

4.2.2 Microstructure of Pre-weld Solution Heat Treated 718Plus

Figs. 4-11 a, b, c and 4-12 a, b, c show SEM microstructure of 718Plus after solution heat treatment for 1 hr at 950^{o}C and 1050^{o}C, respectively. Samples that were heat treated at 1150^{o}C had microstructures similar to those treated at 1050^{o}C. Generally, after the solution heat treatment at 950^{o}C, and at all the cooling rates employed, the alloy contained dispersed blocky shaped precipitates of Nb, Ti-rich carboborides and Ti, Nb-rich carbonitrides in intergranular and intragranular regions of its γ solid solution matrix. Also, grain boundary regions of the alloy were outlined by secondary precipitates of δ-phase having platelet or blocky morphology. In addition to the carbides and δ phase, precipitates of γ′ particles were observed within the γ matrix of the furnace cooled samples. High magnification SEM image showing the spherical shaped γ′ particles is shown in the top right inset of Fig. 4-11c. The γ′ particles precipitated from γ matrix during continuous cooling of 718Plus in the furnace at a slow rate (≈ 0.25^{o}C/s). Specimens heat treated at 1050^{o}C and 1150^{o}C contained micro-constituents similar to those observed in the samples that were heat treated at 950^{o}C, with the exception of δ phase. δ phase precipitates were not observed after the solution treatments at 1050^{o}C and 1150^{o}C because these temperatures are above the solvus of δ phase in 718Plus which has been reported to be in the range of 1002–1018^{o}C [25]. A notable difference was also observed in the grain size of the samples after heat treatments. The optical micrographs in

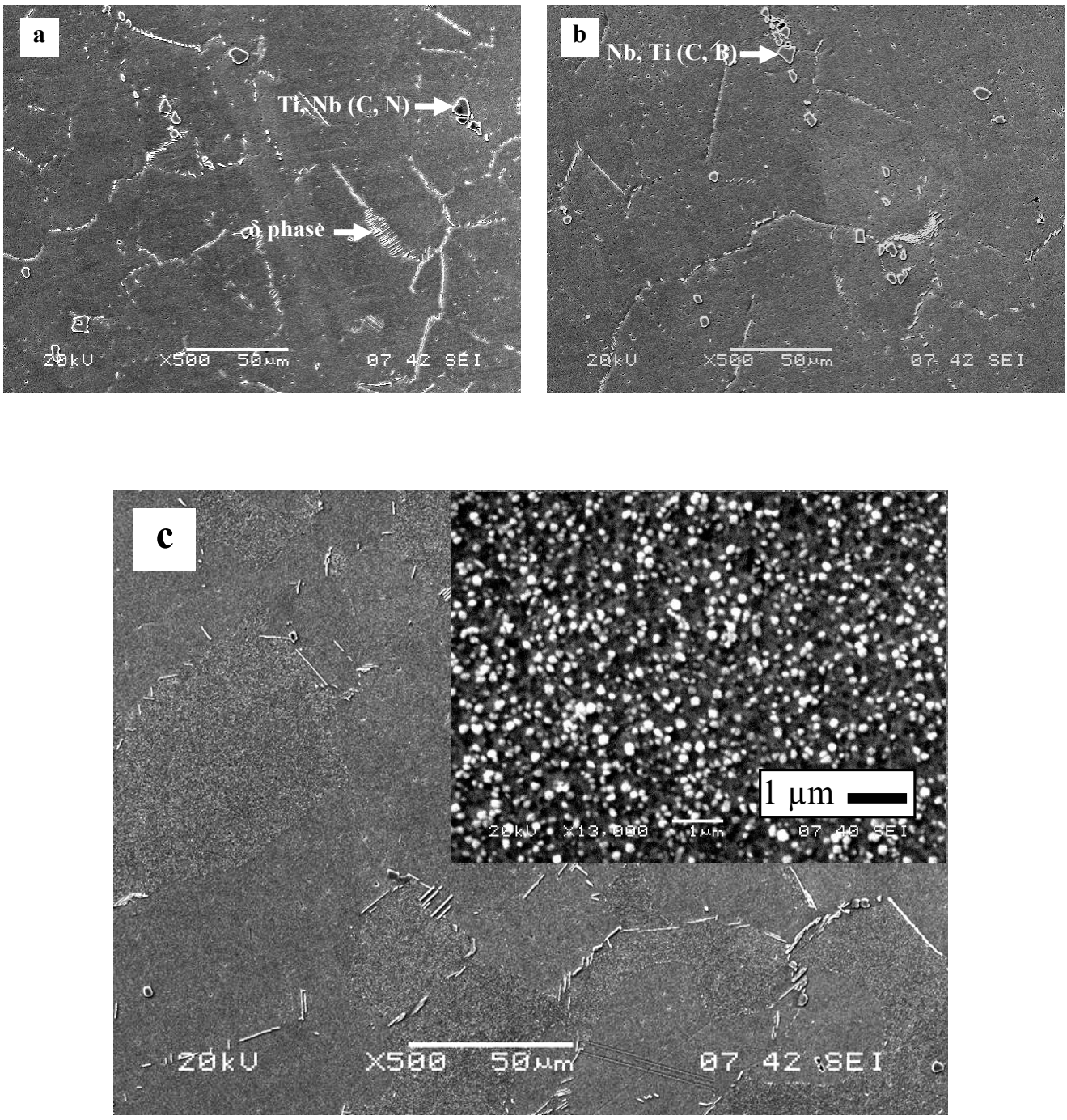

Figure 4-11: SEM microstructure of 718Plus solution heat treated at 950°C and a) iced water quenched, b) air cooled, c) furnace cooled. The top right inset on 1c shows γ′ particles in γ matrix of the furnace cooled samples.

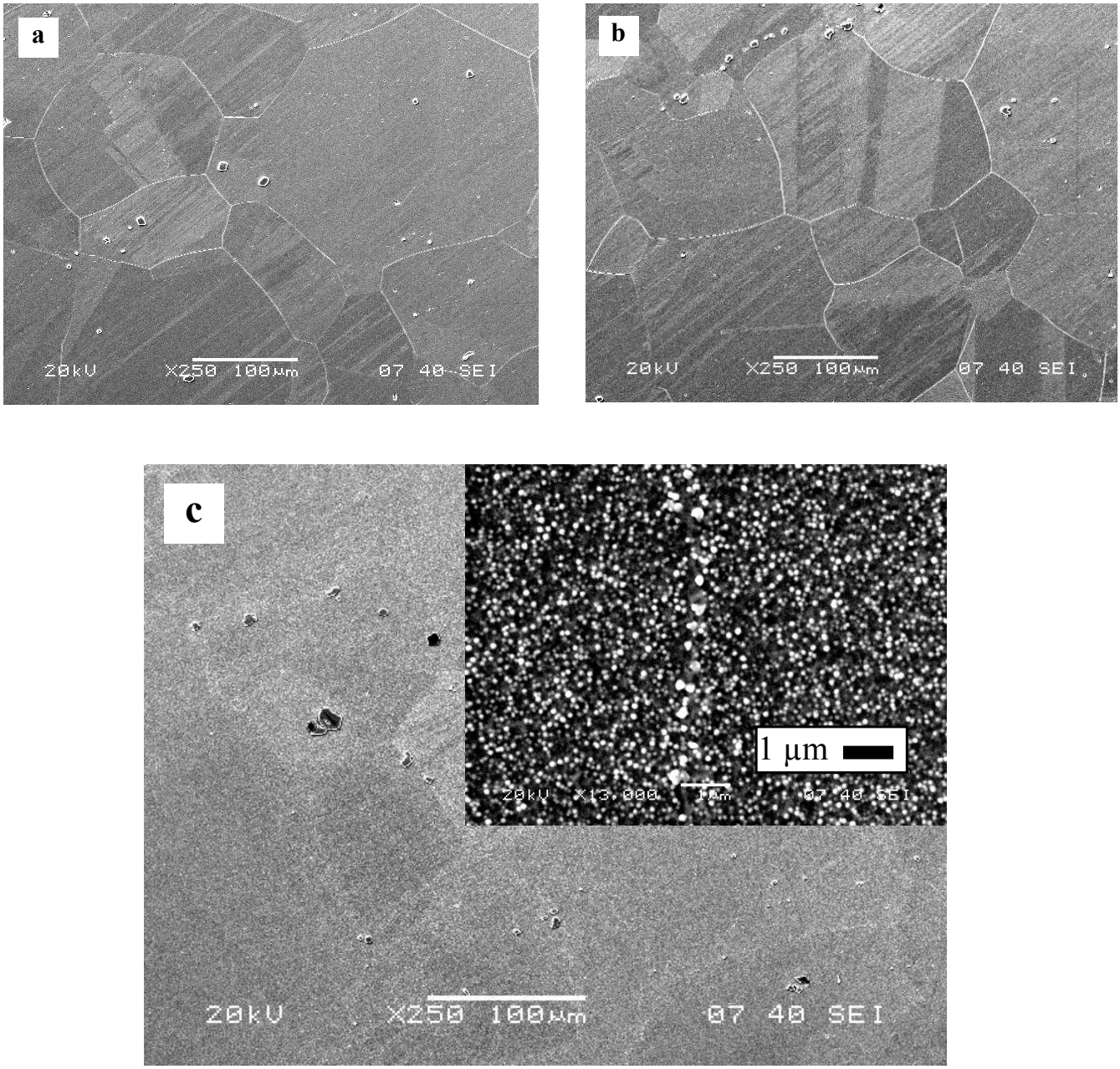

Fig. 4-12: SEM microstructure of 718Plus solution heat treated at 1050^{o}C and a) iced water quenched, b) air cooled, c) furnace cooled. The top right inset on 1c shows γ′ particles in γ matrix of furnace cooled samples.

Figs. 4-13 a-c show the grain sizes of specimens solution heat treated at 950°C (≈ 58 μm grain size), 1050°C (≈ 120 μm grain size) and 1150°C (≈ 360 μm grain size), respectively, and air cooled. The micrographs depict the variation in grain size of the alloy after these heat treatments. Approximate mean diameter of the grains after all the pre-weld solution heat treatments are presented graphically in Fig. 4-14. It is seen that no significant variation in grain size occurred with variation in cooling rate. However, the grain size increased approximately by a factor of two and six when heat treatment temperature was increased from 950°C to 1050°C and 1150°C, respectively. The dramatic grain growth that occurred at 1050°C and 1150°C can be attributed to the dissolution of δ phase precipitates during heat treatments at these temperatures, as shown in Figs. 4-12. It is known that δ phase pins grain boundaries, and thereby prevents/limits grain growth during high temperature exposure [15]. Thus, no significant grain growth occurred during the treatment at 950°C where the grain boundaries were outlined and successfully pinned by δ phase (Fig. 4-11).

4.2.3 HAZ Microstructure of Welded Alloy

The SEM backscattered electron (BSE) image in Fig. 4-15 shows weld HAZ microstructure of the specimen that was pre-weld heat treated at 950°C and quenched in iced water. Liquation of MC-type carbide particles was occasionally observed in the HAZ region closer to the fusion zone of the weld. Also, grain boundary liquation was observed in HAZ region up to about 250 μm from the fusion zone, but HAZ cracking was not observed. The samples that were pre-weld heat treated at 950°C and air or furnace-cooled were also crack-free. Their HAZ microstructures were similar to those of the

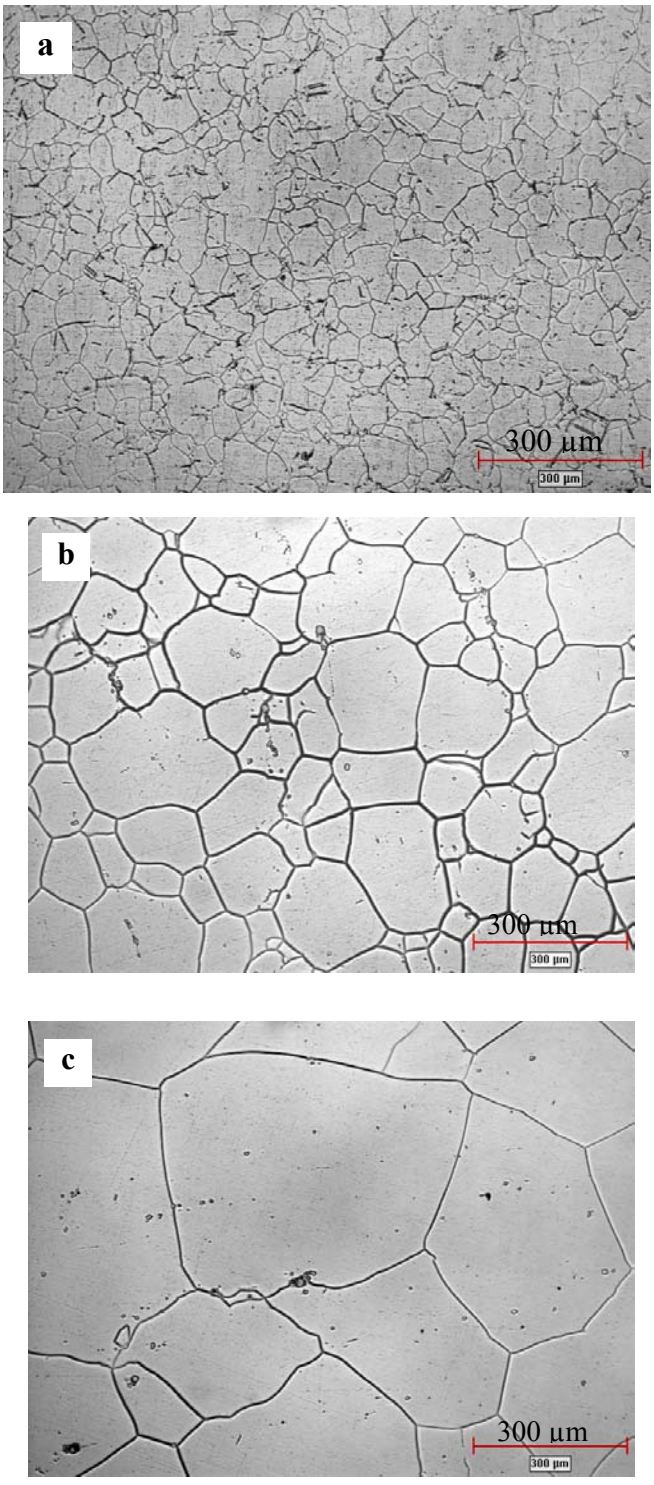

Fig. 4-13: Optical micrographs (x100, 10% oxalic etch) of 718Plus showing the variation in grain size after solution heat treatment at a) 950°C, b) 1050°C, c) 1150°C and followed by air cooling.

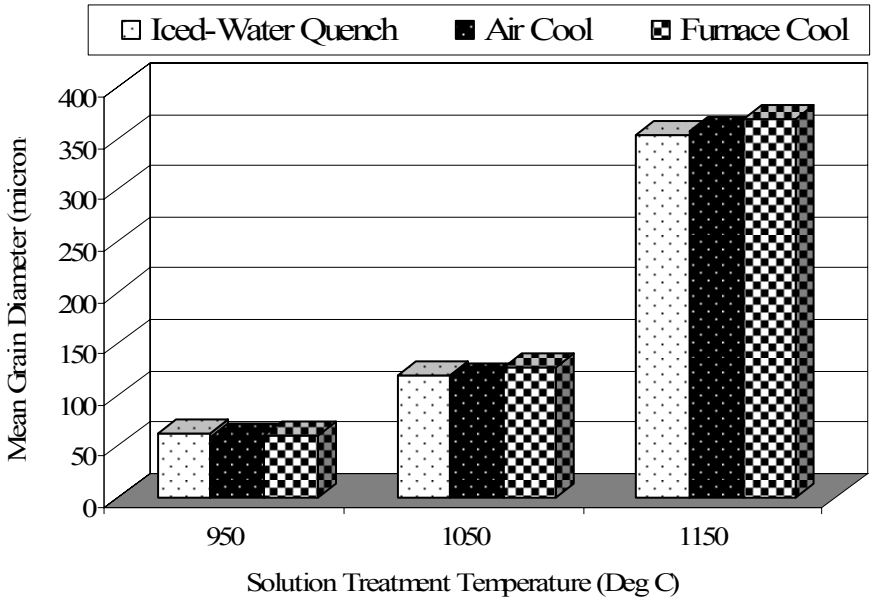

Figure 4-14: Variation in average grain size of 718Plus with pre-weld heat treatment temperature and cooling rate.

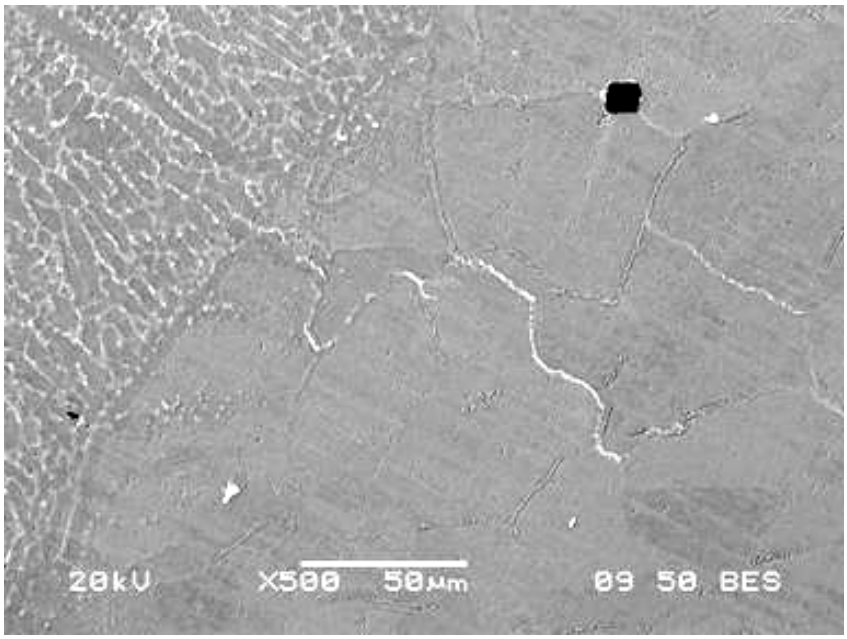

Fig. 4-15: SEM micrograph showing the absence of HAZ cracking in the weld of 718Plus that was pre-weld solution heat treated at 950^{o}C and iced water quenched.

samples that were quenched in iced-water (Fig. 4-15). However, SEM microstructures of the pre-weld and weld HAZ of furnace cooled sample (Figs. 4-16 a & b) suggests that liquation of γ′ particles occurred in the heat affected zone during welding. The underlying mechanism of the constitutional liquation of γ′ precipitates in γ′ strengthened nickel base superalloys has been discussed in details in the work of Ojo et al [130-131]. An explicit consideration of the potential effects of this on the weldability of 718Plus (in aged condition) is a subject of future work. However, it has been reported [130-131] that liquid film from constitutionally liquated γ′ precipitate can contribute to weld HAZ cracking if it penetrates and wets HAZ grain boundaries.

The weld HAZ microstructures of samples that were pre-weld heat treated at 1050^{o}C and 1150^{o}C, respectively, were similar to those that were heat treated at 950^{o}C. However, HAZ cracks were observed in the samples that were pre-weld heat treated at 1050^{o}C and 1150^{o}C. Representative optical and SEM images of a cracked region are shown in Figs. 4-17 a & b, respectively. As shown in the figures, the cracks were mostly present within the neck region of the nail head shaped welds. The degree of cracking in these samples was quantified by the measurement of total crack length (TCL). The average value of TCL observed in variously heat treated material is shown in Fig. 4-18. It is seen that cracking was not observed in the welds in samples that were pre-weld heat treated at 950^{o}C and cooled at the three cooling rates. However, as shown in Fig. 4-18, HAZ cracking occurred in the welds when the pre-weld heat treatment temperature was increased to 1050^{o}C and 1150^{o}C. Fig. 4-18 also shows that, at 1050^{o}C and 1150^{o}C, the highest degree of cracking occurred in air cooled samples. This was followed by furnace cooled samples, while the lowest extent of cracking was found in samples that were

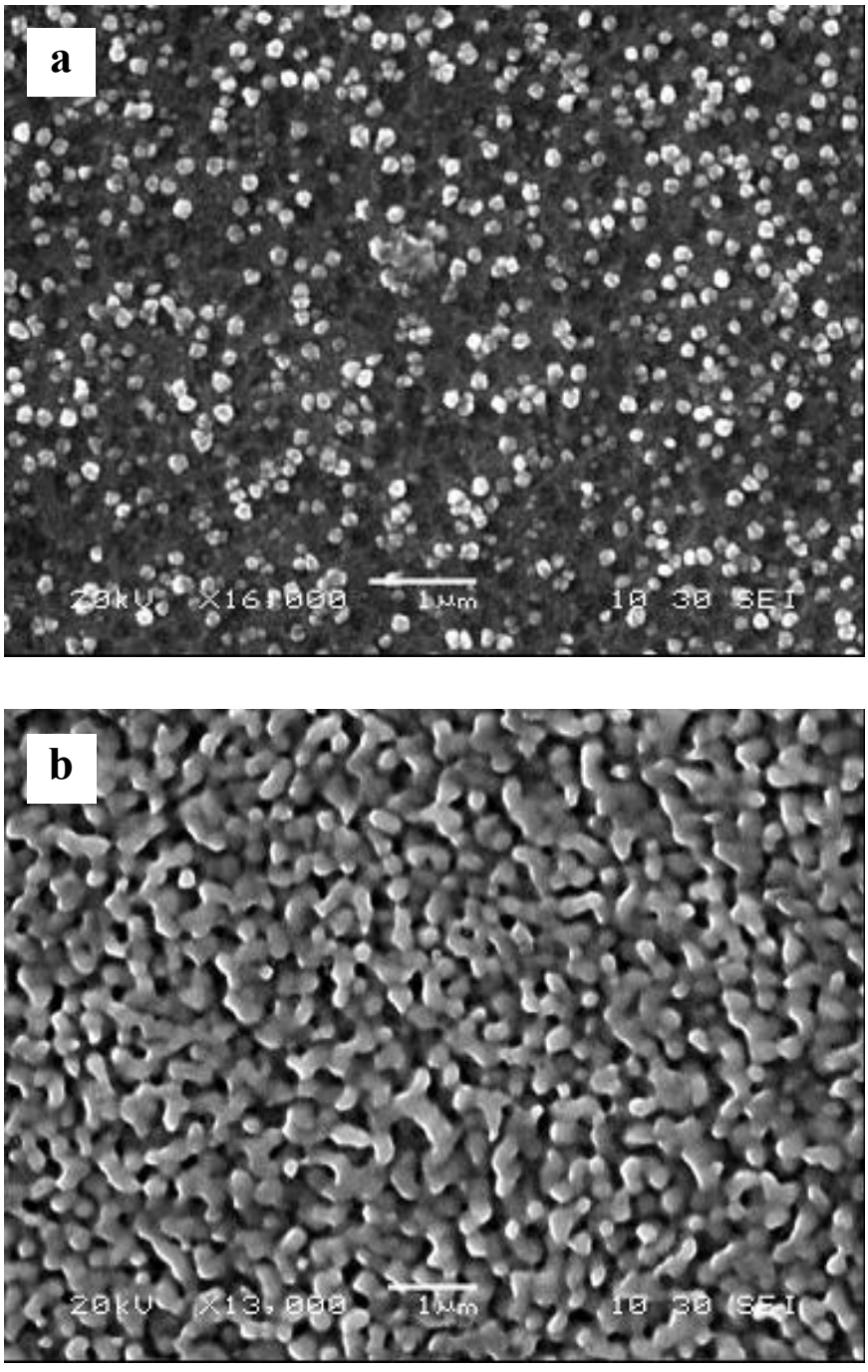

Fig. 4-16: SEM micrographs showing γ′ particles a) before welding (i.e. after 950^{o}C + furnace cool), and b) after welding (in the HAZ).

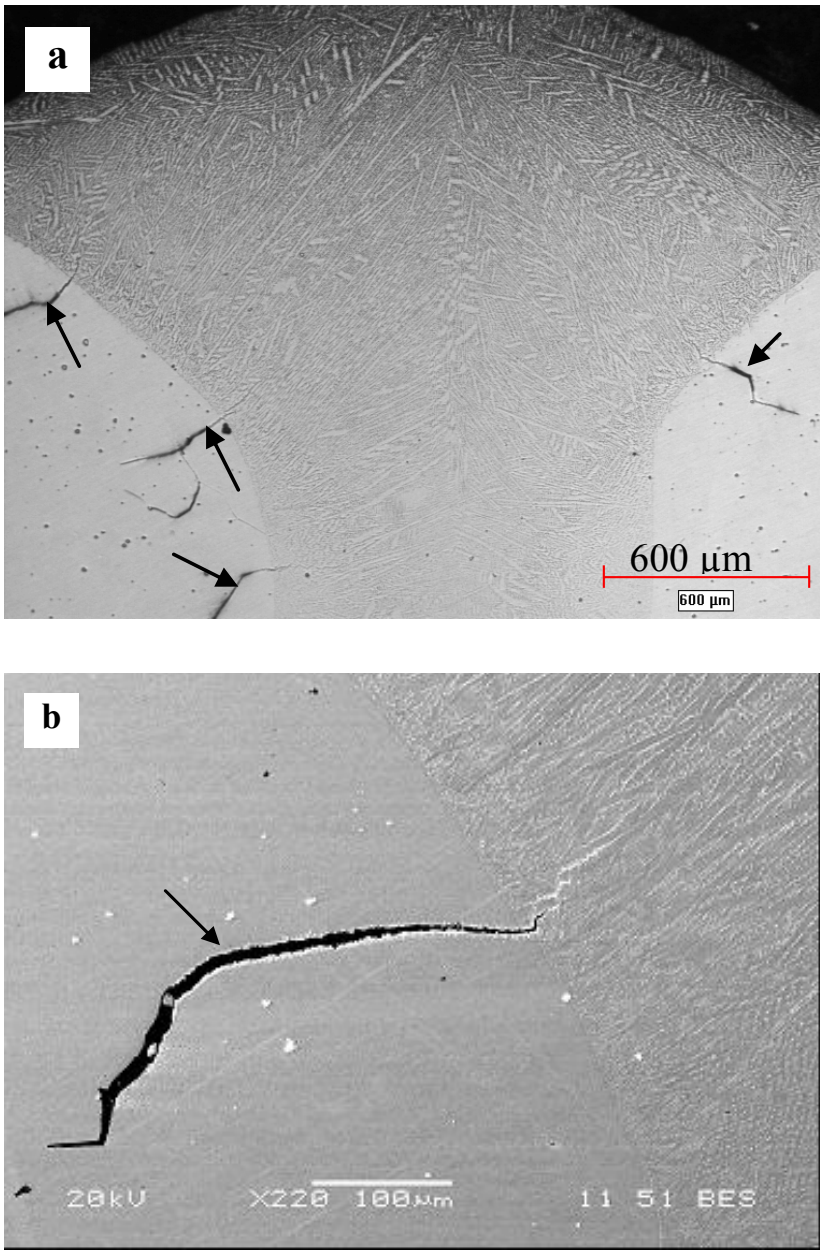

Fig. 4-17: a) Optical, and b) SEM micrographs showing cracking in the weld HAZ of 718Plus that was pre-weld solution heat treated at 1150^{o}C + air cool.

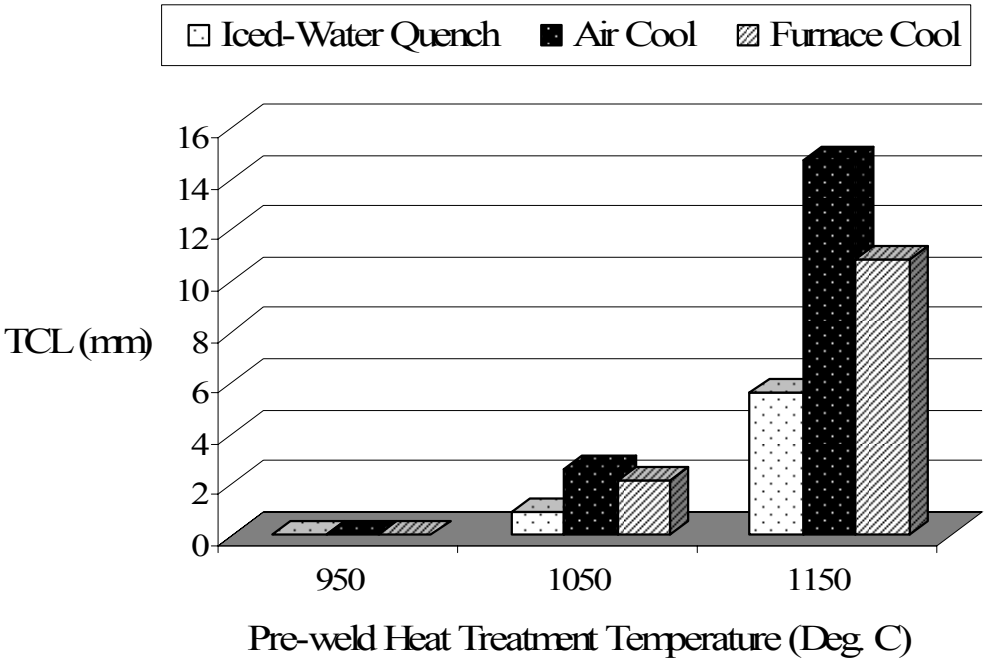

Fig. 4-18: Variation in HAZ total crack length (TCL) of 718Plus with pre-weld heat treatment temperature and cooling rate.

quenched in iced-water. At all the three cooling rates, the degree of cracking was always higher in samples pre-weld heat treated at 1150^{o}C compared to those that were heat treated at 1050^{o}C. Although constitutional liquation of MC-type carbides was observed in this work, and has been reported to contribute to HAZ cracking in 718Plus [68], a careful study of the variation of cracking with pre-weld heat treatment temperature and cooling rate, which did not affect the volume fractions of constitutionally liquating MC-type carbides, suggested that cracking was more influenced by two main factors, viz., segregation of B and grain size of the material, which are discussed next.

4.2.4 Effect of Pre-weld Heat Treatments on Grain Boundary Segregation of Boron and HAZ Cracking

The cause of intergranular cracking that often occurs in HAZ of austenitic alloys during welding is generally attributed to a combination of mechanical driving force for cracking; threshold tensile welding stresses, and a crack susceptible microstructure such as with liquated grain boundaries. The liquation of a HAZ grain boundary during welding causes its solid-solid interfacial bond to be replaced by a weaker solid-liquid bond. Consequently, this reduces the threshold tensile welding stress that is required to cause the liquated grain boundary's decohesion. Thus, the inherent resistance of an alloy to HAZ cracking is reduced by the liquation reaction. Grain boundary liquation can occur by either equilibrium supersolidus or non-equilibrium subsolidus melting. However, the mere occurrence of liquation reaction is not sufficient to produce a crack susceptible microstructure; it is essential that the liquid film penetrates and wets the grain boundaries and is stable over a wide range of temperature to allow enough stresses to build up during weld cooling. The presence of positively partitioning elements (i.e. $k < 1$), particularly

boron, enhances the wettability and increases the stability of grain boundary liquid film, and boron has been described as the most detrimental element causing grain boundary liquation cracking [54, 64, 103], although, it improves creep-rupture life of the alloy. Boron is particularly more detrimental as it has a tendency to preferentially segregate to grain boundaries during thermo-mechanical processing of an alloy, or thermal treatments prior to welding.

The thermally induced grain boundary segregation of solute atoms, e.g. boron, is a diffusion controlled process that can occur by two mechanisms, viz., equilibrium segregation and non-equilibrium segregation. As was discussed earlier, equilibrium segregation occurs when a polycrystal is held at a sufficiently high temperature to permit appreciable diffusion of misfit impurity atoms within its grains to loosely packed interfaces, e.g. grain boundaries. The impurity atoms are absorbed by such interfaces in order to reduce their free energy [71], and are thereby said to "segregate" to the interface. The extent of such equilibrium segregation is known to decrease with an increase in heat treatment temperature, but is independent of cooling rates. On the other hand, thermally induced non-equilibrium segregation [74, 132], as its name suggests, occurs under non-equilibrium thermal conditions, particularly when cooling from elevated temperatures over a range of cooling rates. This type of segregation has been widely described by a solute drag mechanism [133, 134], which involves the following. During high temperature annealing an equilibrium concentration of vacancies is generated and distributed within the grain interior of a polycrystal. As the temperature decreases during cooling, the grains become supersaturated with vacancies. Since grain boundaries act as perfect sinks for point defects, a vacancy concentration gradient is set up between the

supersaturated grains and the boundaries [78]. Consequently, vacancies diffuse down the concentration gradient to grain boundaries where they are annihilated. However, if some of the vacancies are attracted to impurity atoms, vacancy-solute complexes will be formed, and a proportion of the impurity atoms (those with positive vacancy-solute binding energies [64]) will be dragged with vacancies towards grain boundaries. Thus, the grain boundaries will become gradually enriched with impurity solute atoms while the vacancies are being annihilated.

In contrast to equilibrium segregation, the degree of non-equilibrium segregation depends on cooling rates and vacancy-solute binding energy. The degree of non-equilibrium segregation increases with an increase in heat treatment temperature. The cooling rate is however very critical. If cooling rate is very rapid, sufficient time may not be available for a significant diffusion of complexes to grain boundaries to occur [54]. On the other hand, if cooling rate is very slow, desegregation of solute atoms may occur, i.e., segregated solute atoms on grain boundaries may diffuse away from their grain boundary sites back to grain interior when a solute concentration gradient occurs between the grain boundaries and the grain interior [104, 135]. Therefore, the degree of non-equilibrium segregation is usually highest at intermediate cooling rates when sufficient time is available to let vacancy-solute complexes diffuse to grain boundaries but is not sufficient to let the deposited solute atoms diffuse away from the grain boundary region.

Figs. 4-19 a, b, c to 4-21 a, b, c show a set of SIMS images illustrating grain boundary distribution of boron in 718Plus after heat treatments at 950^{o}C, 1050^{o}C and

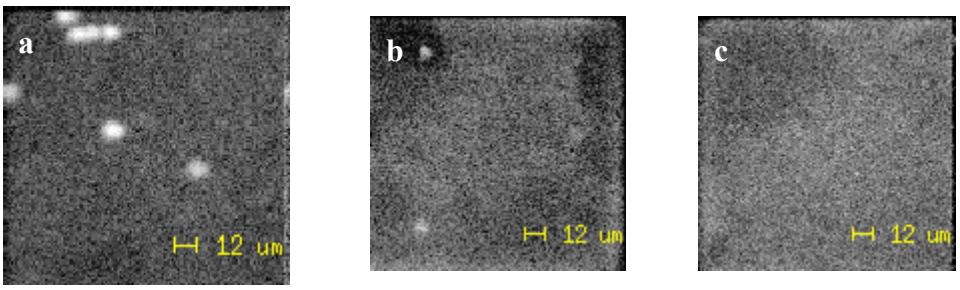

Fig. 4-19: SIMS image of boron in 718Plus after heat treatment at 950^{o}C and a) iced-water quench b) air cool c) furnace cool.

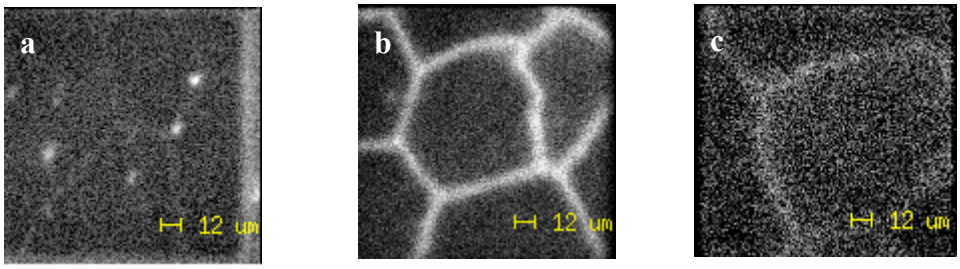

Fig. 4-20: SIMS image of boron in 718Plus after heat treatment at 1050^{o}C and a) iced-water quench b) air cool c) furnace cool.

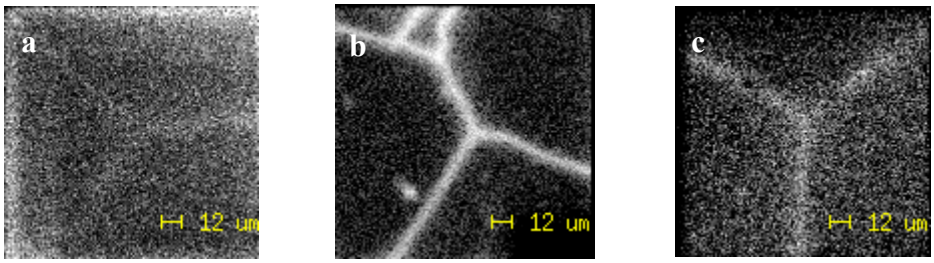

Fig. 4-21: SIMS image of boron in 718Plus after heat treatment at 1150^{o}C and a) iced-water quench b) air cool c) furnace cool.

1150^{o}C at cooling rates corresponding to iced-water quench, air cool, and furnace cool. The images were recorded at the same instrumental settings of SIMS. Within the resolution limit of SIMS, boron segregation was significantly minimized in samples heat treated at 950^{o}C, and cooled at any of the three cooling rates employed (Figs. 4-19 a, b & c). However, brighter boron signals, the degree of which varied with cooling rates and appeared to increase with heat treatment temperature, were observed in samples heat treated at 1050^{o}C and 1150^{o}C, respectively (Figs. 4-20 a, b, c to Fig. 4-21 a, b, c). The brightest boron intensity was observed in air cooled samples while iced-water quenching and furnace cooling resulted in a significant reduction in the intensity. The intensities of boron signals could not be quantified by SIMS, thus, this work is limited only to a qualitative comparison of the signals.

The dependence of non-equilibrium segregation on cooling rates suggests that the characteristically dynamic segregation pattern observed in the present work during pre-weld heat treatments of 718Plus, as shown in Figs. 4-19 to 4-21, is predominantly non-equilibrium in nature. It has been widely reported [104, 136] that the segregation of boron to grain boundaries in austenitic steels occurs mainly during cooling from high temperatures and by non-equilibrium mechanism. Karlsson et al [137] used SIMS to study the nature of grain boundary segregation of boron in type 316L austenitic stainless steel at heat treatment temperatures and cooling rates which ranged from 900^{o}C-1250^{o}C, and 530^{o}C/s – 0.25^{o}C/s, respectively. They observed an increase in the degree of grain boundary segregation of boron when the cooling rate was decreased from 530^{o}C/s to 27^{o}C/s. However, a further decrease in the cooling rate to 0.25^{o}C/s resulted in desegregation of the boron atoms, an occurrence which was marked by a decrease in the

intensity of boron atoms on the grain boundaries. In the present investigation, boron segregation was significantly minimized in 718Plus that was heat treated at 950^{o}C and cooled at various rates (Figs. 4-19 a, b, c), viz., iced-water quench (≈ 500^{o}C/s), air cool (≈ 25^{o}C/s) and furnace cool (≈ 0.25^{o}C/s). However, boron segregated to grain boundaries when the heat treatment temperature was increased to 1050^{o}C and 1150^{o}C, respectively. As shown in Figs. 4-20 a, b, c and 4-21 a, b, c, at both temperatures, the degree of segregation varied with cooling rates. The brightest boron intensities were observed in samples that were cooled at intermediate rate (air cool), while the fastest cooling rate (iced-water quench) resulted in an appreciable decrease in boron segregation. Moreover, desegregation of boron seems to have occurred during furnace cooling. A significant reduction in boron intensity was observed in furnace cooled samples, although their intensities were always brighter than that observed in the iced-water quenched samples.

Boron is considered to be the most detrimental element causing grain boundary liquation cracking in Alloy 718 [54, 64, 103], although cracking is also known to result from the constitutional liquation of MC-type carbides. Huang et al [63, 64] and Chen et al [65] evaluated the weldability of alloy 718, in both cast and wrought forms, after the alloy was pre-weld treated using various heat treatment schedules that varied the degree of boron segregation on its grain boundaries. A close relationship was observed between the pre-weld heat treatments, the degree of boron segregation and the susceptibility of 718 to HAZ cracking, which was evaluated by measuring the total length of cracks (TCL) that were observed in the HAZ. A heat treatment that increased boron segregation also increased cracking in the alloy, and vice-versa. In the present investigation no cracking was observed in weld HAZ of the alloy which was pre-weld heat treated at 950^{o}C and

cooled at various rates which ranged from iced-water quench to furnace cool (Figs. 4-15 & 4-18). SIMS analyses of the alloy in the pre-weld heat treated conditions did not reveal a significant segregation of boron to its grain boundary regions either (Fig. 4-19). Evaluation of the welds that were pre-weld heat treated at 1050^{o}C and 1150^{o}C, respectively, revealed that HAZ cracking occurred during welding (Figs. 4-17 & 4-18). The degree of cracking (TCL) in the HAZ of the welds increased with an increase in the degree of boron segregation which occurred on the grain boundaries of the alloy during the respective pre-weld heat treatments. As shown in Figs. 4-18, 4-20 & 4-21, iced-water quenching (fastest cooling rate) after pre-weld solution heat treatments at 1050^{o}C and 1150^{o}C, respectively, qualitatively resulted in the lowest degree of boron segregation and weld HAZ cracking. However, the highest degree of boron segregation and weld HAZ cracking were observed in air cooled (intermediate cooling rate) coupons. In comparison to air cooling, the degree of HAZ microfissuring was reduced in coupons which were furnace cooled; a cooling condition where desegregation of boron from grain boundaries could have started to occur and which would have reduced the amount of segregated boron on the grain boundaries.

To further confirm the contribution of boron to HAZ cracking in Allvac 718Plus, a version of the alloy which has a higher boron concentration (60 ppm of boron) was pre-weld heat treated for 1hr at 950^{o}C, 1050^{o}C and 1150^{o}C, respectively, and air cooled. Thereafter, the coupons were welded using the same electron beam welding conditions that were reported in the experimental technique section of this communication. SIMS images of segregated boron atoms on grain boundaries of the pre-weld heat treated coupons, as well as the degree of HAZ cracking which occurred during their welding are

shown in Figs. 4-22 & 4-23, respectively. Similar to the observations in the lower boron version (≈ 30 ppm) of 718Plus, boron segregation increased with an increase in pre-weld heat treatment temperature, and so did the weld HAZ cracking. However, it was noted that HAZ cracking was always higher in the higher boron version of 718Plus (Figs. 4-18 & 4-23). Also, in contrast to the lower boron version of the alloy, a more significant grain boundary segregation of boron, accompanied by weld HAZ cracking was observed in the higher boron alloy which was pre-weld heat treated at 950^{o}C. In this heat treatment condition, grain boundary segregation was significantly reduced and no HAZ cracking was observed in the lower boron version of the alloy, as shown in Figs. 4-18 and 4-19. This further confirmed that boron played a significant role in causing HAZ cracking during welding of 718Plus. Therefore, its concentration should be as low as possible to improve the weldability of the alloy.

Generally, boron has been considered to influence the susceptibility of an alloy to weld HAZ cracking by the following mechanisms:

1. Segregated boron can act as a melting point depressant and reduce the melting temperature of grain boundary regions relative to surrounding matrix [65].
2. Boron can extend the solidification range of liquid film on HAZ grain boundaries due to its low partition coefficient.
3. Boron can decrease solid-liquid interfacial energy (γ_{SL}) [64, 138], which would enhance the wettability (and facilitate spreading) and/or increase the stability of grain boundary liquid during welding.

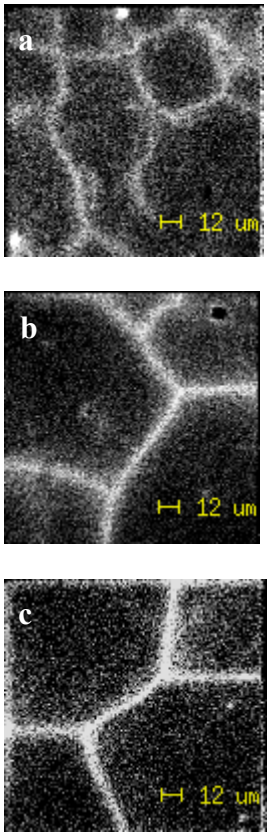

Fig. 4-22: SIMS micrographs showing grain boundary boron segregation in 718Plus (higher boron version ≈ 60 ppm) after pre-weld heat treatment at a) 950°C, b) 1050°C, and c) 1150°C. All samples were air cooled.

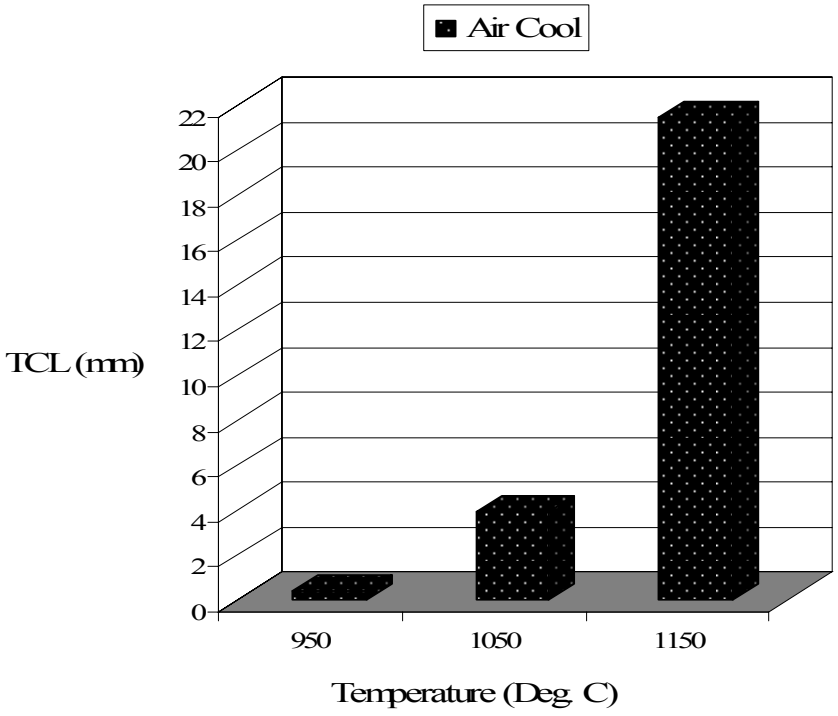

Fig. 4-23: Variation in weld HAZ total crack length (TCL) of 718Plus (higher boron version ≈ 60 ppm) with pre-weld heat treatment temperature. All samples were air cooled.

The existence of any or a combination of the above conditions, due to grain boundary boron segregation, which was observed in the present study, will increase the susceptibility of HAZ grain boundaries to liquation and facilitate spreading of the liquid film along the grain boundaries during welding. The inability of the liquated grain boundaries to support tensile stresses that develop during cooling of the welds will result in their cracking [106], as observed in the present work.

4.2.5 Effect of Pre-Weld Heat Treatments on Grain Size and Weld HAZ Cracking

In addition to boron segregation, the variation in grain size of an alloy which takes place during pre-weld heat treatments, can also affect the susceptibility of the alloy to HAZ cracking during welding. Thompson et al [139] reported that HAZ cracking of alloy 718 depends linearly on its grain size. It is common knowledge that casting components are usually more prone to cracking than their wrought counterparts. This can be partly attributed to the usually larger grain sizes of the castings, apart from contributions from their segregated microstructure. Generally, the grain size of an alloy can also contribute to its weld HAZ cracking due to the following:

1. As predicted in the non-equilibrium grain boundary segregation model of Faulkner [140], an increase in grain size could decrease total grain boundary surface area that is available for grain boundary segregation. Thus, provided heat treatment conditions are favorable for segregation to occur, an increase in the degree of boron segregation on the grain boundaries could arise, which could also increase their susceptibility to cracking during welding.

2. The grain size of an alloy can significantly influence the effectiveness of grain boundary liquid solidification by liquid film migration (LFM). This has been critically discussed in the work of Nakkalil et al [120] and will only be summarized here. Nakkalil et al [120] evaluated the occurrence of HAZ cracking in Incoloy 903 that had a duplex grain structure. A considerable amount of microfissures was observed on the grain boundaries of a large grained alloy. However, minimal cracking and an extensive occurrence of LFM were observed in the material with fine recrystallized grain boundaries. It was argued that effective relief of the supersaturation of solutes in grain boundary liquid film by LFM can reduce the total solidification range of the liquid film. This can effectively reduce the susceptibility of an alloy to HAZ cracking. The velocity of LFM is dependent on grain boundary curvature, which has been reported [141] to vary inversely with grain size. Thus, a fine grained alloy should possess a substantial mean grain boundary curvature that would enhance the solidification of grain boundary liquid film by LFM and potentially reduce the susceptibility of the alloy to HAZ cracking.
3. When the HAZ begins to accumulate strains due to welding stresses, grain boundary sliding is one mechanism that can operate to accommodate the strains [142]. However, this would increase stress concentrations at grain boundary triple points and could initiate microfissures. Once initiated, the microfissures can easily propagate along the liquated grain boundary regions. A large grain size would cause a longer interface sliding, which would lead to larger stress concentrations at grain boundary triple points [139]. This would increase the potential for crack initiation at grain boundary triple points, and therefore liquation cracking.

In wrought alloy components, a significant increase in grain size will usually increase the susceptibility of the alloy to HAZ cracking during welding. In the present investigation, the grain size of 718Plus increased significantly with an increase in pre-weld solution heat treatment temperatures ranging from 950^{o}C to 1150^{o}C (Figs. 4-13 & 4-14), and corresponding to the increase in susceptibility of the alloy to HAZ cracking (Fig. 4-18). For example, SEM observations of the welds of samples that were air cooled after pre-weld solution heat treatment at 950^{o}C (this resulted in an average grain size ≈ 58 μm) revealed an absence of HAZ cracking (Fig. 4-15). However, significant HAZ cracking, the extent of which increased with temperature, occurred when the alloy was pre-weld solution heat treated at 1050^{o}C (≈ 120 μm grain size) and 1150^{o}C (≈ 360 μm grain size), respectively.

A variation in weld HAZ cracking was also observed with cooling rates in samples that were pre-weld heat treated at 1050^{o}C and 1150^{o}C (Fig. 4-18). This variation can not be sufficiently explained with grain size considerations alone, since the grain size of the alloy did not vary appreciably with the cooling rates (Fig. 4-14). This suggests that though the size of the grains of 718Plus may have an effect on its susceptibility to HAZ cracking during welding, the cracking is however influenced by grain size and boron segregation. Therefore, it is concluded that both grain size and grain boundary segregation of boron, contributed to the observed variation in HAZ cracking of 718Plus with temperatures and cooling rates.

4.3 Post-weld Heat Treatment Microstructure and Cracking in HAZ of Allvac 718Plus

4.3.1 Introduction

As previously discussed, in developing 718Plus with an improved high temperature stability and strength compared to 718, compositional modification was carried out which resulted in a change in the main strengthening phase of the alloy from γ″ to γ′. Although nickel base alloys, such as Waspaloy, Rene 41, Inconel 738 etc, that are predominantly strengthened by γ′, and exhibit fast precipitation rate, are more stable at higher temperatures, it has been widely reported [81 – 89, 93 - 94] that they are more susceptible to HAZ cracking during post weld heat treatments. On the other hand, alloy 718, which is predominantly strengthened by the γ″ phase, has a good resistance to post weld heat treatment cracking, a property attributed to the sluggish aging response of its γ″ phase [94]. Therefore, the susceptibility of alloy 718Plus to cracking during post weld heat treatment can not be determined by a simple extrapolation of the well-known cracking behavior of its parent alloy, 718, since they are both majorly strengthened by different phases.

The present investigation was undertaken to study and understand the microstructure and cracking behavior of 718Plus during commercially recommended [7] post weld heat treatment. To achieve these objectives, electron beam welded coupons that were pre-weld solution heat treated for 1 hr at 950^{o}C and 1050^{o}C, respectively, were post weld heat treated in a furnace with an argon atmosphere. The post weld heat treatment schedule comprised of: a) stress relief solution heat treatment at 950^{o}C/1hr +AC, and b)

aging heat treatment at 788°C/ 8 hrs + furnace cool at 55°C/ hr to 654°C/ 8 hrs + air cool. Following the heat treatments, FZ and HAZ microstructures, as well as HAZ cracking of the samples were examined using optical microscopes and analytical SEM & TEM. The results of these are presented and discussed next.

4.3.2 Microstructure of Weld Fusion Zone after Standard Post-weld Heat Treatment

Fig. 4-24 shows an optical micrograph of the post weld heat treated microstructure of fusion zone of alloy 718Plus, which was pre-weld solution heat treated at 950°C/1hr +AC. The fusion zone has a cellular dendritic microstructure and it showed no evidence of cracking. Also, similar microstructure was observed in post weld heat treated samples which were pre-weld heat treated at 1050°C/1hr +AC. Typical higher magnification SEM secondary electron (SE) and backscattered electron (BSE) microstructural images of the fusion zones of the post weld heat treated samples are shown in Figs. 4-25 a and b, respectively. As seen in Fig. 4-25 a, the interdendritic region of the fusion zone consisted of blocky shaped second phase particles within needle-like particles, which are distributed in an almost continuous fashion. The contrast between the phases was better revealed under backscattered electron image shown in Fig. 4-25 b. Preliminary SEM/EDS analysis of the interdendritic blocky shaped particles suggested them to be based on MC type carbides and Laves phase, however, TEM was used for their positive identification. The characteristic needle-shaped morphology of the particles associated with the blocky shaped phase(s) suggested them to be δ phase, which is commonly observed in 718-type alloys after exposure to high temperature below δ solvus, usually around 1020°C [20, 25]. In addition, careful SEM examination under

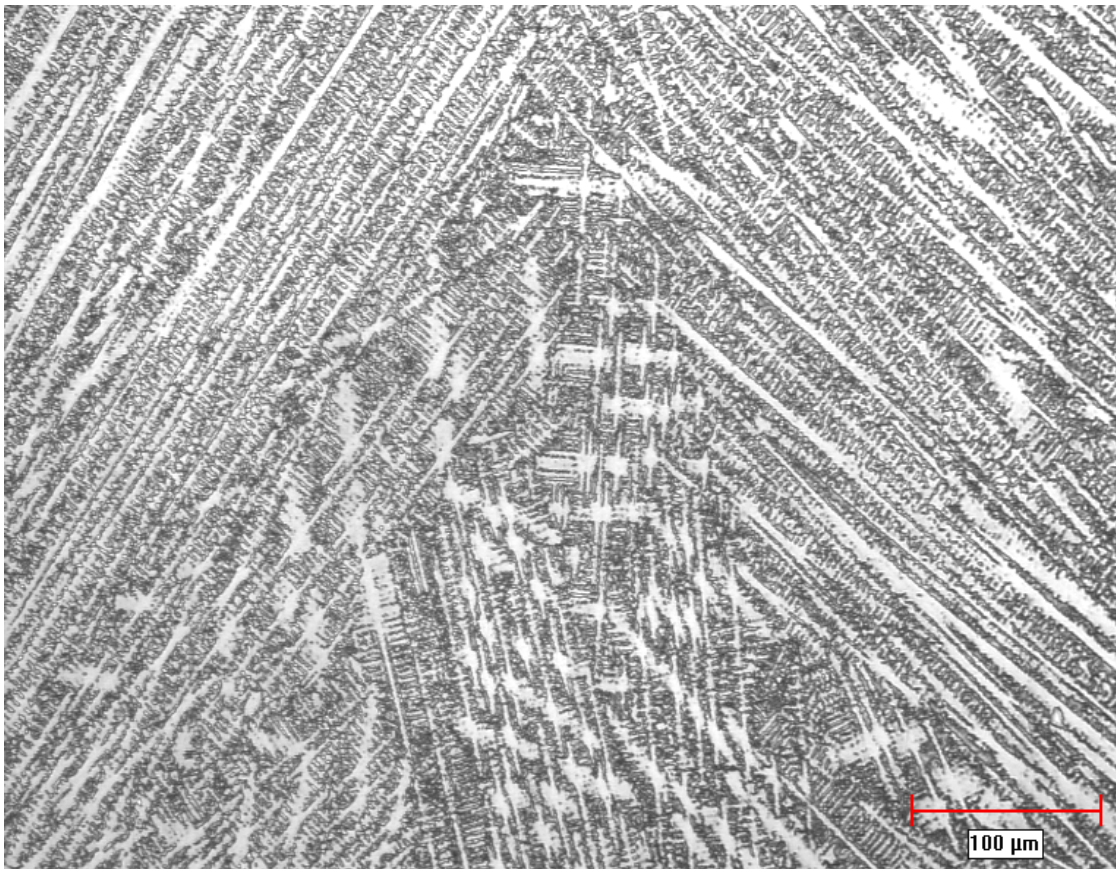

Fig. 4-24: Optical micrograph showing cellular-dendritic microstructure of weld fusion zone of 718Plus following pre-weld solution heat treatment (SHT) at 950^{o}C/1hr +AC, and post-weld heat treatments comprising of a) SHT at 950^{o}C/1hr +AC, and b) aging heat treatment at 788^{o}C/ 8 hrs + furnace cool to 654^{o}C/ 8 hrs + air cool.

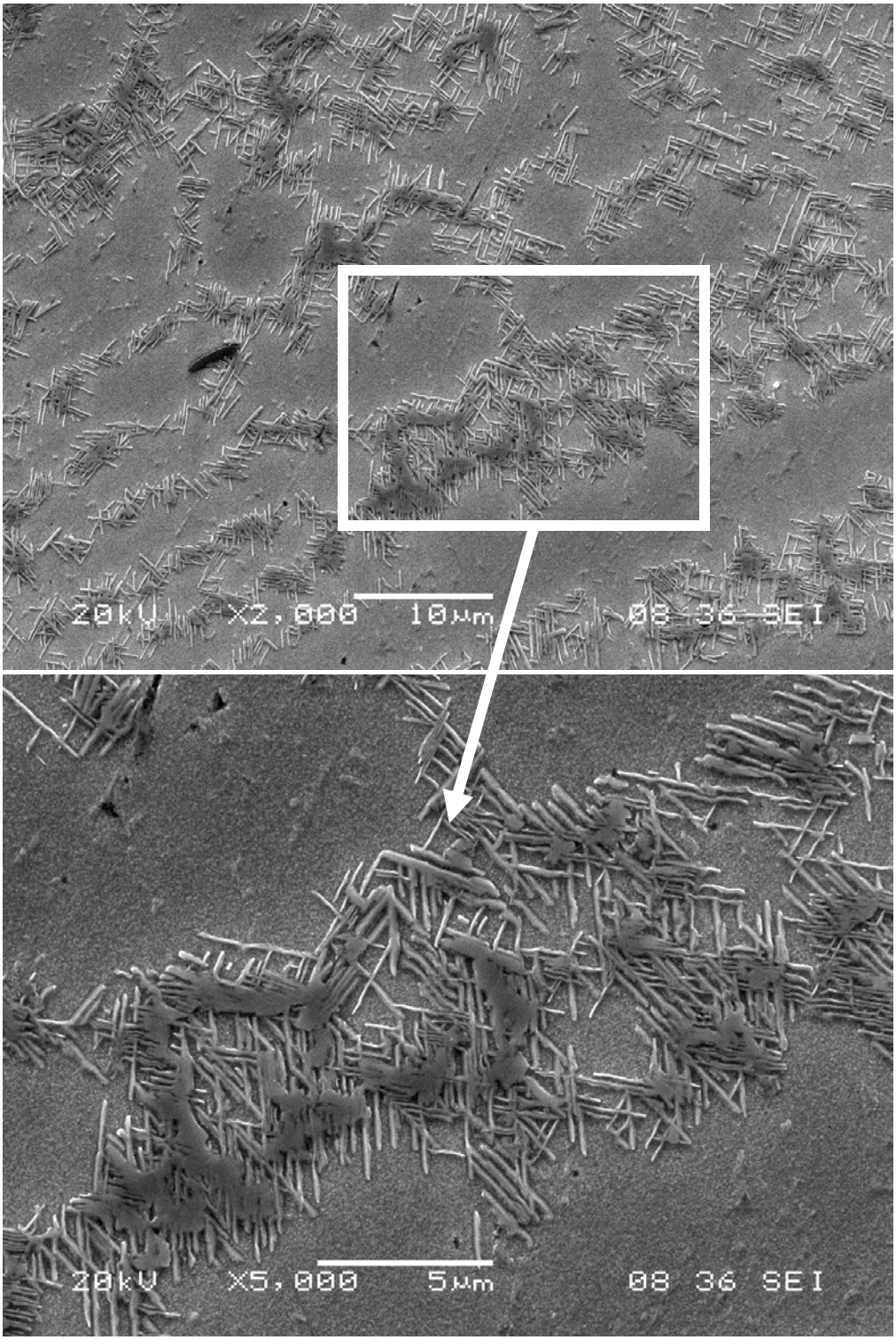

Fig. 4-25a: SEM secondary electron image of weld fusion zone microstructure of 718Plus following pre-weld solution heat treatment (SHT) at 950^{o}C/1hr +AC, and post-weld heat treatments comprising of a) SHT at 950^{o}C/1hr +AC, and b) aging heat treatment at 788^{o}C/ 8 hrs + furnace cool to 654^{o}C/ 8 hrs + AC.

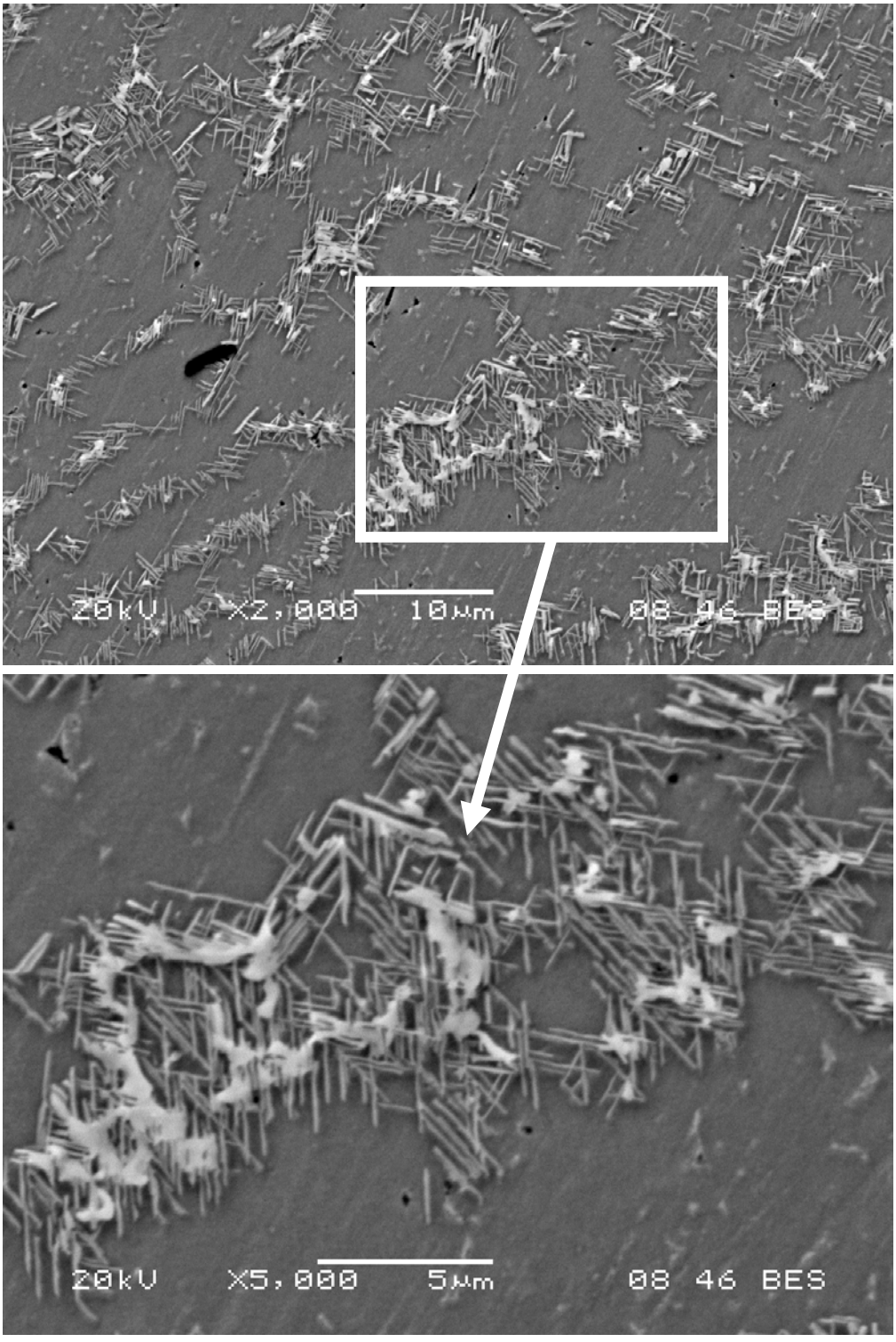

Fig. 4-25b: SEM backscattered electron image of weld fusion zone microstructure of 718Plus following pre-weld solution heat treatment (SHT) at 950°C/1hr +AC, and post-weld heat treatments comprising of a) SHT at 950°C/1hr +AC, and b) aging heat treatment at 788°C/ 8 hrs + furnace cool to 654°C/ 8 hrs + AC.

secondary electron mode at higher magnification, as shown in Fig. 4-25 a, revealed variation in light etching contrasts within the bulk fusion zone. This could be due to precipitation of closely spaced fine γ′ precipitates which could not be resolved appropriately by SEM. Thus, this was further investigated using TEM.

A typical TEM bright field image of the phase constituents in the post-weld heat treated fusion zone is shown in Fig. 4-26. Apart from the matrix (M), three other phases, labeled C, L & D, were identified. The TEM-EDS spectra of the phases (C, L & D) and matrix (M) are shown in Figs. 4-27 a, b, c & d, while their semi-quantitative chemical compositions are summarized in Table 4-4. The TEM compositional analyses suggested the phases C, L & D to be MC-type carbide, Laves, and delta, respectively. These were confirmed by TEM selected area diffraction pattern (SADP) analysis.

Figs. 4-28 a & b show SADPs of crystals of phase C oriented at $[\bar{1}12]$ and $[\bar{1}14]$ zone axes parallel to the electron beam. Analyses of the SADPs indicated the crystal structure of the phase to be face centered cubic (fcc) with lattice parameter a = 4.47 Å (0.447 nm), which is similar to that of MC-type carbides [15]. Combination of the SADPs and TEM/EDS analyses (Fig. 4-27 a, Table 4-4) confirmed phase C to be an Nb, Ti – rich carbide. Furthermore, analysis of SADPs, one of which was obtained from $[01\bar{1}2]$ zone axis parallel to the beam and is shown in Fig. 4-29, and the TEM/EDS analysis (Fig. 4-27 b, Table 4-4) confirmed phase L to be Laves phase with a hexagonal closed pack crystal structure with lattice parameters a = 4.90 Å (0.49 nm), b = 8.0 Å (0.80 nm).

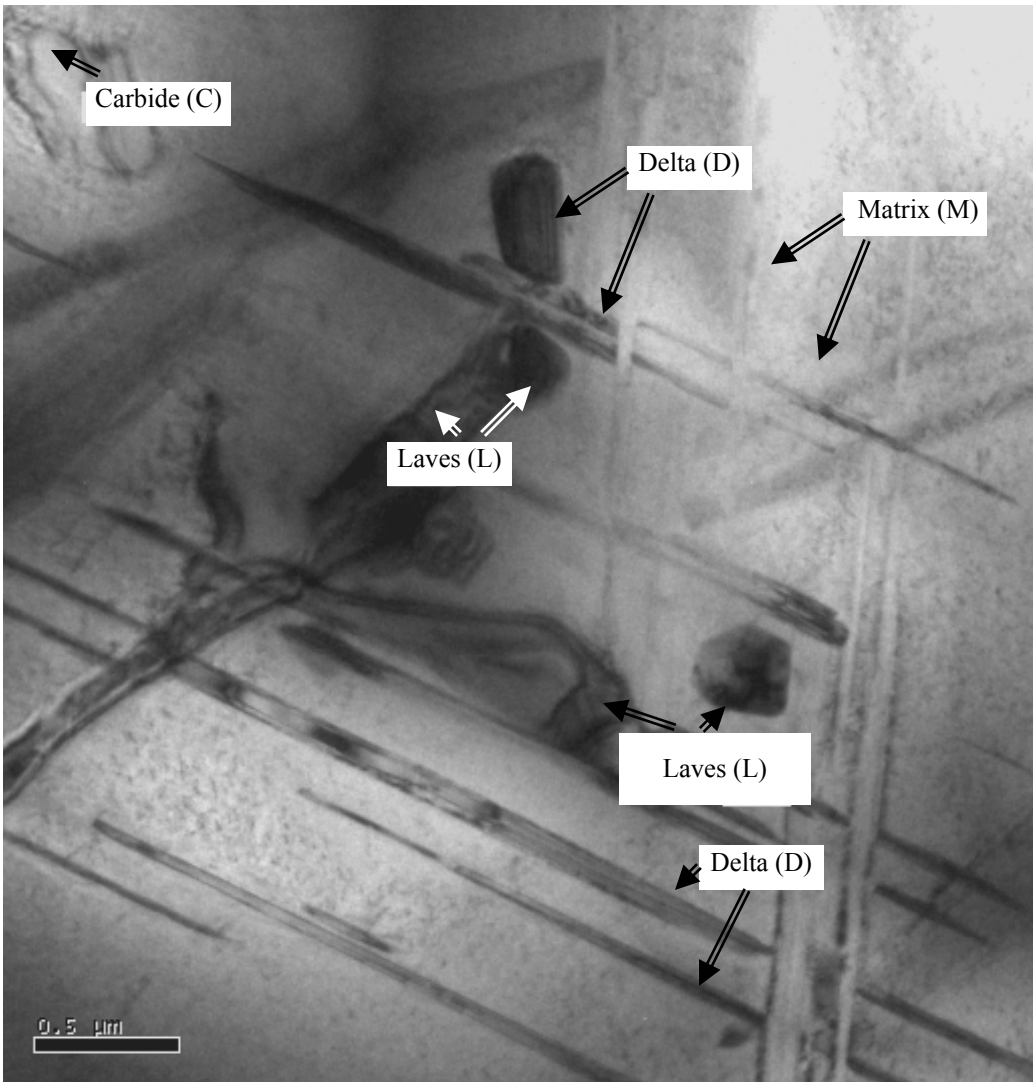

Fig. 4-26: TEM bright field image of fusion zone constituents of post-weld heat treated 718Plus, showing carbide (C), matrix (M), Laves (L) and delta (D) phases.

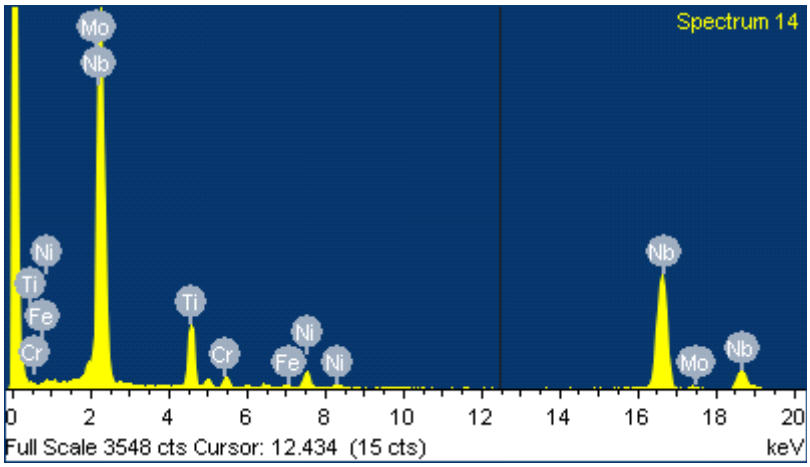

(a)

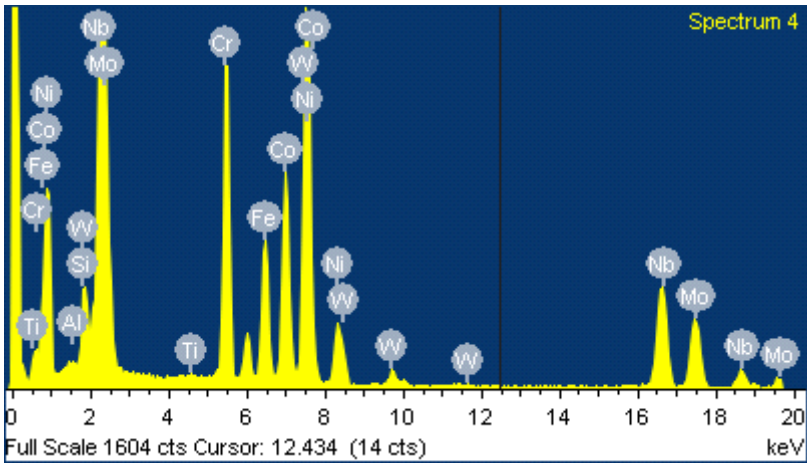

(b)

Fig. 4-27: TEM/ EDS spectrum of a) MC-type carbide, b) Laves constituents in the fusion zone of post-weld heat treated 718Plus.

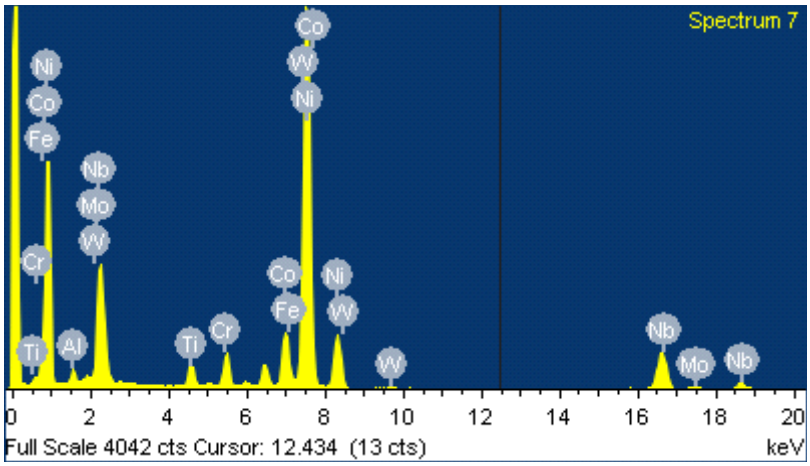

(c)

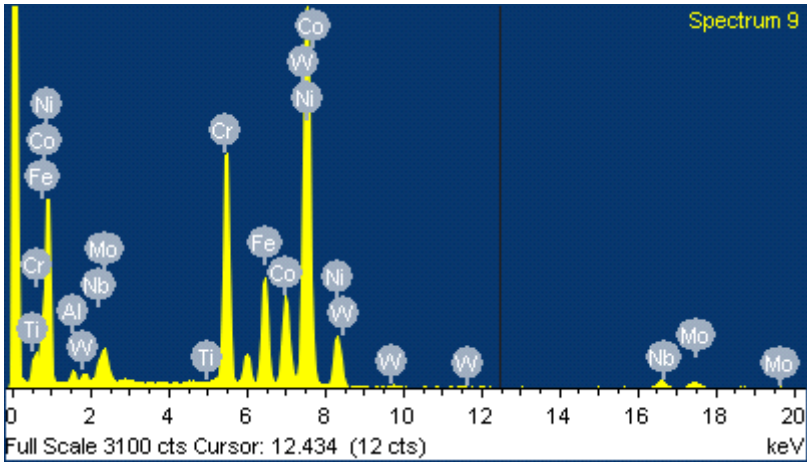

(d)

Fig. 4-27: TEM/ EDS spectrum of c) delta phase, d) matrix in the fusion zone of post-weld heat treated 718Plus.

Table 4-4: Semi-quantitative TEM/EDS Analysis (wt % and at %) of fusion zone constituents of post-weld heat treated alloy 718Plus.

	Carbide –MC type (C)		Laves (L)		Delta (D)		Matrix (M)	
	wt %	at %	wt %	at %	wt %	at %	wt %	at %
Ni	5.42	7.40	31.84	34.57	69.43	71.91	53.42	52.45
Cr	2.49	3.83	16.09	19.73	3.49	4.08	19.76	21.90
Fe	0.88	1.27	8.88	10.13	2.92	3.18	11.28	11.65
Co	-	-	15.27	16.51	8.57	8.84	10.94	10.70
Nb	78.22	67.40	13.80	9.46	12.45	8.15	1.63	1.01
Mo	1.91	1.59	11.81	7.84	0.79	0.50	2.14	1.28
Al	-	-	0.03	0.06	0.47	1.05	0.35	0.76
W	-	-	1.76	0.61	0.12	0.04	0.36	0.11
Ti	11.08	18.51	0.11	0.15	1.78	2.26	0.12	0.14
Si	-	-	0.41	0.93	-	-	-	-

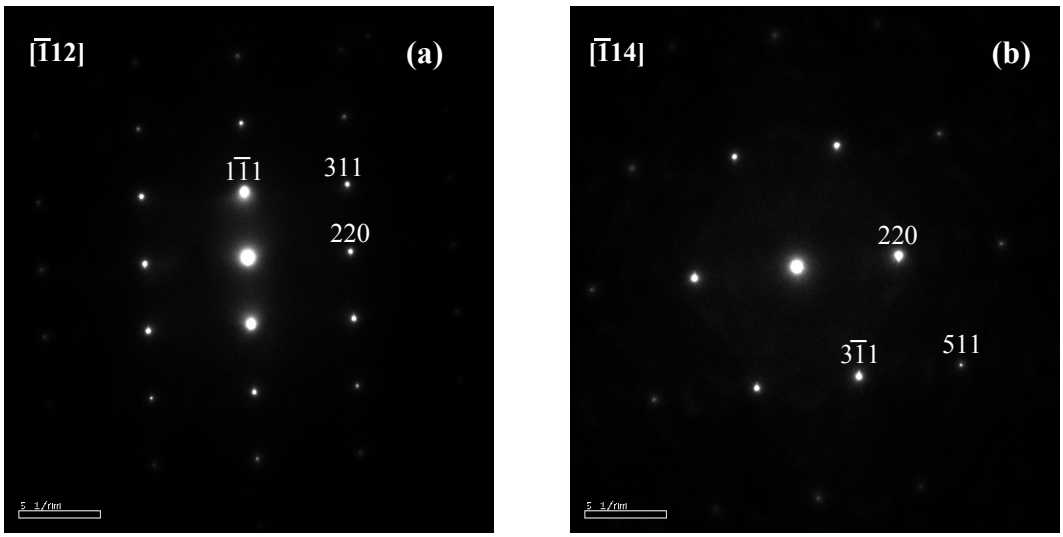

Fig. 4-28: TEM SADPs from a) [$\bar{1}$12], and b) [$\bar{1}$14] zone axes of a MC-type carbide particle (C) in the fusion zone of post-weld heat treated 718Plus.

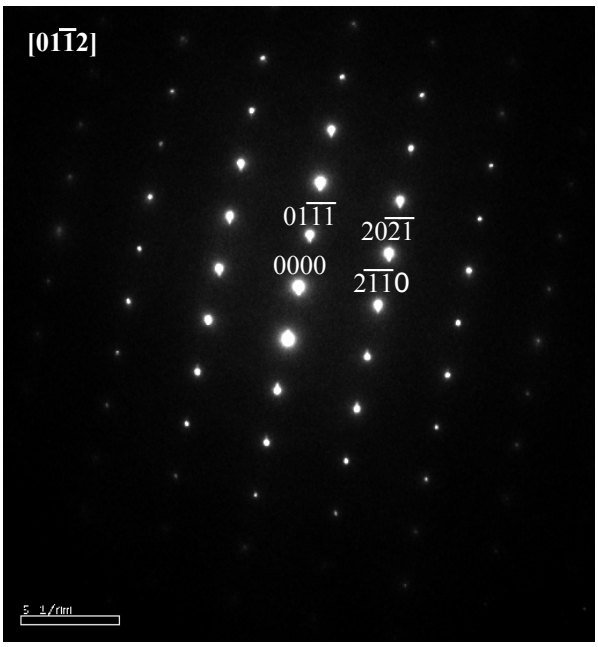

Fig. 4-29: TEM SADP from [01$\bar{1}$2] zone axis of a Laves particle (L) in the fusion zone of post-weld heat treated 718Plus.

In addition to the Nb, Ti-rich carbides and Laves phase, analysis of SADPs from phase D, an example of which is shown in Fig. 4-30, confirmed the phase to be delta phase with an orthorhombic crystal structure and lattice parameters a = 5.11 Å (0.511 nm), b = 4.25 Å (0.425 nm), c = 4.55 Å (0.455 nm). TEM SADPs obtained from γ matrix (phase M) of the post-weld heat treated fusion zone, revealed the presence of superlattice reflections typical to those of $L1_2$ ordered lattice of γ′ precipitates (Fig. 4-31 a). A dark field image (Fig. 4-31 b) was obtained using (010) superlattice reflection, and it revealed the presence of spherical γ′ precipitates with an ordered fcc crystal structure and lattice parameter a = 3.64 Å (0.364 nm). The average size of the γ′ precipitates is about 0.03 μm (30 nm), so they could not be resolved by SEM (Fig. 4-25 a). TEM SADP (Fig. 4-32) obtained from γ solid solution matrix of fusion zone in the as-welded condition, however, did not reveal presence of γ′ superlattice reflections. Thus, the γ′ observed in the post-weld heat treated fusion zone formed during the post-weld heat treatment, which was carried out within precipitation temperature range of γ′ phase.

In the as-welded condition, the fusion zone of alloy 718Plus consisted of γ dendrites and microsegregation-induced secondary solidification constituents comprising of MC- type carbides and interdendritic Laves phase (Fig. 4-33). The solvus temperatures [25] of the carbide and Laves phases are higher than the post-weld heat treatment temperature range employed for alloy 718Plus, thus, the phases persisted, and were observed in the post-weld heat treated specimens (Figs. 4-25 & 4-26). However, the delta and γ′ phases, which were not present in as-welded condition, formed during the post-weld heat treatment. The presence of γ′ phase in age-hardenable Ni-base alloys is known

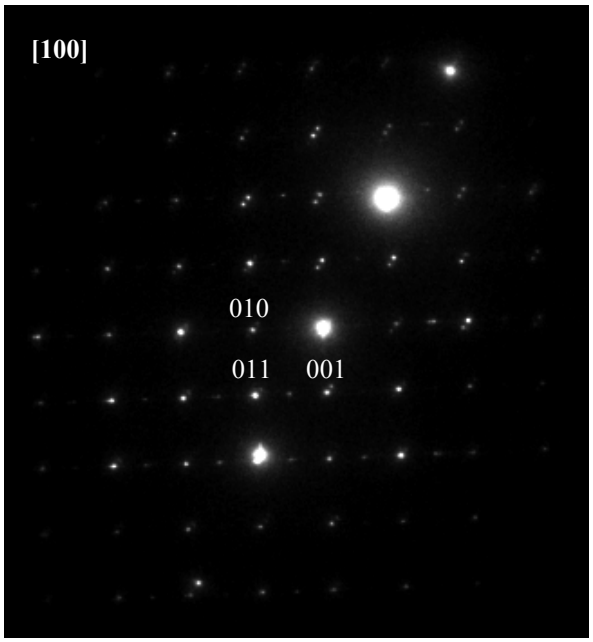

Fig. 4-30: TEM SADP from [100] zone axis of delta phase particle (D) in the fusion zone of post-weld heat treated 718Plus.

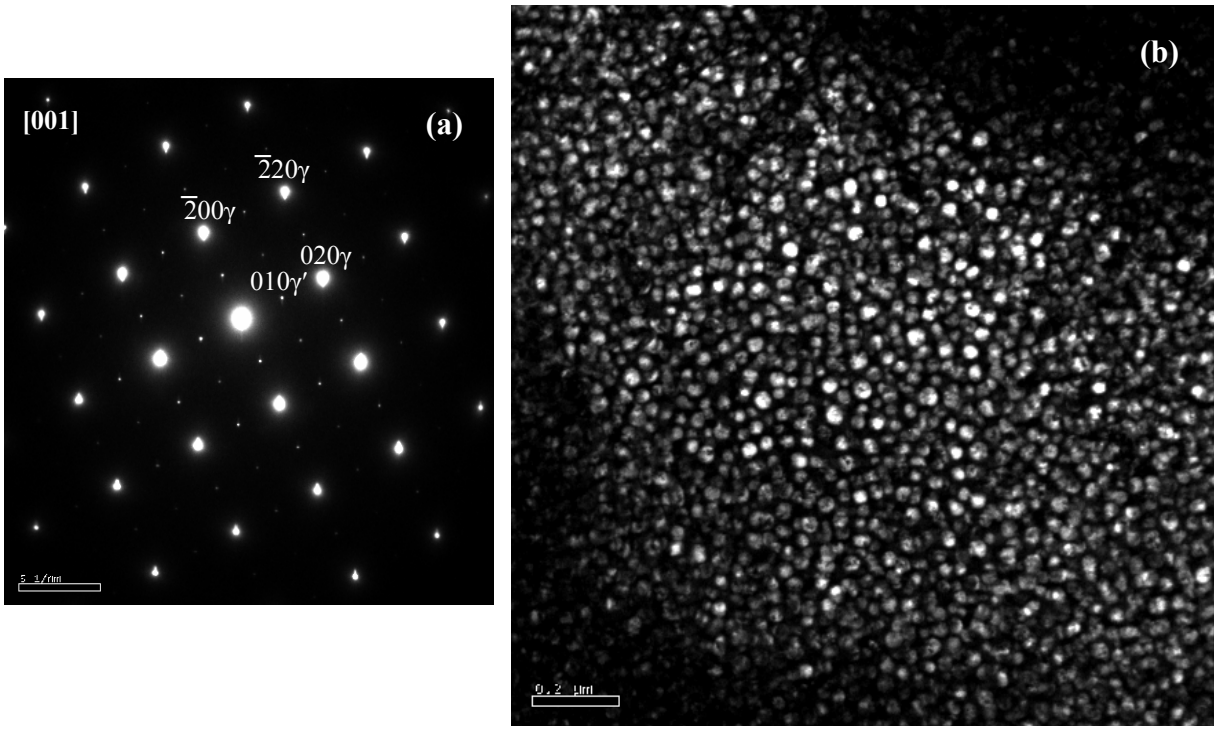

Fig. 4-31: TEM a) SADP from [001] zone axis of γ matrix (M) showing the presence of superlattice reflections typical to $L1_2$ ordered lattice of γ′ phase, b) dark field image of γ′ particles taken with (010) superlattice reflection in the fusion zone of post-weld heat treated 718Plus.

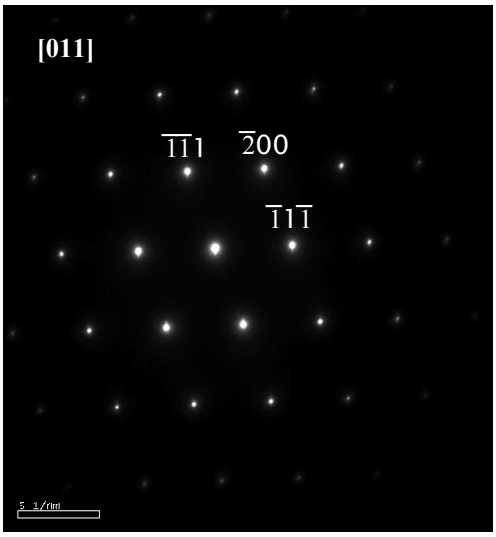

Fig. 4-32: TEM SADP from [011] zone axis of γ matrix showing the absence of superlattice reflections of γ′ phase in the as-weld fusion zone of 718Plus.

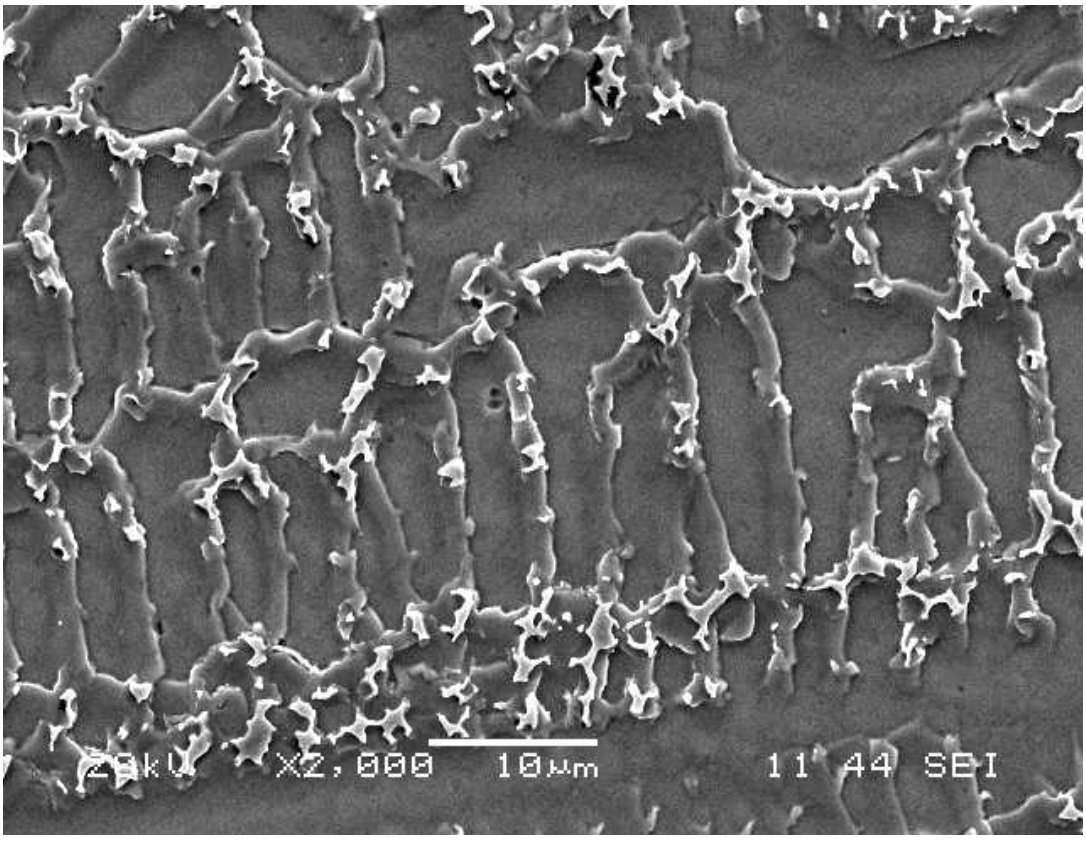

Fig. 4-33: SEM secondary electron image of the as-weld fusion zone of an electron beam welded 718Plus.

to significantly contribute to their high temperature strength. Thus, the precipitation of γ′ from γ matrix in the weld fusion zone of alloy 718Plus during post-weld heat treatment is beneficial for its mechanical properties. On the other hand, δ phase is incoherent with γ matrix and does not confer substantial strength when present in significant quantity [15], as observed at the interdendritic regions in the present work (Figs. 4-25 a & b).

In summary, a composite microstructure, comprising of γ′, γ matrix, MC-type carbides, Laves and δ phases, was observed in the fusion zone of standard post-weld heat treated alloy 718Plus. Some of the secondary phases, e.g. γ′, and MC-type carbides, could improve the mechanical properties of the fusion zone, while others, e.g., Laves and δ phases, could degrade the properties and produce weld fusion zone with inferior mechanical properties. Thus, to improve the mechanical properties of as-welded fusion zone of 718Plus, it is required that the post-weld heat treatment be designed such that it completely dissolves Laves phase and minimize δ phase precipitation while optimizing the precipitation of γ′ phase.

4.3.3 Weld HAZ Microstructure and Cracking during Standard Post-Weld Heat Treatment of Allvac 718Plus.

To study post-weld HAZ microstructure and cracking in alloy 718Plus, as welded coupons of the alloy, which were pre-weld solution heat treated at 950^{o}C/1hr +AC and 1050^{o}C/1hr +AC, respectively, were post-weld heat treated using standard heat treatment.

Figs. 4-34 & 4-35 show optical micrographs of HAZ regions of as-welded coupons that were pre-weld solution heat treated at 950^{o}C/1hr +AC and 1050^{o}C/1hr +AC, respectively. It is seen that the HAZ of the 950^{o}C/1hr coupons were crack-free (Fig. 4-34), while cracks were observed in the HAZ of coupons pre-weld heat treated at 1050^{o}C/1hr +AC (Fig. 4-35). Higher magnification SEM micrographs of the HAZs of the two pre-weld heat treatment conditions are presented in Figs. 4-36 & 4-37. HAZ cracks in about 8 cross-sections of the 1050^{o}C/1hr +AC welded coupons were quantified by using SEM image analysis software. The total crack length (TCL), average total crack length (ATCL/S), total number of cracks (TNC), average length of a crack (ACL), and maximum crack length (MCL) were determined and is presented in Table 4-5. Apart from the presence or absence of HAZ cracking in the welds, intergranular and intragranular MC-type carbides, some of which had constitutionally liquated, were observed in the HAZs. Also, some of the HAZ grain boundaries were laced with resolidified γ/Laves eutectic-like constituents, as shown in Fig. 4-38. Further SEM examination did not reveal the presence of γ′ precipitates, both in the HAZ and base metal region of the welds.

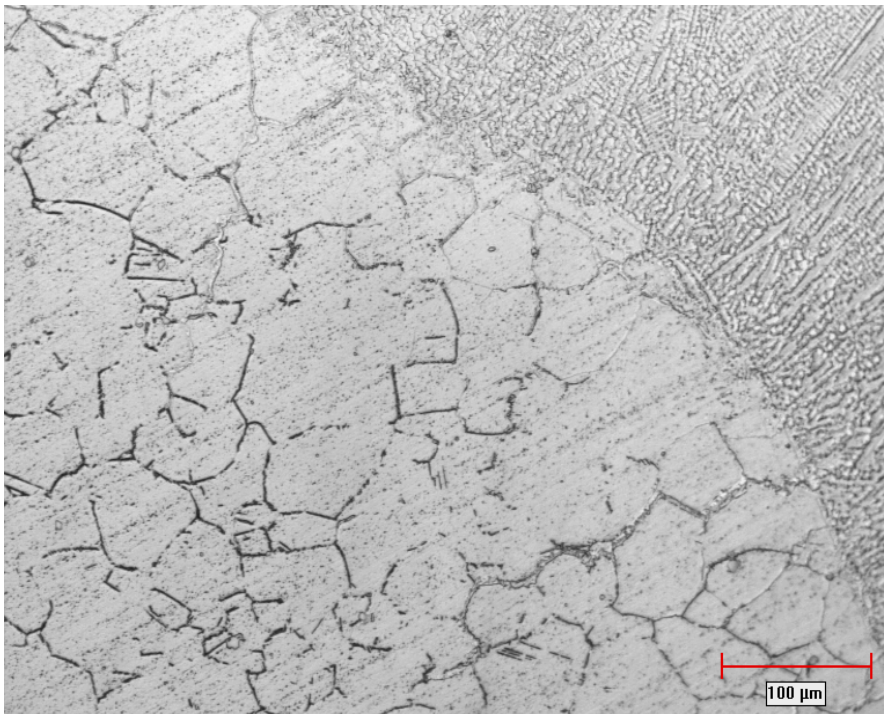

Fig. 4-34: Optical micrograph of as-weld HAZ of 718Plus which was pre-weld solution heat treated at 950°C/1hr +AC, showing absence of HAZ cracks.

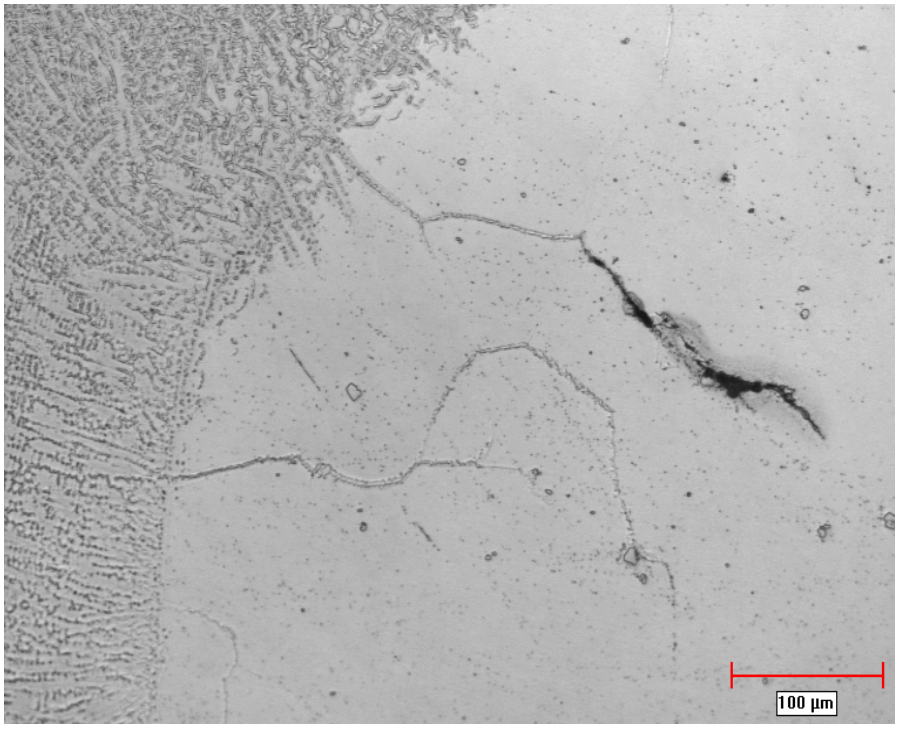

Fig. 4-35: Optical micrograph of as-weld HAZ of 718Plus which was pre-weld solution heat treated at 1050°C/1hr +AC, showing presence of HAZ crack.

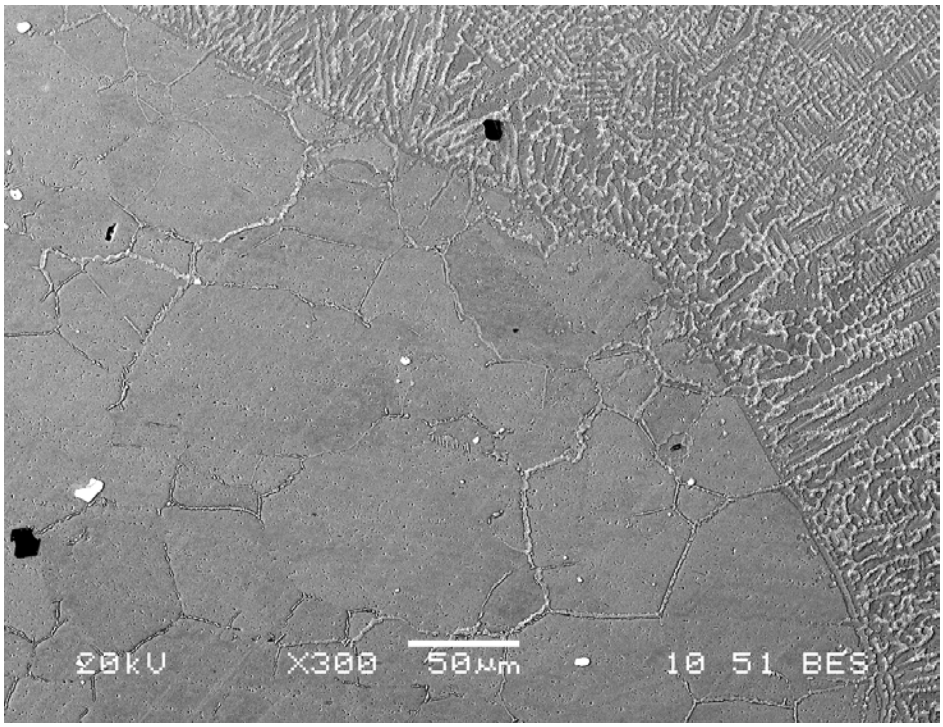

Fig. 4-36: SEM backscattered electron image of as-weld HAZ of 718Plus, which was pre-weld solution heat treated at 950°C/1hr +AC, showing absence of HAZ cracks.

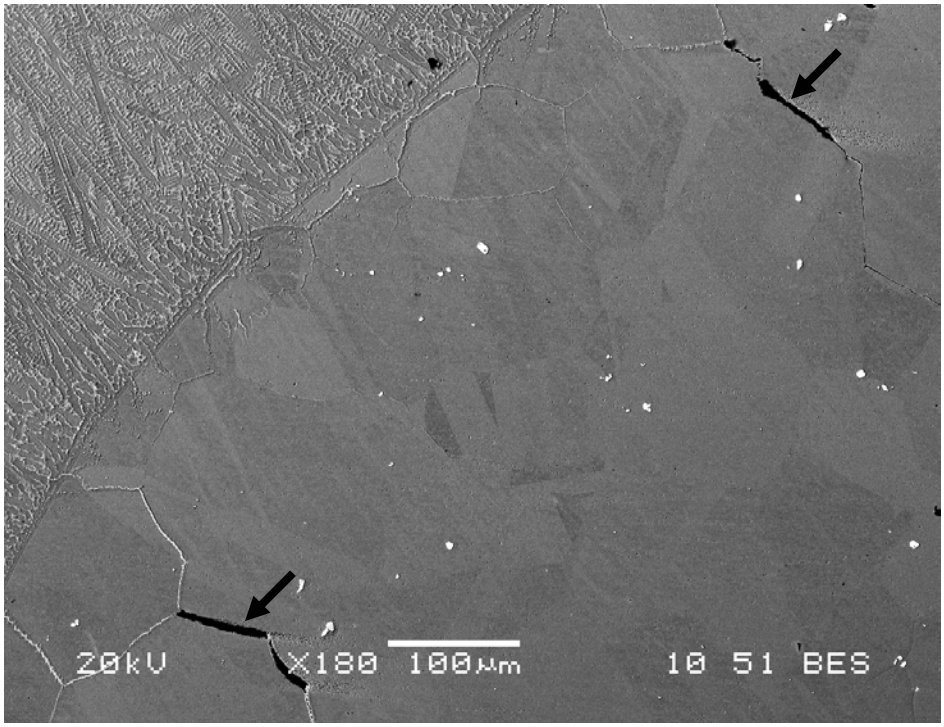

Fig. 4-37: SEM backscattered electron image of as-weld HAZ of 718Plus, which was pre-weld solution heat treated at 1050°C/1hr +AC, showing presence of HAZ cracks (marked with arrow heads).

Table 4-5: HAZ cracking susceptibility of 718Plus during electron beam welding and post-weld heat treatment. Weld coupons were pre-weld solution heat treated at 950°C/1hr +AC (coupon A) and 1050°C/1hr +AC (coupon B), respectively.

	As welded coupon A* 950°C/1hr + AC	Post-weld# heat treated coupon A	As-welded coupon B+ 1050°C/1hr + AC	Post-weld# heat treated coupon B
Total Crack Length – TCL (μm)	0	1705	2572	8247
Average Total Crack Length per Section – ATCL/S (μm)	0	213	321	1030
Total Number of Cracks -TNC (μm)	0	26	28	81
Average Length of a Crack – ALC (μm)	0	65	91	101
Maximum Crack Length – MCL (μm)	0	240	259	312

*coupon A: 718Plus solution heat treated at 950°C/1hr +AC before welding

#: post-weld heat treated using standard heat treatment schedule comprising of a) solution heat treatment at 950°C/1hr +AC, and b) aging heat treatment at 788°C/ 8 hrs + furnace cool to 654°C/ 8 hrs + air cool.

+coupon B: 718Plus solution heat treated at 1050°C/1hr +AC before welding

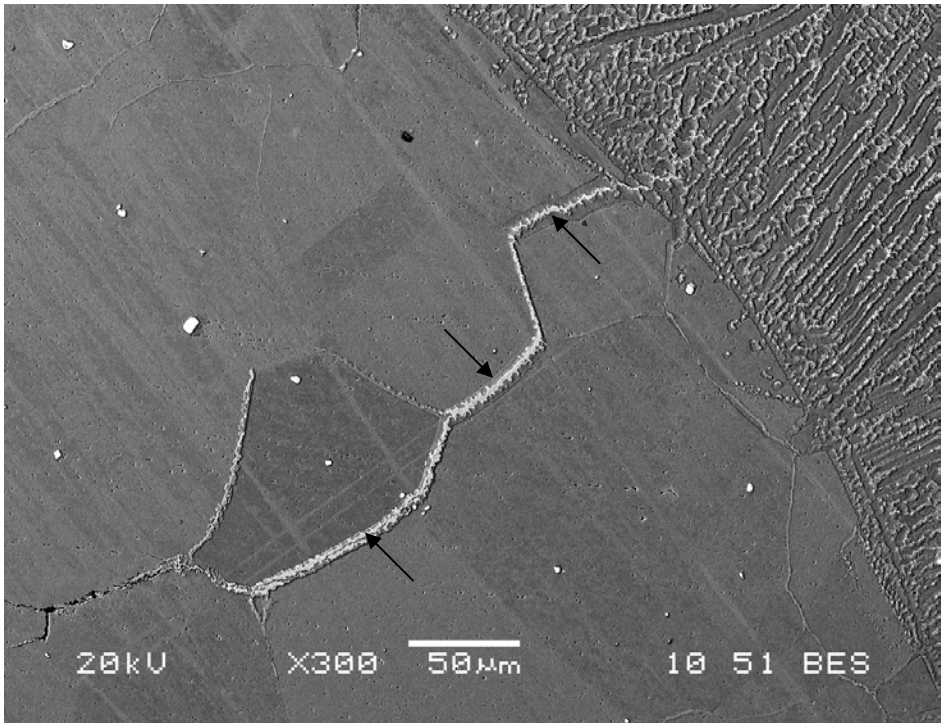

Fig. 4-38: SEM backscattered electron image of as-weld HAZ of 718Plus, which was pre-weld solution heat treated at 1050°C/1hr +AC, showing grain boundary outlined by γ/Laves eutectic-like phase (marked with arrow heads).

To further confirm the absence of γ′, TEM selected area diffraction patterns were taken from matrix in the weld HAZ and base metal regions of coupons that were pre-weld solution heat treated at 950°C/1hr +AC. Figs. 4-39 a & b show typical SADPs from the HAZ and base metal, respectively. It is seen that superlattice reflections from γ′ were absent from the SADPs. This confirms that γ′ precipitates did not form in the HAZ and base metal region of the as-welded coupons.

As-welded coupons (coupon A: pre-weld solution heat treated at 950°C/1hr +AC; coupon B: pre-weld solution heat treated at 1050°C/1hr +AC) were post-weld heat treated using standard heat treatment schedule of 950°C/1hr +AC post-weld solution heat treatment, and aging at 788°C/ 8 hrs + furnace cool to 654°C/ 8 hrs + air cool. Following the post-weld heat treatment, HAZs of the coupons were examined using SEM to determine if post-weld heat treatment cracking had occurred, and also to study the microstructure of the region. Figs. 4-40 a & b show SEM backscattered electron images of the HAZ of coupon A after post-weld heat treatment. As seen in the figures, cracks were observed along some grain boundaries in the post-weld heat treated HAZ, which was initially crack-free. Higher magnification SEM image of the crack, shown in Fig. 4-41, revealed that they are outlined on both crack interfaces by a dense network of Laves phase and acicular δ precipitates. It was noted that the cracks were usually fine and most easily identified in backscattered electron imaging mode of SEM. Cracking extent during the post-weld heat treatment was quantified by measuring TCL, ATCL/S, TNC, ALC, and MCL. Results of the measurements are presented in Table 4-5.

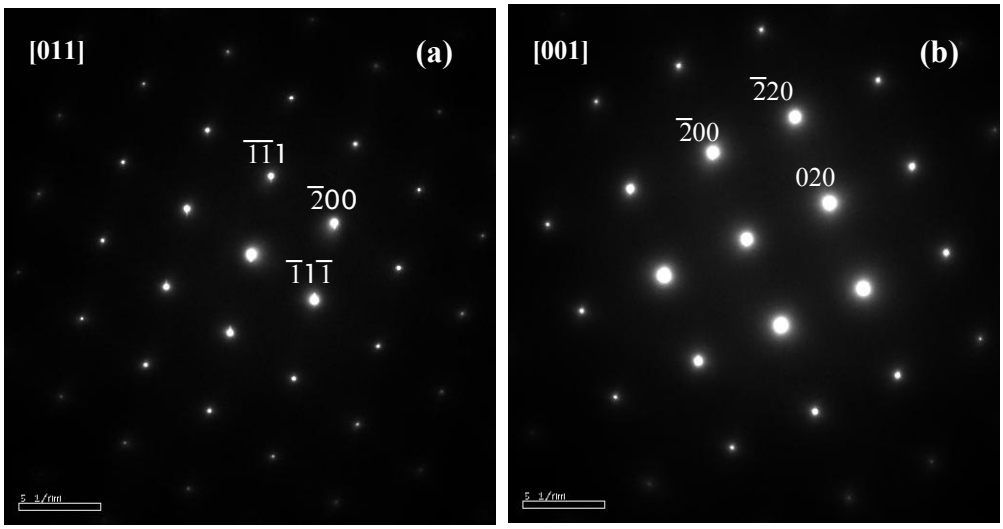

Fig. 4-39: TEM SADP from a) [011] zone axis of γ matrix from HAZ, b) [001] zone axis of γ matrix from base metal region, showing the absence of superlattice reflections of γ′ phase in as-welded 718Plus which was pre-weld heat treated at 950^{o}C/1hr +AC.

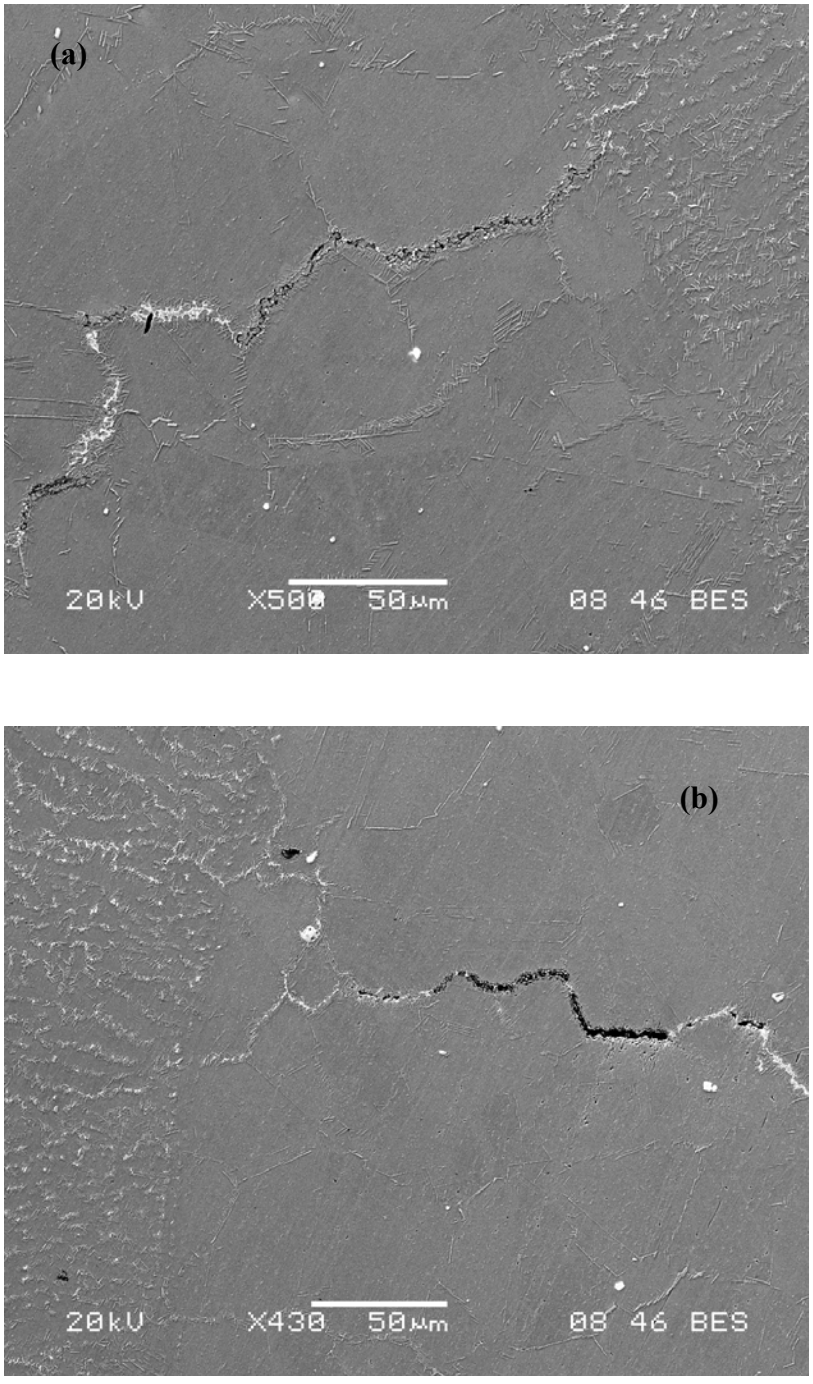

Figs. 4-40 a & b: SEM backscattered electron images showing presence of HAZ cracks in 718Plus after post-weld heat treatment. Coupon was pre-weld solution heat treated at 950^{o}C/1hr +AC.

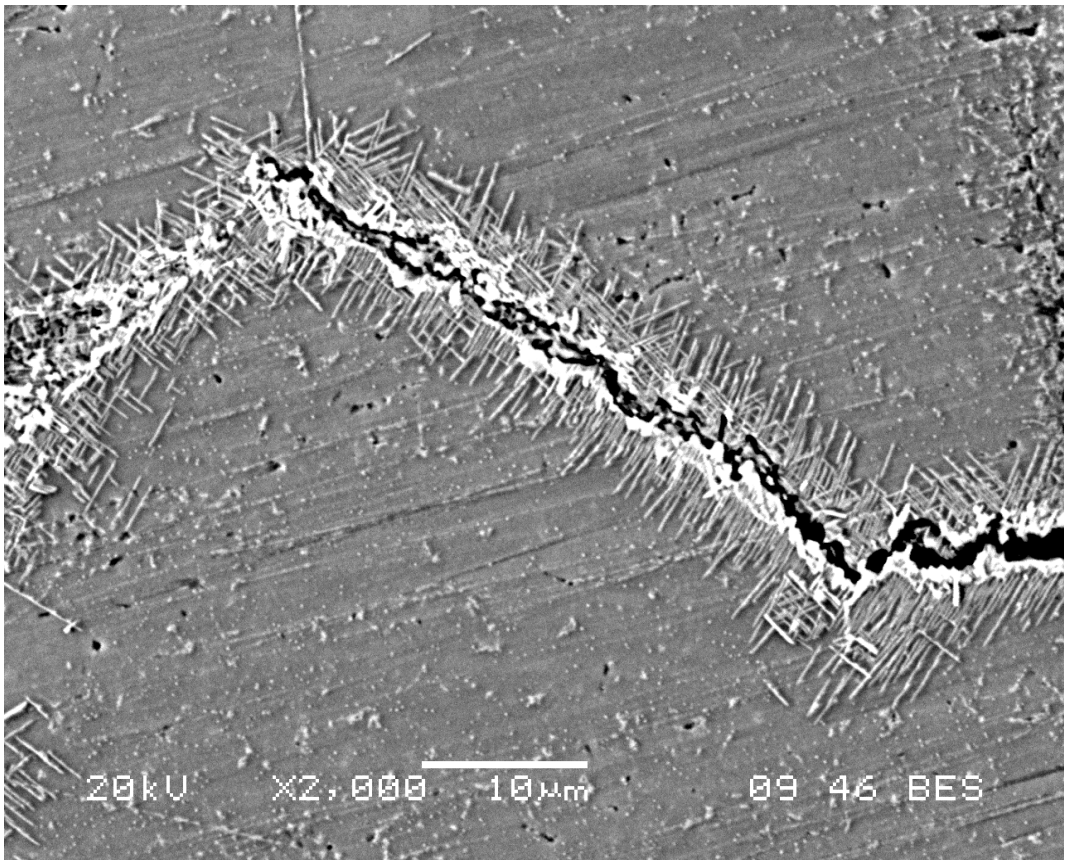

Figs. 4-41: Higher magnification SEM backscattered electron image of a post-weld heat treatment crack in HAZ of 718Plus. Note dense network of Laves phase and acicular δ precipitate outlining the crack.

SEM examination of the HAZ of post-weld heat treated coupon B, an example of which is shown in Fig. 4-42, revealed a more extensive degree of cracking than was observed in post-weld heat treated coupon A. Two different types of cracks were observed, namely; finer cracks (Fig. 4-43 a) that were laced with dense network of Laves and δ phases similar to those observed in coupon A (Figs. 4-40 & 4-41), while the other cracks were relatively wider with almost no second phase precipitates at the crack interfaces (Fig. 4-43 b). The extent of cracking in the coupon was quantified, and is summarized in Table 4-5. It is seen from the table that there is a higher degree of cracking, measured in terms of TCL, ATCL/S, TNC, ALC and MCL, in coupon B compared to coupon A. This may be attributed to the fact that in contrast to coupon A, which was crack-free before post-weld heat treatment, coupon B contained some HAZ cracks which formed during welding and might have further propagated during post-weld heat treatment.

In addition to the cracks and dense network of phases which were observed on HAZ grain boundaries of coupons A and B (Figs. 4-40 to 4-43), SEM examination of grain interiors within the HAZ revealed the presence of a significant volume fraction of γ′ precipitates. This was also observed in the base metal regions of the coupons. Also, MC-type carbides and δ precipitates were observed in the HAZ grain interiors. A typical higher magnification SEM secondary electron image of the phases (γ′, MC-type carbide & δ phase) within the HAZ grain interior is shown in Fig. 4-44. TEM dark field image of the γ′ particles is shown in Fig. 4-45. The γ′ particles have an average size of 0.04 μm, but occasionally larger γ′ particles measuring 0.1 – 0.2 μm were also observed.

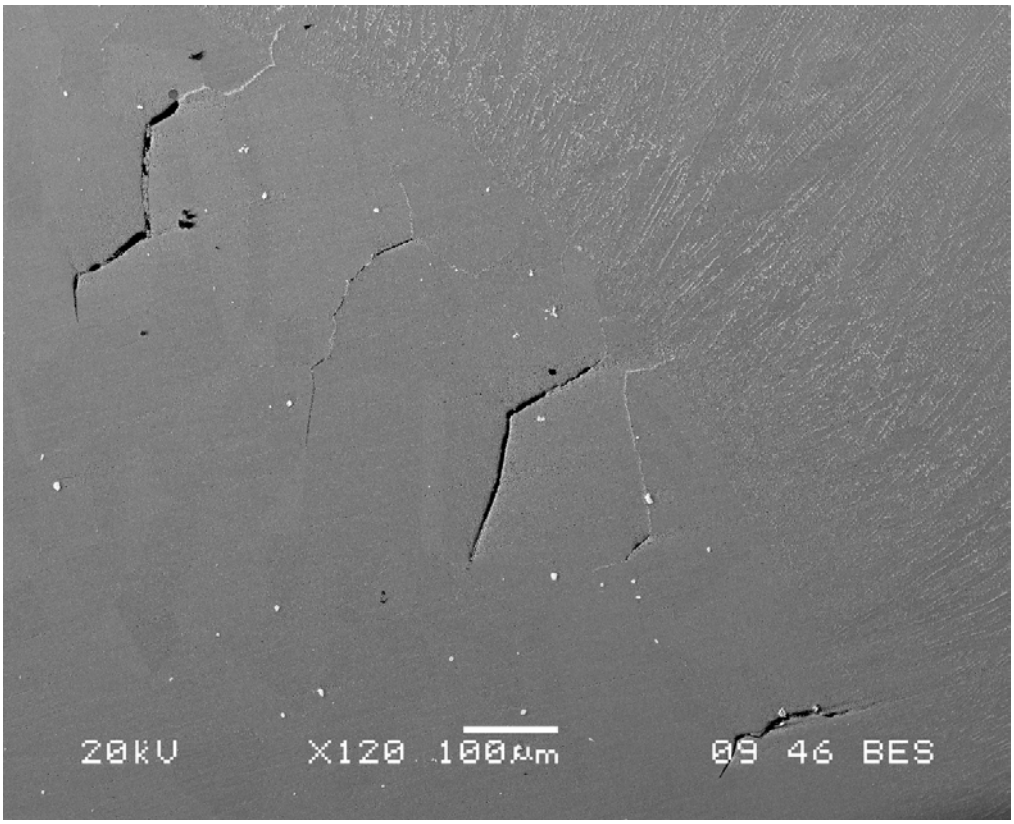

Figs. 4-42: SEM backscattered electron image showing presence of HAZ cracks in 718Plus after post-weld heat treatment. Coupon was pre-weld solution heat treated at 1050^{o}C/1hr +AC.

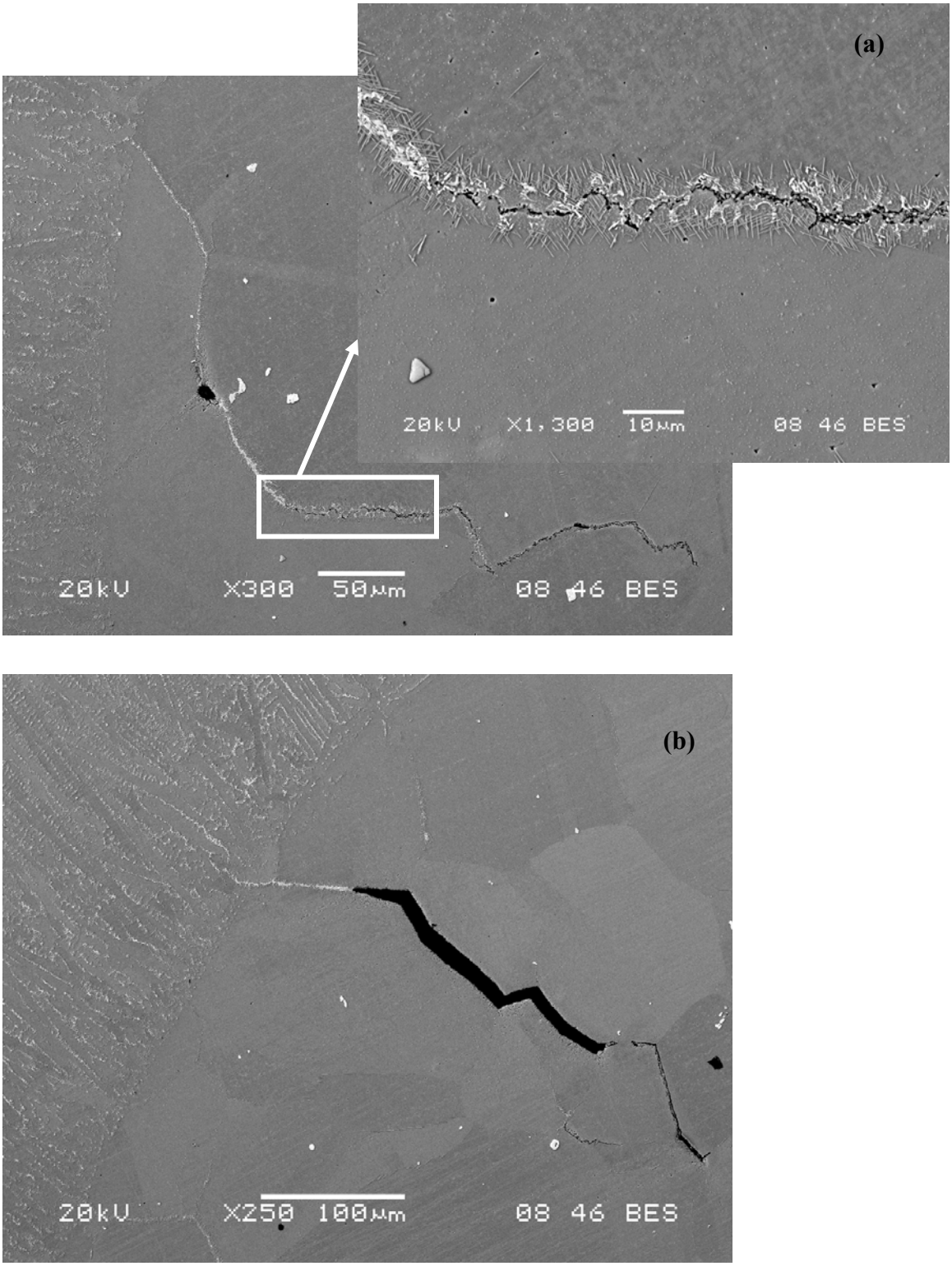

Fig. 4-43: SEM micrographs of a) fine and b) wide cracks in HAZ of 718Plus after post-weld heat treatment. Coupon was pre-weld solution heat treated at 1050°C/1hr +AC.

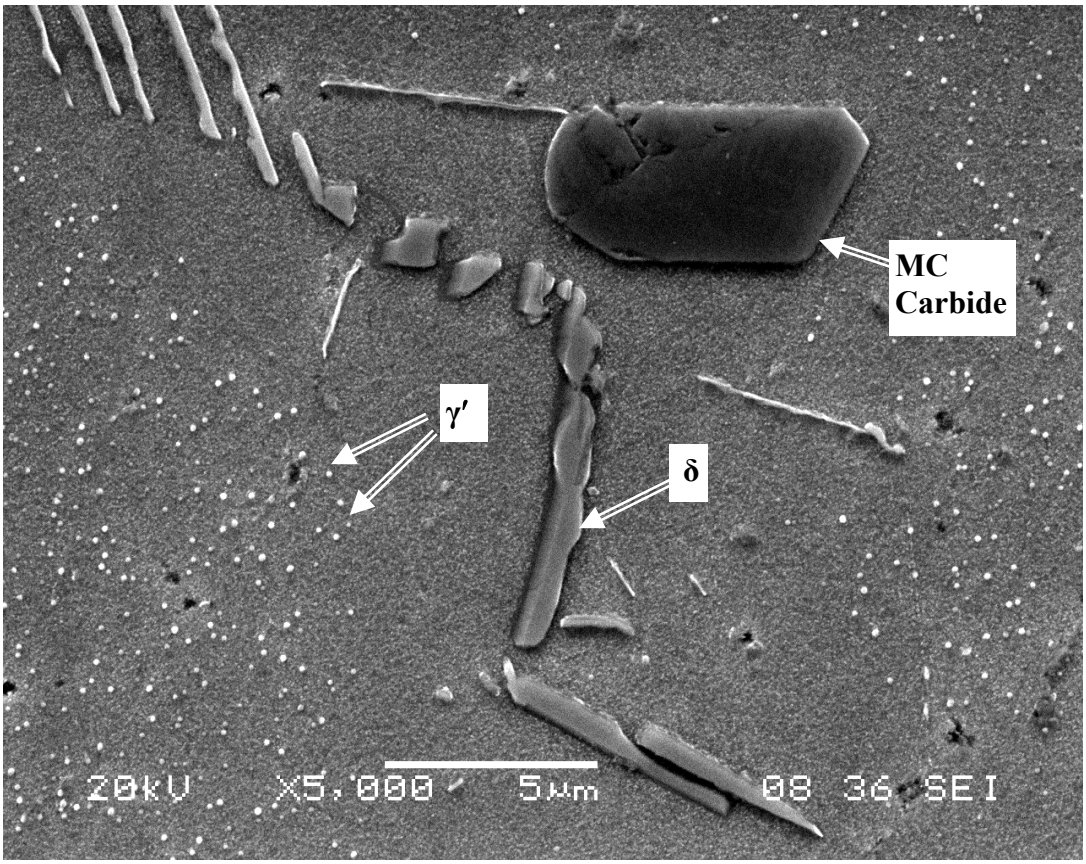

Fig. 4-44: SEM micrograph showing microstructure of HAZ grain interior of 718Plus after post-weld heat treatment.

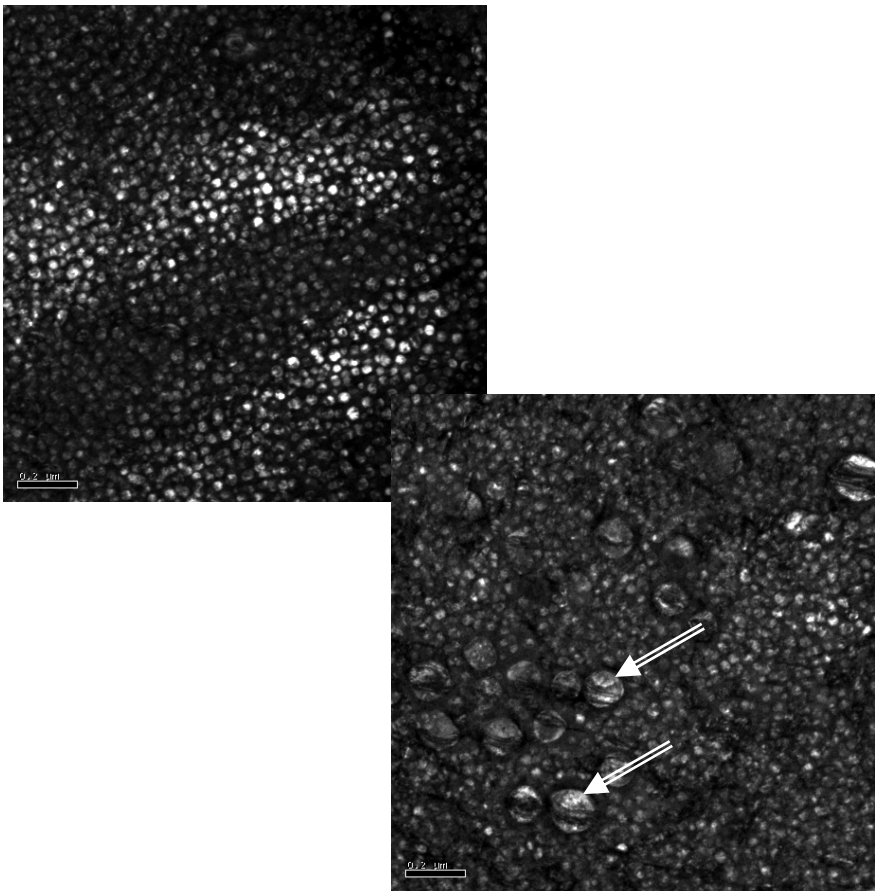

Fig. 4-45: TEM dark field image of γ′ particles in the HAZ of post-weld heat treated 718Plus. Arrows show occasionally large γ′ particles in finer γ′ particles.

The precipitation of γ′ during post-weld heat treatment of 718Plus, as observed in this work, is beneficial to the restoration of high temperature mechanical properties of the alloy. However, γ′ precipitation has been also reported as a major cause of cracking during post-weld heat treatments of γ′ strengthened nickel base superalloys.

4.3.4 Development of Post-Weld Heat Treatment Cracking in 718Plus

As earlier stated, post-weld heat treatments are carried out on welds to relieve them of welding residual stresses and develop a microstructure that will enhance their mechanical properties. However, despite the potential benefits of post-weld heat treatments, γ′ age-hardenable nickel base alloys are especially susceptible to cracking during the post-weld heat treatments. The cracks are usually intergranular in nature, and they range in size from microscopic to a few centimeters in length. Such cracks initiate in the HAZ, and may propagate into base metal regions that are unaffected by welding heat. Thus, their presence can lower the fracture toughness of the welds. In the present study, as-welded coupons of 718Plus (coupon A) which were initially crack-free after welding (Figs. 4-34 & 4-36) developed cracks during standard post-weld heat treatment, as shown in Figs. 4-40 – 4.42 and Table 4-5. Furthermore, coupons that originally cracked during welding (coupon B, shown in Figs. 4-42 & 4.44) showed further crack propagation (increase in average crack length – Table 4-5) and formation of new cracks (increase in total number of cracks - Table 4-5) during post-weld heat treatments. To determine effective ways of minimizing or preventing the occurrence of cracking of 718Plus during post-weld heat treatments, its cause(s) needs to be understood.

Several researchers [81 – 88] have investigated the causes of PWHT cracking in γ′ age hardenable superalloys, especially Rene 41 and Waspaloy. The various possible causes which were considered, and detailed in the review work of Thamburaj et al [94] included; Al + Ti composition of an alloy [89], grain size [90 – 92], pre-weld heat treatments [88, 92], post-weld heat treatment cycle [94 – 97], and heat treatment atmosphere [88]. In investigating these factors, the common theory proposed by the researchers was that post-weld heat treatment cracking occurred from a combination of residual welding and aging contraction stresses acting on the HAZ during post-weld heat treatment after it had been embrittled by metallurgical reactions that took place during welding.

During welding, the peak temperatures experienced by welds and HAZs alter their microstructure. Also, it results in high residual stresses being retained after the welds have cooled and solidified. To restore the properties of the welds, post-weld heat treatments comprising of high temperature solution anneal, needed to stress relief the welds, (in the present work – solution heat treatment at 950^{o}C/ 1hr + air cool), followed by aging (in the present work - aging at 788^{o}C/ 8 hrs + furnace cool to 654^{o}C/ 8 hrs + air cool) are carried out. However, on heating the alloy to the solution treatment temperature, it passes through γ′ precipitation temperature range. Thus, for an alloy with very fast γ′ precipitation kinetics, two processes will simultaneously compete; the residual welding stresses will begin to relax while the alloy also undergoes a rapid stiffening (loss in ductility) within its grain interior due to γ′ precipitation. The stiffening continues during subsequent aging heat treatments. The lattice parameter of γ′, e.g. in Rene 41 and

Waspalloy, is less than that of γ matrix [15], thus, the precipitation of a significant volume fraction of γ′ during aging, apart from stiffening the grain interior, could result in shrinkage contraction of the matrix. In weldments that are sufficiently restrained, or welds made on thicker sections, such contraction could lead to the development of high stresses that would further aggravate the stress condition of the alloy and would result in the initiation or propagation of cracks and relieve some of the stresses. Since the grain interior is hardened through precipitation of γ′, the relief cracks (termed post-weld heat treatment cracks) will preferentially initiate on HAZ grain boundaries that were embrittled/ weakened by prior liquation reactions that had occurred on them during welding. In summary, two things are necessary for post-weld heat treatment cracking to occur, namely; i) hardening of γ grain interior by γ′ precipitation, which also induce aging contraction stress in an alloy, ii) embrittlement of HAZ grain boundaries.

As discussed in the literature review (Chapter 2), Fig. 2-22 [89] shows the effects of Al and Ti, which are principal γ′ formers, on the cracking (both welding and post-weld heat treatment cracking) of Ni-base alloys. As shown on the figure, alloys above the dashed line have high Al + Ti concentration, and are difficult to weld because of their high susceptibility to cracking during welding and post-weld heat treatment. However, alloys below the dashed line have lower content of Al and Ti, and are considered to be readily weldable. Alloys like Rene 41 and Waspaloy are on the borderline and are weldable with some difficulty but they are susceptible to post-weld heat treatment cracking. The variation in cracking with Al + Ti content is attributed to the fact that these are major γ′ forming elements. Thus, the rate of precipitation, and volume fraction of γ′

will increase with an increase in Al + Ti content. Consequently, an alloy with high content of Al & Ti will age harden rapidly with an attendant rapid stiffening and aging contraction of its matrix, which will promote cracking on weakened HAZ grain boundaries. In alloys, e.g. 718, where strengthening is derived by the addition of niobium, as opposed to Al + Ti, γ″ precipitates as the main strengthening phase. The γ″ phase has a sluggish aging response, and as such, alloys that are predominantly strengthened by it are generally more resistant to post-weld heat treatment cracking but are less thermally stable at high temperature above about 650^{o}C. The new superalloy 718Plus has improved high temperature stability than alloy 718, and is predominantly strengthened by γ′ precipitation in contrast to 718, which is strengthened by precipitation of γ″. Examination of the HAZ of 718Plus after post-weld heat treatment revealed significant cracking occurred at grain boundary regions during the post-weld heat treatment, as shown in Figs. 4-40 – 4-43 and Table 4-5. Higher magnification SEM (Fig. 4-44) and TEM (Fig. 4-45) examinations of the grains surrounding the cracked HAZ grain boundaries revealed the presence of a significant volume fraction of γ′ precipitate. Also, it was notably observed that the cracking occurred mainly through a dense network of γ/Laves-type phase and extensive needle-like precipitates of δ; typical examples are shown in Figs. 4-41 & 4-43a. The Laves phase formed as a resolidification product on liquated HAZ grain boundaries during welding, while the extensive needle-like δ phase precipitated around the Laves phase during post-weld heat treatment. It has been reported in previous studies [23] on 718-type alloy that Laves phase is very brittle and has a weak interface with γ matrix, therefore, it provides preferential sites for easy crack initiation and propagation. Thus, during post-weld heat treatment of γ′ age-hardenable 718Plus, the

presence of the embrittling microconstituents on HAZ grain boundaries, coupled with aging contraction stresses from γ′ precipitation could result in cracking of the grain boundaries.

The susceptibility of 718Plus to post-weld heat treatment cracking may be significantly reduced by controlling the metallurgical reactions, e.g. grain boundary liquation, which embrittle the grain boundaries with Laves phase, and γ′ precipitation which hardens the matrix grain interior. In similar γ′ strengthened Ni-base superalloys, post-weld heat treatment cracking was minimized when the alloys were welded in soft/ ductile overaged condition rather than in fully aged or solutioned condition [88, 93, 143 – 145]. Thompson et al [88] reported a superior resistance to post-weld heat treatment cracking in Rene 41 that was slowly cooled from pre-weld solution annealing temperature. The heat treatment resulted in the formation of coarse overaged γ′ and softened the alloy prior to welding and post-weld heat treatment. In a similar concept, Lim et al [145] developed a cyclic overaging pre-weld heat treatment for Rene 80. The heat treatment resulted in the precipitation of coarse γ′ precipitates and was reported to improve the resistance of the alloy to post-weld heat treatment cracking. In a more recent work, Sidhu et al [93] studied the post-weld heat treatment cracking of autogenously GTAW welded Inconel 738 LC superalloy which was pre-weld heat treated in two different solution heat treatment conditions. The first heat treatment, designated as SHT, consisted of annealing at 1120^{o}C for 2 hrs in vacuum furnace, followed by argon quenching. The second heat treatment, designated as UMT, consisted of solution annealing at 1120^{o}C for 2hrs in vacuum furnace, followed by argon quenching and

subsequent aging at 845^{o}C for 24 hrs. Compared to SHT, UMT resulted in a formation of coarse, overaged γ′ and softened the alloy considerably. After post-weld heat treatment, the soft, overaged UMT samples had ~43% less cracking than the SHT [93]. This was attributed to the fact that the overaged base metal remained soft and ductile, and thus, has improved capability to absorb strain aging stress during post-weld heat treatment. As a result of this, stress relaxation could then be transferred to the soft, more ductile and voluminous base metal than on the embrittled HAZ grain boundaries which have little capacity to accommodate strain.

Chapter 5

Summary and Conclusions

The following summary and conclusions were made during this study:

5.1 Effect of Weld Heat Input on the Microstructure and Heat Affected Zone Cracking of 718Plus

1. The microstructure of 718Plus which was solution heat treated at 1025^{o}C/ 1hr + AC (air cool) prior to welding consisted of γ solid solution matrix, Nb & Ti – rich carboborides, and Ti & Nb – rich carbonitrides.
2. After welding, using low (about 137 J/mm) and high (about 472 J/mm) heat inputs, HAZ cracks were observed in the lower heat input welds, but their fusion zones were crack-free. However, both the HAZs and fusion zones of higher heat input welds were crack-free.
3. The HAZ cracks were observed to have irregular/ zigzag morphology that is typical of liquation cracks, and were often associated with constitutionally liquated grain boundary carbides. Also, the cracks were outlined by resolidification products which suggested that HAZ cracking in 718Plus is associated with the formation of liquid film on its grain boundaries during welding.
4. An extensive liquation of grain boundaries and grain interiors occurred in higher heat input welds, but their HAZs were crack-free. This was attributed to a combination of lower welding stresses generated from shallower HAZ thermal gradient, which resulted from the higher heat input, and an increased tendency of a

larger volume of intergranular liquid to reduce grain boundary cracking through crack-healing phenomenon or by better strain accommodation.

5. Although no HAZ cracking was observed in higher heat input welds, it resulted in a significant damage to parent microstructure through its extensive liquation. To produce high quality welds, such a high weld heat input is not recommended. Therefore, the applications of suitable pre-weld heat treatments which are capable of minimizing HAZ cracking of 718Plus were further investigated.
6. SEM examination of weld fusion zone of 718Plus showed that the microstructure consisted of γ dendrites and Nb-enriched Laves phase in the interdendritic regions. Large discrete carboboride and carbonitride phases were also observed within the fusion zone.
7. An important phenomenon of liquid backfilling was observed on HAZ grain boundaries of lower heat input welds. This resulted in healing of some of the HAZ cracks.

5.2 Influence of Pre-weld Heat Treatments on Weld Heat Affected Zone Cracking of 718Plus

1. Weld HAZ cracking in 718Plus was significantly influenced by pre-weld solution heat treatment temperature and cooling rate. No cracking was observed in samples that were pre-weld heat treated at $950^{o}C$ and cooled either by iced water quenching, air cooling or furnace cooling. However, HAZ cracking occurred in samples that were pre-weld heat treated at $1050^{o}C$ and $1150^{o}C$, respectively. The degree of cracking in the samples varied with cooling rates.

2. In samples that were pre-weld heat treated at 1050^{o}C and 1150^{o}C, respectively, the highest degree of cracking occurred in air cooled samples. This was followed by furnace cooled samples, while the lowest degree of cracking was found in samples that were quenched in iced-water after pre-weld heat treatment. At all the three cooling rates, the degree of cracking was always higher in samples pre-weld solution heat treated at 1150^{o}C than those that were solution treated at 1050^{o}C.
3. SIMS analyses revealed that grain boundary segregation of boron occurred during pre-weld solution heat treatments. The segregation occurred predominantly by non-equilibrium segregation mechanisms and varied with temperature and cooling rates. Segregation of boron was significantly minimized in samples which were heat treated at 950^{o}C and cooled by any of the three cooling rates employed (ID-WQ, AC, FC). However, brighter boron signal, suggesting higher segregation of boron, were observed in samples heat treated at 1050^{o}C and 1150^{o}C, respectively. The brightest boron intensity was observed in air cooled samples while iced-water quenching and furnace cooling significantly reduced segregated boron intensity.
4. Appreciable grain growth occurred with increase in pre-weld solution temperature. Grain size increased from ~ 58 μm to ~ 120 μm, and 360 μm when pre-weld solution treatment temperature increased from 950^{o}C to 1050^{o}C and 1150^{o}C, respectively. No significant variation in grain size occurred with cooling rates.
5. The occurrence of weld HAZ cracking in 718Plus was found to be associated with non-equilibrium grain boundary segregation of boron which depended on the pre-weld solution heat treatment temperature and cooling rates, and also the grain size

of the alloy prior to welding which was also dependent on the pre-weld treatment temperature.

6. It is concluded from this study that crack-free welds of 718Plus can be produced by carrying out a pre-weld solution heat treatment at 950^{o}C. At this temperature, both grain growth and non-equilibrium grain boundary segregation of boron were considerably minimized.

5.3 Post-Weld Heat Treatment Microstructure and Cracking in HAZ of 718Plus

1. As-welded 718Plus, which were pre-weld solution heat treated at 950^{o}C and 1050^{o}C, respectively, were post-weld heat treated using standard post-weld heat treatment cycles, which comprised of 950^{o}C/1hr +AC post-weld solution heat treatment, and aging at 788^{o}C/ 8 hrs + furnace cool to 654^{o}C/ 8 hrs + air cool. SEM & TEM microstructural examinations of the fusion zones of the post-weld heat treated coupons revealed that their microstructure comprised of MC-type carbides, and network of interdendritic Laves phase, which were also present in as-welded condition. Also observed were needle-like δ particles and spherical γ' phase, which precipitated during post-weld heat treatment. No γ'' precipitate was observed.
2. Examination of HAZs of the post-weld heat treated coupons, namely; coupon A (pre-weld solution heat treated at 950^{o}C/1hr +AC, then post-weld heat treated using standard heat treatment schedule of 950^{o}C/1hr +AC post-weld solution heat treatment, and aging at 788^{o}C/ 8 hrs + furnace cool to 654^{o}C/ 8 hrs + air cool), and coupon B (pre-weld solution heat treated at 1050^{o}C/1hr +AC, then post-weld heat

treated using standard heat treatment schedule of 950^{o}C/1hr +AC post-weld solution heat treatment, and aging at 788^{o}C/ 8 hrs + furnace cool to 654^{o}C/ 8 hrs + air cool), revealed the presence of cracks in the HAZ. Coupon A, which was originally crack-free before post-weld heat treatment, cracked during the post-weld heat treatment. Also, a significant increase in the extent of cracking occurred during post-weld heat treatment of coupon B, which contained original weld HAZ cracks.

3. Most of the new cracking that occurred during post-weld heat treatment propagated through dense network of Laves and δ phases on HAZ grain boundaries. The Laves phase formed as a resolidification product on liquated HAZ grain boundaries during welding, while the δ phase precipitated around the Laves phase during post-weld heat treatment.
4. A significant volume fraction of γ′ phase precipitated, both in the HAZ and base metal region, in the interior of grains which surrounded cracked grain boundaries.
5. Occurrence of post-weld heat treatment cracking in 718Plus was attributed mainly to a combination of embrittlement of HAZ grain boundaries by Laves and δ phases, and hardening of grains interior/ aging contraction stresses from γ′ precipitation.

Chapter 6

Suggestions for Future Work

1. Apart from HAZ grain boundary liquation cracking caused by constitutional liquation of MC-type carbides and grain boundary segregation of impurity elements (e.g. boron), it was reported in a recent study by Zhang and Ojo [146] that δ phase particles in HAZ of 718-type alloy can also constitutionally liquate. This is in contrast to the generally reported phenomenon that the particles undergo complete solid-state dissolution during thermal exposure in weld HAZ. It is expected that the penetration and wetting of HAZ grain boundaries by liquid from constitutionally liquated δ particles could contribute to HAZ liquation cracking in 718Plus, or otherwise, heal the cracks if present in large volume [147]. Therefore, a systematic and complete investigation needs to be carried out to study the potential contribution of constitutional liquation of δ particles to HAZ cracking during welding of 718Plus.
2. A considerable volume fraction of γ′ precipitates were observed in the present work after 718Plus coupons were pre-weld solution heat treated at 950^{o}C/ 1hr and 1050^{o}C/ 1hr, respectively, and furnace cooled. Following welding, the γ′ precipitates appeared to have liquated (Fig. 4-16b) The implication of this is that constitutional liquation of γ′ precipitates may occur during repair welding of service-damaged aerospace component made from 718Plus, which will be in fully aged condition prior to welding. Liquid from constitutional liquation of γ′ precipitates in a Ni-base superalloy was reported [148 - 149] to contribute to HAZ

liquation cracking in the alloy. Therefore, the occurrence of this phenomenon, i.e. constitutional liquation of γ′ precipitates and its potential effect on weld cracking in fully aged 718Plus needs to be properly considered and investigated.

3. Fusion welding processes, as employed in the present investigation, resulted in the formation of composite microstructure within a welded component of 718Plus. The microstructure of weld fusion zone differed from that of HAZ, which in-turn differed from that of the base region of the alloy. To homogenize the microstructure of the welded components and relieve them of welding residual stresses, standard post-weld heat treatments were carried out. This resulted in the precipitation of γ′ phase, which is beneficial to improving high temperature strength properties of the welds. However, embrittling phase, e.g. Laves, present in a significant volume fraction in the weld fusion zone and partly in the HAZ, was not eliminated/ dissolved by the post-weld heat treatment schedule. Further, the heat treatment resulted in an extensive precipitation of δ phase in the fusion and heat affected zones of the welds. The phases are known to impair the mechanical properties of welded components. It is thus imperative to study and recommend suitable post-weld heat treatments which will better homogenize the composite nature of the as-welded microstructure, and which will not contribute to further cracking.
4. One of the significant causes of post-weld heat treatment cracking in 718Plus was contraction stresses induced by γ′ precipitation. It is recommended that the evolution of these stresses should be studied by using advance X-ray techniques, and correlated with post-weld heat treatment cracking.

5. It is widely reported that the condition of an alloy prior to welding (controlled by pre-weld heat treatments) and post-weld heat treatments significantly affect its susceptibility to post-weld heat treatment cracking. Therefore, several combinations of pre-weld and post-weld heat treatments need to be studied to identify an optimum combination that will minimize the post-weld heat treatment cracking in 718Plus. More specifically, future study should investigate if post-weld heat treatment cracking in 718Plus could be eliminated by optimizing post-weld heat treatment schedule, in terms of heating rate, temperature, etc. Also, the use of filler materials should be investigated.

References

1. H.L. Eiselstein, Advances in the Technology of Stainless Steels and Related Alloys, ASTM, Philadelphia, PA, 1965, pp. 62-79 (ASTM STP 369).
2. W.D. Cao, R.L. Kennedy, Role of Chemistry in 718-type Alloys – Allvac 718Plus Alloy Development, in: K.A. Green, T.M. Pollock, H. Harada, T.E. Howson, R.C. Reed, J.J. Schirra, S. Walston (Eds.), Superalloys 2004, The Minerals, Metals and Materials Society, 2004, pp 91-99.
3. M. Prager and C.S. Shira, Welding of Precipitation-Hardening Nickel-Base Alloys, Welding Research Council Bulletin, No 128, 1968.
4. W.D. Cao, US Patent No.: 6,730.254 B2, 2004.
5. Allvac 718Plus Alloy, ATI Allvac Technical Data Sheet, 2005, pp 1-3.
6. H.L. Eiselstein, US Patent 3,046,108, 1962.
7. Allvac 718 Alloy, ATI Allvac Technical Data Sheet, 2008, pp 1-2.
8. J.M. Oblak, D.F. Paulonis and D.S. Duvall, Metall. Trans., Vol. 5, 1974, p 143.
9. M.C. Chaturvedi and Ya-fang Han, Metal Science, Vol. 17, 1983, p 145.
10. D.F. Paulonis, J.M. Oblak and D.S. Duvall, Trans. ASM, Vol. 62, 1969, p 611.
11. Madeleine Durand-Charre, The microstructure of superalloys, translated by Davidson, J.H., Gordon and Breach Science Publishers, 1997.
12. J.F. Radavich, J. of Metals, 1988, p 42.
13. R. Cozar and A. Pineau, Metall. Trans., Vol. 4, 1973, p 47.
14. H.J. Wagner and A.M. Hall, Physical Metallurgy of Alloy 718, DMIC Report 217, 1965.

15. M.J. Donachie and S.J. Donachie, Superalloys – A Technical Guide, 2nd ed., ASM International, 2002, pp 1-409.
16. Y.Y. Qiu, Scripta Materialia, Vol. 33, No 12, 1995, p 1961.
17. I. Kirman, J. Iron. Steel Inst., Vol. 207, 1969, p 1612.
18. J.P. Houvion, C. Frantz and M. Gantois, Mem. Sci. Rev. Metall., 1975, p 159.
19. M. Sundararaman, P. Mukhopadhyay and S. Banerjee, Metall. Trans., Vol. 19A, 1988, p 453.
20. S. Azadian, L. Wei and R. Warren, Materials Characterization, 53, 2004, p 7.
21. J.F. Muller and M.J. Donachie, Superalloys a technical guide, Materials Park, OH, ASM International, 1975, p 211.
22. M.K. Burke and M.K. Miller, Precipitation in Alloy 718: A combined AEM and APFIM investigation, Superalloys 718, 625, 706 and various derivatives (Ed. Loria, E.A.), 1991, p 337.
23. J.J. Schirra, R.H. Caless and R.W. Hatala, The effect of Laves phase on mechanical properties of wrought and cast + HIP 718, Superalloys 718, 625, 706 and various derivatives (Ed. Loria, E.A.), 1991, p 375 - 388.
24. R.L. Kennedy, Allvac 718Plus, Superalloy for the next forty years, Superalloys 718, 625, 706 and derivatives 2005 (Ed. Loria, E.A.), 2005, p 1.
25. W.D. Cao, Solidification and solid state phase transformation of Allvac 718Plus alloy, Superalloys 718, 625, 706 and derivatives 2005 (Ed. Loria, E.A.), 2005, p 165.
26. J.F. Radavich and T. Carneiro, A microstructural study of alloy 718Plus, Superalloys 718, 625, 706 and derivatives 2005 (Ed. Loria, E.A.), 2005, p 329.

27. X.S. Xie, G.M. Xu, G.L. Wang, J.X. Dong, W.D. Cao and R.L. Kennedy, Structure stability study on a newly developed nickel-base superalloy – Allvac 718Plus, Superalloys 718, 625, 706 and derivatives 2005 (Ed. Loria, E.A.), 2005, p 179.
28. M.B. Bever, Welding: An overview, Encyclopedia of Materials Science and Engineering, Pergamon Press, Oxford, 1986, p 5280.
29. Welding: An Overview, Encyclopedia of Materials Science and Engineering (Ed. Bever , M.B.), Vol. 7, 1986, p 5280.
30. S. Kou, Welding Metallurgy, 2nd ed., John Willey & Sons Inc., Hoboken, 2003, p 9.
31. Electron Beam Welding, ASM Handbook, Welding, Brazing and Soldering, ASM International, Vol. 6, 1993, pp 254-261.
32. K. Masubuchi, Residual stresses and distortion, ASM Handbook, Vol. 6, Welding, Brazing and Soldering, ASM International, 1993, pp 1094-1102.
33. K. Easterling, Introduction to the physical metallurgy of welding, Butterworth-Heinemann, 1992.
34. Overview of Weld Discontinuities, ASM Handbook, Welding, Brazing and Soldering, ASM International, Vol. 6, 1993, pp 1073-1080.
35. M.J. Cieslak, Cracking phenomenon associated with welding, ASM Handbook, Welding, Brazing and Soldering, ASM International, Vol. 6, 1993, pp 88 – 96.
36. A.R.E. Singer and P.H. Jennings, J. Inst. Metals, Vol. 73, 1947, p 197.
37. W.I. Pumphrey and J.V. Lyons, J. Inst. Metals, Vol. 74, 1948, p 439.
38. J.D. Dowd, Weld. J., Vol. 31, 1952, p 448s.
39. P.H. Jennings, A.R.E. Singer and W.I. Pumphrey, J. Inst. Metals, Vol. 74, 1948, p 227.

40. J.H. Dudas and F.R. Collins, Weld. J., Vol. 45, 1966, p 241s.
41. E.J. Michaud, H.W. Kerr and D.C. Weckman, in Trends in Welding Research, Eds. H.B. Smartt, J.A. Johnson, and S.A. David, ASM International, Materials Park OH, June 1995, p 154.
42. K. Nakata, and F. Matsuda, Trans. JWRI, Vol. 24, 1995, p 83.
43. M.J. Dvornak, R.H. Frost and D.L. Olson, Weld. J., Vol. 68, 1989, p 327.
44. M.C. Flemings, Solidification Processing, McGraw-Hill, New York, 1974.
45. J.C. Borland, Br. Weld. J, 1960, p 508.
46. J.C. Borland, Welding and Metal Fabrication, Vol. 47, 1979, p 19.
47. J. Vero, Metal Industry, Vol. 48, 1936, pp 431- 494.
48. A.R.E. Singer and S.A. Cotterell, J. Inst. Metals, Vol. 73, 1946, p 33.
49. W.I. Pumphrey and P.H. Jennings, J. Inst. Metals, Vol. 75, 1948, p 235.
50. B.I. Medovar, Automatic Welding, Vol. 7, 1954, p 12.
51. W.S. Pellini, Foundry, Vol. 80, 1952, pp 125 – 133, 192 – 199.
52. H.F. Bishop, C.G. Ackerlind and W.S. Pellini, Trans. Amer. Foundry Soc., Vol. 60, 1952, p.
53. P.P. Pusak, W.R. Apblett and W.S. Pellini, Welding J., Vol. 35, 1956, pp 9s.
54. M.C. Chaturvedi, Materials Science Forum, Vol. 546-549, 2007, p 1163.
55. W.A. Owczarski, D.S. Duvall and C.P. Sullivan, Weld. J., Vol. 46, 1967, p 423s.
56. J.J Pepe and W.F. Savage, Weld. J., Vol. 46, 1967, p 411s.
57. B. Weiss, G.E. Grotke and R. Stickler, Weld. J., Vol. 49, 197, p 471s.
58. J.A. Brooks, Weld. J., Vol. 53, 1974, pp 517.

59. R.G. Thompson, B. Radhakrishnan and P.E. Mayo, Journal of Physics , Vol. 49, 1988, pp C5-471 – C5-478.
60. W.A. Baeslak III and D.E. Nelson, Metallography, Vol. 19, 1986, p 371.
61. B. Radhakrishnan and R.G. Thompson, Metall. Trans. A, Vol. 24A, 1993, p 1409.
62. R. Nakkalil, N.L. Richards and M.C. Chaturvedi, Metall. Trans. A, Vol. 24A, 1993, p 1169.
63. X. Huang, M.C. Chaturvedi and N.L. Richards, Metall. Trans. A, Vol. 27A, 1996, p 785.
64. X. Huang, M.C. Chaturvedi, N.L. Richards and J. Jackman, Acta Mater., Vol. 45, 1997, p 3095.
65. W. Chen, M.C. Chaturvedi and N.L. Richards, Metall. Trans. A, Vol. 32A, 2001, p 931.
66. O.A. Ojo, N.L. Richards and M.C. Chaturvedi, Mater. Sci. Tech., Vol. 20, 2004, p 1027.
67. O.A. Ojo, N.L. Richards and M.C. Chaturvedi, Metall. Trans. A, Vol. 37A, 2006, p 421.
68. K.R. Vishwakarma, M.C. Chaturvedi, in: E.A. Loria (Ed.), Superalloys 718, 625, 706 and Derivatives 2005, The Minerals, Metals and Materials Society, 2005, pp. 637-647.
69. O.A. Ojo, PhD Thesis, The University of Manitoba, 2004, p 89.
70. A.N. Aronson, MSc Thesis, Rensselaer Polytechnique Inst., Troy, New York, 1963.
71. D. McLean, Grain boundaries in metals, Clarendon Press, oxford, 1957.

72. E.D. Hondros and M.P. Seah, in Physical Metallurgy (Ed. R.W. Cahn), 3rd edn, North Holland, Amsterdam, 1984.
73. M. Mclean and A. Strang, Metals Technol., Vol. 11, 1984, p 454.
74. J.H. Westbrook and K.T. Aust, Acta Metall., Vol. 11, 1963, p 1151.
75. K.T. Aust, R.E. Hanneman, P. Nissen and J.H. Westbrook, Acta Metall., Vol. 16, 1968, p 291.
76. R.L. Eadie and K.T. Aust, Scripta Metall., Vol. 4, 1970, p 641.
77. K.T. Aust, Canadian Metallurgical Q., Vol. 13, No. 1, 1974, p 133.
78. R.G. Faulkner, R.B. Jones, Z. Lu and P.E.J. Flewitt, Phil. Mag., Vol. 85, No. 19, 2005, p 2065.
79. K.T. Aust, S.J. Armijo, E.F. Kock and J.H. Westbrook, Trans. Am. Soc. Metals, Vol. 6o, 1967, p 360.
80. T.R. Anthony, Acta Metall., Vol. 17, 1969, p 603.
81. W.P. Hughes and T.F. Berry, Weld. J., Vol. 46, 1967, p 361s.
82. L.C. Lim, J.Z. Yi, N. Liu and Q. Ma, Mater. Sci. Tech., Vol. 18, 2002, p 407.
83. K.C. Wu and R.E. Herfert, Weld. J., Vol. 1, 1967, p 32s.
84. A.W. Dix and W.F. Savage, Weld. J., Vol. 50, No. 6, 1971, p 247s.
85. J.E. Franklin and W.F. Savage, Weld. J., Vol. 53, No. 9, 1974, p 380s.
86. D.S. Duvall and W.A. Owczarski, Weld. J., Vol. 48, No. 1, 1969, p 10s.
87. Y. Nakao, Trans. Weld. Soc., Vol. 19, No. 1, 1988, p 66.
88. E.G. Thompson, S. Nunez and M. Prager, Weld. J., Vol. 47, No. 7, 1968, p 299s.
89. W. Yeniscavich, in The Superalloys, (Ed. C.T. Sims, N.S. Stoloff and W.C. Hagel), John Wiley and Sons, New York, 1972, p 509.

90. M. Prager and G. Sines, Weld. Res. Council Bull., No. 150, 1970, p 24.

91. J.B. Carlton and M. Prager, Weld. Res. Council Bull., No. 150, 1970, p 13.

92. T.F. Berry and W.P. Hughes, Weld. J., Vol. 48, No. 11, 1969, p 505s.

93. R.K. Sidhu, N.L. Richards and M.C. Chaturvedi, Mater. Sci. and Tech., Vol. 23, No. 2, 2007, p 203.

94. R. Thamburaj, W. Wallace and J.A. Goldak, International Metals Reviews, Vol. 28, No. 1, 1983, p 1.

95. W.A. Owczarski and C.P. Sullivan, Weld. J., Vol. 44, No. 6, 1965, p 241s.

96. D.E. Jordan and E.G. Richards, in Heat Treatment Aspects of Metal Joining Processes, The iron and Steel Institute, London, 1972, p 71.

97. F.M. Burdekin, in Heat Treatment Aspects of Metal Joining Processes, The iron and Steel Institute, London, 1972, p 6.

98. D.S. Duvall and W.A. Owczarski, , Weld. J., Vol. , 1967, p 423s.

99. R.G. Thompson and S. Genculu, Weld. J., Vol. , 1983, p 337s.

100. B. Radhakrishnan and R.G. Thompson, Metall. Trans. A, Vol. 22A, 1991, p 887.

101. B. Radhakrishnan and R.G. Thompson, Metall. Trans. A, Vol. 23A, 1992, p 1783.

102. R.G. Thompson, B. Radhakrishnan and P.E. Mayo, Journal of Physics, Vol. 49, 1988, p 471.

103. T.J. Kelly, Weld. J, Vol. 68, 1989, p 44s.

104. W. Chen, M.C. Chaturvedi, N.L. Richards and G. McMahon, Metall. Trans. A, Vol. 29A, 1998, p 1947.

105. H. Guo, M.C. Chaturvedi and N.L. Richards, Sci. and Tech. of Welding and Joining, Vol. 3, No. 5, 1998, p 257.

106. H. Guo, M.C. Chaturvedi, N.L. Richards and G.S. McMahoon, Scripta Materialia, Vol. 40, No 3, 1999, p 383.

107. M. Qian and J.C. Lippold, Weld. J., Vol. 82, No. 6, 2003, p 145s.

108. K.R. Vishwakarma, PhD Thesis, The University of Manitoba, 2008, pp 1-267.

109. K. Poorhaydari, B.M. Patchett and D.G. Ivey, Weld. J., 2005, p 149s.

110. N.L. Richards, R. Nakkalil and M.C. Chaturvedi, Metall. Trans. A., Vol. 25A, 1994, p 1733.

111. A. Koren, M. Roman, I. Weisshaus and A. Kaufman, Weld. J., Vol. 61, No. 11, 1982, p 348.

112. K. Shinozaki, H. Kuroki, X. Luo, H. Ariyoshi and M. Shirai, Welding International, Vol. 13, No. 12, 1999, p 945.

113. W.A. Miller and G.A. Chadwick, Acta Metallurgica, Vol. 15, 1967, p 607.

114. C.E. Cross, W.T. Tack and L.W. Loechel, Proceedings, Materials Weldability Symposium, Detroit, MI; Oct. 1990, Published by ASM International, Metal Park.

115. D.G. Eskin, Suyitno and L. Katgerman, Progress in Materials Science, Vol. 49, 2004, p 629.

116. T. W. Clyne and G. J. Davies, British Foundryman, Vol. 74, No. 4, 1981, p 65

117. B. Rhadhakrishnan and R.G. Thompson, Metall. Trans. A., Vol. 24A, 1993, p 2773.

118. W.A. Owczarski, D.S. Duvall and C.P. Sullivan, Weld. J., Vol. 45, No. 4, 1966, p 145s.

119. O.A. Ojo and M.C. Chaturvedi, Metall. Trans. A., Vol. 38, 2007, p 356.

120. R. Nakkalil, N.L. Richards and M.C. Chaturvedi, Acta Metall. Mater., Vol. 41, No. 12, 1993, p 3381.

121. S.W. Baker and G.R. Purdy, Acta Mater., Vol. 46, No. 2, 1998, p 511.

122. V.L. Acoff and R.G. Thompson, Metall. Trans. A., Vol. 27A, 1996, p 2692.

123. B. Radhakrishnan and R.G. Thompson, Scripta Metallurgical et Materialia, Vol. 24, 1990, p 537.

124. R. Nakkalil, N.L. Richards and M.C. Chaturvedi, Scripta Metallurgical et Materialia, Vol. 26, 1992, p 1599.

125. W.F. Savage and D.W. Dickinson, Weld. J., Vol. 51, No. 11, 1972, p 555s.

126. C.D. Lundin, C.H. Lee and C.Y.P. Qiao, Weld. J., Vol. 72, No. 7, 1993, p 321s.

127. J.C. Lippold, Weld Cracking Mechanisms in Austenitic stainless Steels, in: Trends in Welding Research in the United State, American Society for Metals, 1982, p 209.

128. N.L. Adams, Physics and Chemistry of Surfaces, Oxford University Press, London, 1942.

129. G.A. Knorovsky, M.J. Cieslak, T.J. Headley, A.D. Romig Jr. and W.F. Hammetter, Metall. Trans. A., Vol. 20A, 1989, p 2149.

130. O.A. Ojo, N.L. Richards, M.C. Chaturvedi, Scripta Materialia, Vol. 50, 2004, p 641.

131. O.A. Ojo, R.G. Ding, M.C. Chaturvedi, Scripta Materialia, Vol. 54, 2006, p 2131.

132. J.H. Westbrook, Metall. Rev. Vol. 9, 1964, p 415.

133. R.G. Faulkner, Int. Mater. Rev., Vol. 41, 1996, p 198.

134. X. Tingdong and C. Buyuan, Prog. Mater. Sci., Vol. 49, 2004, p 109.

135. X.L. He, Y.Y. Chu and J.J. Jonas, Acta. Metall. Vol. 37, No. 11, 1989, p 2905.

136. T.M. Williams, A.M. Stoneham and D.R. Harries, Metal Science Vol. 19, 1976, p 14.

137. I. Karlsson, H. Norden and H. Odelius, Acta Metall. Vol. 36, No 1, 1988, p 1.

138. M.A. Morimer, Grain Boundary in Engineering Materials, 4th Bolton Landing Conf., ed. J.L. Walter, J.H. Westbrook and D.A. Woodford. Claitors Publication Division, Baton Rouge, LA, 1974, p 647.
139. R.G. Thompson, J.J. Cassimus, D.E. Mayo and J.R. Dobbs, Weld. J., 1985, p 91s.
140. R.G. Faulkner, J. Mater. Sci., Vol. 16, 1981, p 373.
141. B.R. Patterson and Y. Liu, Metall. Trans. A, Vol. 23A, 1992, p 2481.
142. R.G. Thompson, Welding Metallurgy of Non-ferrous High Temperature Materials, ASM Handbook, Vol. 6, 1993, p 567.
143. D.S. Duvall and W.A. Owczarski, Weld. J., Vol. 50, 1971, p 401s.
144. A.T. D′Annessa, Technical report no: AFML-TR-72-17, Air force materials laboratory, Wright-Petterson, OH, USA, 1972.
145. L.C. Lim, J.Z. Yi, N. Liu and Q. Ma, Mater. Sci. Tech., Vol. 18, 2002, p 413.
146. O.A. Ojo, H.R. Zhang, Phil. Mag. Letters, Vol. 89, No. 12, 2009, p 787.
147. O.A. Ojo, M.C. Chaturvedi, Metall. Trans. A, Vol. 38, No. 2, 2007, p 356.
148. O.A. Ojo, N.L. Richards, M.C. Chaturvedi, Scripta Materialia, Vol. 51, 2004, p 141.
149. O.A. Ojo, N.L. Richards, M.C. Chaturvedi, Mater. Sci. Eng. A, Vol. 403, 2005, p 77.

Refereed Publications from the Present Thesis

1. O.A. Idowu, O.A. Ojo, M.C. Chaturvedi, Crack-Free Electron Beam Welding of Allvac 718Plus Superalloy, Weld. J., Vol. 88, 2009, pp 179s – 187s.
2. O.A. Idowu, O.A. Ojo, M.C. Chaturvedi, Microstructural Response of Allvac 718Plus to Variation in Heat Input During Laser Beam Welding, In: Aerospace Materials and Manufacturing IV: Advances in Processing and Repair of Aerospace Materials, The 47th Annual Conference of Metallurgist, Winnipeg, August 24 – 27, 2008, Paper No. 3119.
3. O.A. Idowu, O.A. Ojo, M.C. Chaturvedi, Effect of Heat Input on Heat Affected Zone Cracking in Laser Welded ATI Allvac 718Plus Alloy, Material Science and Engineering A., Vol. 454-445, 2007, pp 389 – 397.

Other Refereed Publications

1. O.A. Idowu, O.A. Ojo, M.C. Chaturvedi, Microstructural Study of Transient Liquid Phase Bonded Cast Inconel 738 Superalloy, Metallurgical and Materials Transactions A, Vol. 37 A, No. 9, 2006, pp 2787 – 2796.
2. O.A. Idowu, N.P. Wikstrom, O.A. Ojo, M.C. Chaturvedi, Transient Liquid Phase Bonding of a Nickel Base Superalloy: Effects of Process Variables, Proceedings of 3rd International Symposium on Aerospace Materials and Manufacturing: Emerging Materials, Processes, and Repair Techniques, Montreal, Canada, 2006, pp 289 – 299.

3. N. P. Wikstrom, O.A. Idowu, O.A. Ojo, M.C. Chaturvedi, Deviation from Conventional Transient Liquid Phase Bonding Models during Diffusion Brazing of Ni-base Superalloys, Proceedings of 3rd Intl. Brazing and Soldering Conference, San Antonio, Texas, USA, 2006, pp 6-11.
4. O.A. Idowu, N.L. Richards, M.C. Chaturvedi, Effect of Bonding Temperature on Isothermal Solidification Rate during Transient Liquid Phase Bonding of Inconel 738LC Superalloy, Materials Science and Engineering A, Vol. 397, No. 1-2, 2005, pp 98 – 112.

Poster Presentations

1. O.A. Idowu, Formation of Carboboride Particles in the Diffused Layer of a TLP Bonded IN 738 Ni-base Alloy, 17th Canadian Materials Science Conference, University of British Columbia, Vancouver, Canada, June 2005 (**Best Poster Presentation Award**).
2. O.A. Idowu, Formation of Boride Particles in The Diffused Layer of a Transient Liquid Phase Bonded IN 738 Nickel-Based Superalloy, The 47th Annual Conference of Metallurgist, Winnipeg, August 24 – 27, 2008 (**2nd price Graduate Student Poster Award**).